Single-particle states in neutron-rich 69Cu and 71Cu by means of the (d,3He) transfer reaction

Pierre Morfouace

Institut de Physique Nucléaire

CNRS - UNIVERSITÉ PARIS SUD

26 Septembre 2014 IPNO-T-14-01

Thèse

Présentée par

MORFOUACE Pierre

Pour obtenir le grade de Docteur ès Sciences
De l'Université Paris Sud

Single-particle states in neutron-rich ^{69,71}Cu by means of the (d,^{3}He) transfer reaction

École Doctorale Particules, Noyaux, Cosmos
Université Paris-Sud XI
Institut de Physique Nucléaire d'Orsay

THÈSE

pour l'obtention du Diplôme de
Docteur en Sciences de l'Université Paris-Sud XI
Spécialité Physique Nucléaire

par

Pierre MORFOUACE

Le 26 septembre 2014

Single-particle states in neutron-rich ^{69,71}Cu by means of the (d,^{3}He) transfer reaction

Composition du jury :

Président du jury	Prof. Elias KHAN	Paris-Sud XI - IPN, Orsay
Directeur de thèse	Dr. Faiçal AZAIEZ	IPN, Orsay
Co-Directeur de thèse	Dr. Serge FRANCHOO	IPN, Orsay
Rapporteur	Dr. Navin ALAHARI	GANIL, Caen
Rapporteur	Dr. Daniel BAZIN	NSCL, Michigan State University, USA
Examinateur	Dr. Riccardo RAABE	KU Leuven, Belgique
Examinateur	Dr. Olivier SORLIN	GANIL, Caen

Remerciements

Après ces trois années de thèse qui viennent conclure les huit années du cycle universitaire, le temps des remerciements est arrivé. Ces quelques lignes en français, les seules de ce manuscrit, s'adressent à tous ceux qui m'ont accompagné, avec qui j'ai partagé des moments de travail, de shift de nuit mais aussi de détente et de plaisir.

Tout d'abord, je remercie Elias Khan, Navin Alahari, Daniel Bazin, Olivier Sorlin et Riccardo Raabe d'avoir accepté d'être les membres de mon jury de thèse, et en particulier Navin Alahari et Daniel Bazin d'avoir été les rapporteurs de ce travail.

Je remercie Faiçal Azaiez de m'avoir accueilli au sein de l'Institut de Physique Nucléaire dans le groupe NESTER (Noyaux Exotiques STructure Et Réaction) ainsi que d'avoir été mon directeur de thèse officiel pendant ces trois années. Je remercie sincèrement Serge Franchoo qui m'a encadré pendant cette thèse : merci pour ta disponibilité, ta rigueur et tes conseils. Nos discussions m'ont beaucoup appris et apporté.

Je veux également remercier tous les membres du groupe NESTER avec qui j'ai pu également échanger et qui m'ont beaucoup aidé. La bonne ambiance du groupe a contribué à ma motivation de tous les jours. Je remercie en particulier Marlène, Fairouz, Nicolas, Iulian, Iolanda pour leur aide bien sûr, mais aussi pour discuter/partager leurs goûts en matière de séries, films, livres, voyages... bref, de tout autre chose que de la physique. Je remercie également David pour nos échanges et avec qui c'est toujours agréable de discuter, Fadi, Daisuke, Pierre et Jacques pour leurs discussions sur les modèles de réactions notamment, Andrea pour les discussions du midi et sa bonne humeur ainsi que Yorick pour son aide et ses conseils.

Les expériences auxquelles j'ai participé pendant ma thèse ont été très formatrices et je tiens à remercier toute l'équipe d'ALTO et en particulier Hakim pour l'expérience au split-pole et je n'oublie pas non plus toute l'équipe du GANIL pour leur aide précieuse et le bon déroulement de l'expérience avec Must2.

Un grand merci à Laurence et Céline pour leur disponibilité, leur bonne humeur et leur aide précieuse. Je remercie également Pascale qui rythme la pause café du midi.

Je veux remercier Julien Gibelin pour son aide informatique et sa fameuse charte des noyaux. Et je n'oublie pas Kamila, experte du modèle en couche avec qui j'ai eu la chance de travailler. Je la remercie pour son aide, sa disponibilité, la relecture de mon manuscrit et nos différentes discussions ainsi que pour m'avoir fait découvrir un très bon japonais strasbourgeois.

Merci à la génération de thésard qui m'a précédé : merci à toi Adrien de m'avoir beaucoup aidé pour mes premiers pas de jeune thésard/padawan, ton aide m'a été très précieuse, merci également à Sandra qui finissait quand je commençais et également à l'ensemble des thésards "MUST2" : Laurent, Simon et Freddy. Pendant les deux premières années j'ai partagé le bureau avec Laurent et Marine : merci à vous deux pour ces deux superbes années qui sont passées très vite. Je n'oublie pas Aurélie et Marie-Co qui ont partagé avec moi ce bureau lors de ma dernière année avec beaucoup de bonne humeur ainsi que les pauses café accompagnées de Benjamin que je remercie pour son éternelle joie de vivre, et Noël pour partager le goût des films MARVEL avec moi ;) Je vous souhaite une bonne continuation pour la fin de votre thèse et pour la suite. Bon courage également aux nouveaux thésards du groupe : Louis et Claire. Finalement, un remerciement clin d'oeil au RER B qui m'a appris la patience et qui malgré ses aléas hebdomadaires m'a finalement amené au bureau pendant ces trois années.

Merci à Gaël pour ces années au Magistère et notre goût commun pour Brassens, je n'oublie pas non plus Caroline et Sandrine... J'en profite aussi pour remercier une nouvelle fois Elias de m'avoir fait découvrir la physique nucléaire et la physique des particules dans son cours de M1 et qui m'a donné envie de continuer.

Je veux aussi ici remercier tous ceux avec qui j'ai partagé une bière ou deux... et pour tous les moments mémorables qu'on a pu passer ensemble : merci Matthieu évidemment, Julian, Benjamin, Romain, Flavien, Julien, Aurélien, Guillaume, Tico, Alice, Asénath, Marie, Agnès *e* Marta... Merci également à tous les "lamballais" pour les bons moments ressourçant en Bretagne ! Et bon courage Pierre pour l'année prochaine !

Enfin je voudrais terminer par remercier ma famille, mes parents tout d'abord, qui m'ont toujours soutenu et accompagné pendant mes études et qui ont toujours été présent, je n'oublie pas de remercier ma soeur Marie, qui m'a aussi servie d'exemple et qui m'a montré le chemin... Ces derniers mots sont pour Pauline, merci d'avoir partagé ma vie pendant ces trois années de thèse et de m'avoir soutenu.

C'est les personnes que l'on côtoie qui nous façonnent, je voudrais donc finir par remercier toutes les personnes qui m'ont servi d'exemple à un moment ou à un autre[1].

J'espère que votre lecture ne s'arrête pas là ;) je vous souhaite donc une bonne lecture à tous !

Paris, October 7, 2014.

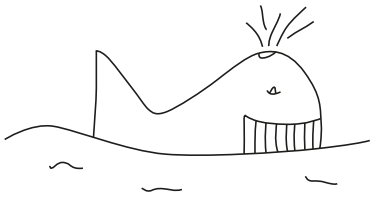

L'avenir est là ; il nous appelle, ou plutôt il nous tire à lui : cette traction ininterrompue, qui nous fait avancer sur la route du temps est cause aussi que nous agissons continuellement.

Henri Bergson (1859 - 1941)
L'énergie spirituelle (1919)

[1]Cette liste n'est évidemment pas exhaustive, et je m'excuse d'avoir pu oublier certains noms dans ces quelques lignes

Contents

Pour un esprit scientifique, toute connaissance est une réponse à une question.

Gaston Bachelard (1884-1962)

Introduction

With the discoveries of the proton in 1911 by Rutherford [1] and the neutron in 1932 by Chadwick [2], the physicists could understand better and better the constituents of matter. These two particles are the two building blocks of the atomic nucleus which corresponds to essentially all the visible mass in the universe.
Protons and neutrons (the nucleons) are the bound states at lowest energy of baryons composed of quarks and gluons. Through the strong interaction, the nucleons can interact and sometimes they can form together bound states of nuclei. In nuclear physics we consider the nucleon as structureless elementary particle. This is justified because in the low-energy region the nucleons hardly get excited. Then we can understand the properties of the nuclear many-body system thanks to the nucleon-nucleon interaction. To understand the low-energy properties, a lot of nuclei are at our disposal to study. Indeed we count 288 stable nuclei on earth in the valley of stability [3] but thousands of them (≈6000) that are unstable exist in the universe situated between the *drip-lines*, which define the limit of existence. This instability is due to an excess of protons or neutrons. We can today produce a lot of radioactive nuclei in our laboratories. In figure 1 the nuclear chart is presented, which is the playground of the nuclear physicist. We are very interested to access nuclei with an abnormal ratio of neutrons over protons N/Z to understand the evolution of the nuclear interaction. We call these nuclei *exotic nuclei*. These exotic nuclei can show unexpected behavior by comparison to the stable ones: for instance the evolution of shells with the appearance of new *magic numbers* as it was experimentally shown recently in the neutron-rich calcium isotopes [4] with the new magic numbers $N = 32$, these phenomena of shell evolutions are also well studied theoretically where theoreticians point out the appearance of new magic numbers [5]; the halo nuclei are also a well known example of unexpected behavior with their neutron skins and their huge spatial distribution [6]. This is why there is nowadays a huge effort both experimentally and theoretically to understand these behaviors and to constrain the

evolution of the nuclear structure.
Different experimental techniques are at our disposal to study the accessible nuclei and pin down the nuclear forces at stakes: among them the β-decay study to measure the level scheme and branching ratio as the β-decay time of flight for instance, or in general manner the collision between nuclei that can lead to different processes such as the elastic scattering, the inelastic reaction, the transfer reaction where one or few nucleons are exchanged between the beam and the target or the fusion to form a compound nucleus. Direct reaction such as the pick-up reaction are an important tool in nuclear physics because this kind of reaction probes the single-particle character of the states in a nucleus. That's why, when it is possible, direct reactions are a very interesting tool to probe the shell evolution at the extreme of isospin.
In this thesis, we are particularly interested in the proton-shell evolution in neutron-rich Copper isotopes between $N = 40$ to $N = 50$ toward the doubly-magic ^{78}Ni nucleus. In this manuscript, we shall focus on the proton-hole states along the isotopic chain of Copper, in particular in ^{69}Cu and ^{71}Cu. Indeed, proton-hole states in Copper isotopes are very interesting to probe the $Z = 28$ gap and that will be studied through the (d,^{3}He) proton pick-up reaction. In a first part we explain the motivations and the experimental procedure to study these two nuclei, during the second part we describe the experimental setup and the data analysis for ^{69}Cu while the third part is devoted to the ^{71}Cu nucleus and finally in the last part we present the interpretation of the results.

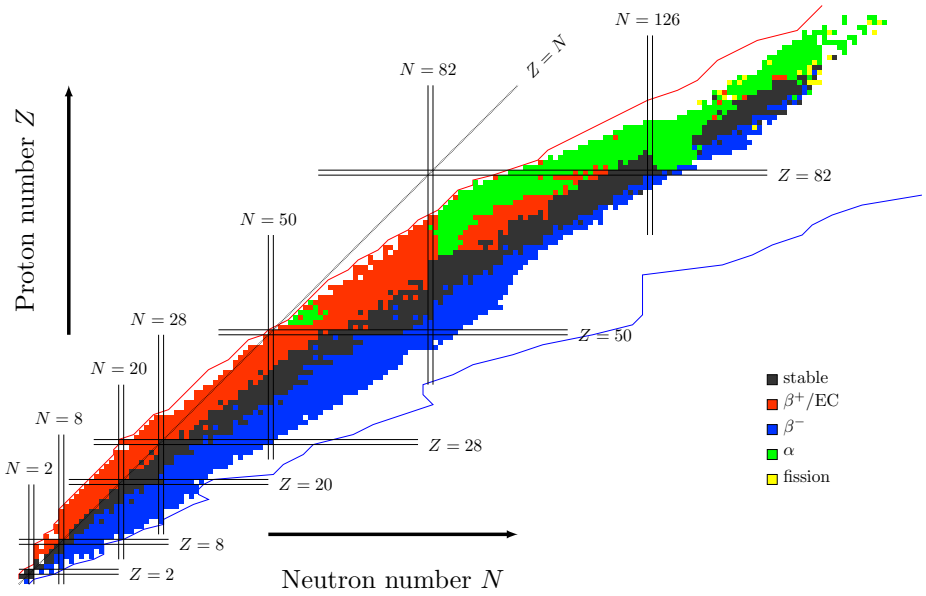

Figure 1: *Nuclear chart classified as a function of the proton and neutron numbers. The valley of stability is represented in black and the different colors represent the different decay modes*

Part I

Motivation and experimental method

1

Nuclear models

Contents

In the following we stress the basic properties of nuclei and we explain in the framework of the shell model the theory of the many-body problem.

1.1 Bulk properties and nuclear forces

1.1.1 The liquid-drop model

Before the discovery of the neutron, the first nuclear model was proposed by G. Gamow in 1930 [7], the so-called liquid-drop model. In this model, the nucleus is described as an incompressible charged liquid-drop with a volume proportional to the number of particles A. In this context, the binding energy of the nucleus is:

$$B(A,Z) = a_V A - a_S A^{2/3} - a_C \frac{Z^2}{A^{1/3}} - a_{sym} \frac{(N-Z)^2}{A} \pm \frac{\delta}{A^{1/2}}, \tag{1.1}$$

with the typical values $a_V = 16$ MeV for volume, $a_S = 17$ MeV for surface, $a_C = 0.7$ MeV for Coulonb, $a_{sym} = 23$ MeV for the asymmetry term and $\delta = 12$ MeV the pairing constant. The plus sign is for even-even nuclei, the minus sign for odd-odd nuclei and for odd-even nuclei we have $\delta = 0$. The typical binding-energy is about 8 MeV per nucleon. Then the empirical relation for masses is:

$$M(A,Z) = (A-Z)m_n + Zm_P - B(A,Z) \tag{1.2}$$

This equation is known as the Bethe-Weizsäcker semi-empirical mass formula. For a given number of nucleons A in a nucleus, its radius follows the empirical law:

$$R(A) = r_0 A^{1/3}, \tag{1.3}$$

where $r_0 \approx 1.2$ fm. Thus the nuclear volume is proportional to the number of nucleons in the nucleus.
The least bound nucleon has a binding energy about 8 MeV and a kinetic energy about 40 MeV while the nucleon mass is $mc^2 \approx 938$ MeV. One can see then that the kinetic energy is negligible compared to the mass, leading to the assumption of non-relativistic theory to be able to describe the nucleus. Most recently, the development of relativistic theories have become important despite of the simple view we are giving. Indeed, we can estimate that the velocity of this least bound nucleon with a kinetic energy of $T = 40$ MeV:

$$v = \sqrt{\frac{2T}{m}} = c\sqrt{\frac{2T}{mc^2}} \approx 0.3c, \tag{1.4}$$

this velocity that corresponds to one third of the speed of light is associated with the de Broglie wavelength:

$$\lambda = \frac{2\pi\hbar}{mv} = \frac{2\pi\hbar c}{\beta mc^2} \approx 4.5 \text{ fm}. \tag{1.5}$$

We can see that λ is not small compared to nuclear radius whose range is from 1.2 fm up to 8 fm, leading to the fact that quantum effect must not be negligible in nuclei.

1.1.2 The nucleon-nucleon interaction

H. Yukawa proposed in 1935 his theory of the strong interaction, in which the interaction between two nucleons is seen as an exchange of a boson particle. As the interaction between two charged particles is an exchange of a photon, the interaction between two nucleons is affected by the exchange of one boson. Contrary to the electromagnetic interaction, the nucleon interaction appears to be short-range, this implies that the exchanged boson must have a finite mass. This mass is given by:

$$m = \frac{\hbar c}{r}, \tag{1.6}$$

with $r \approx 1$ fm the range of the interaction, we get $m \approx 197$ MeV. This particle was discovered in 1947 by César Lattes *et al.* [8] and was identified as the π meson with a mass about 140 MeV that corresponds to a more precise range of 0.7 fm. The associated Yukawa potential has the following form:

$$V_{Yukawa}(r) = -g^2 \frac{e^{-mr}}{r}, \tag{1.7}$$

where g is equal to the coupling constant between the meson field and the fermion field (proton or neutron). When we have $m = 0$, the interaction is Coulomb-like and is long-range.
Let us now define the main properties of the nucleon-nucleon interaction:

- it is invariant by parity,
- it is attractive,
- it is short range of the order of 0.7 fm,

- it has a hard core component so that the nuclear matter does not collapse. It is understood from the Pauli principle for identical nucleons and also for quarks of the same type within nucleons when the nucleons are different,

- it is spin-dependent,

- if we ignore the Coulomb interaction and the mass difference between the up and down quark, the total isospin is conserved and then it commutes with the Hamiltonian: $[H, T] = 0$. This is the charge independence property. The triplet $T = 1$ will be degenerate and the energy of the singlet $T = 0$ can be different from the triplet,

- it has a non central (tensor) component which has the following form:

$$S_{12} = 2\Big(3\frac{(\vec{S}.\vec{r})^2}{r^2} - S^2\Big) \tag{1.8}$$

- it contains a spin-orbit component: $V_{LS}\vec{L}.\vec{S}$,

- only the deuteron which is composed of one proton and one neutron forms a bound state with $S = 1$, $L = 0, (2)$ and $T = 0$ and respect the rule $L + S + T$ odd for two nucleons. None of the $T = 1$ triplet states are observed experimentally suggesting that the $T = 0$ channel is the strongest.

1.2 The Nuclear Shell-Model

It was observed experimentally, that nuclei with a certain number of protons and neutrons are particularly stable in comparison to their neighbours. This extra-stability is characterized by a high first 2^+ excited energy. The evolution of the first excited 2^+ states in even-even nuclei, as we can see in figure 1.1 shows us these numbers that provide extra-stability to the nucleus. These are the so-called magic numbers: 8, 20, 28, 50, 82, 126. This remarkable property was successfully described in the middle of the last century by Goeppert-Mayer, Haxel, Jensen and Suess [9, 10, 11] thanks to the introduction of the spin-orbit interaction. We shall stress here the main features of this shell model.

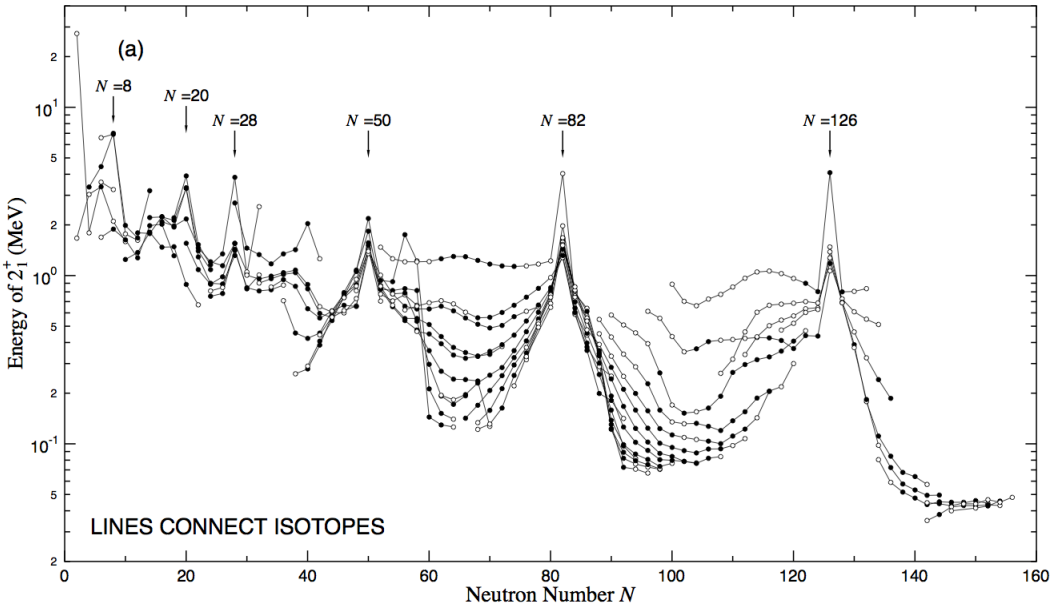

Figure 1.1: *Energy of the first 2^+ state in even-even nuclei [12], which highlights the presence of magic numbers in nuclei*

1.2.1 Independent-particle model

The first assumption of the nuclear shell model is based on the fact that each nucleon that compose the nucleus moves independently in a potential $U(r)$ that represents the average mean field due to the interaction with the other nucleons.
In order to access the nuclear properties of a nucleus composed of A nucleons, one has to solve the following Schrödinger equation:

$$H\Psi(1,2,...,A) = E\Psi(1,2,...,A) \tag{1.9}$$

where H is the Hamiltonian of the system. It contains the kinetic energy and the many-body interaction W. We shall limit ourselves to the two-body term of the interaction:

$$H = -\sum_{i=1}^{A} \frac{\hbar^2}{2m}\Delta_i + \sum_{i<j=1}^{A} W(i,j). \tag{1.10}$$

We can replace equation 1.10 by adding the mean potential felt by each individual nucleon:

$$H = \sum_{i=1}^{A} \Big(-\frac{\hbar^2}{2m}\Delta_i + U(i)\Big) + \sum_{i<j=1}^{A} W(i,j) - \sum_{i=1}^{A} U(i) = H^{(0)} + V, \tag{1.11}$$

where $H^{(0)} = \sum_{i=1}^{A} \Big(-\frac{\hbar^2}{2m}\Delta_i + U(i)\Big) = \sum_{i=1}^{A} h(i)$ is the sum of the single-particle Hamiltonian and V is the so-called residual interaction.
In the nuclear shell model framework, the solutions of the single-particle problem are used to construct a basis that will be used for the diagonalization of the residual interaction V.
To construct our basis that will serve for the diagonalization of the residual interaction, one may solve the Schrödinger equation for a spherically symmetric potential $U(r)$

$$h\phi = \Big(-\frac{\hbar^2}{2m}\Delta + U(r)\Big)\phi = \epsilon\phi. \tag{1.12}$$

We can separate the radial part from the angular part of the wave function:

$$\phi = \frac{u(r)}{r} F(\theta,\varphi). \tag{1.13}$$

It turns out that the angular part corresponds to a spherical harmonic: $F(\theta,\varphi) = Y_l^m(\theta,\varphi)$ and one has to solve the following radial equation:

$$-\frac{\hbar^2}{2m}\frac{d^2u}{dr^2} + \Big(\frac{\hbar^2}{2m}\frac{l(l+1)}{2} + U(r)\Big)u(r) = \epsilon u(r). \tag{1.14}$$

1.2.2 The nuclear shell-model potential

The form of the radial part of the wave function will depend on the potential used in the Hamiltonian. The classical nuclear Hamiltonian is composed of a harmonic oscillator, plus a centrifugal term and a spin-orbit term. The harmonic oscillator alone does not reproduce all the experimental magic numbers but only, 2, 8, and 20. The next one is 40 while the experimental one is 28. The addition of the spin-orbit term reproduces well all the experimental magic numbers and the single-particle Hamiltonian has the following

form:

$$h = -\frac{\hbar^2}{2m}\Delta + \frac{1}{2}m\omega^2 r^2 + f_{ll}\vec{l}.\vec{l} + f_{ls}\vec{l}.\vec{s}. \tag{1.15}$$

A schematic representation of the shell model is shown in figure 1.2. We can see that by adding the different terms, we reproduce the observed magic numbers that give extra stability for certain nuclei. In addition, we see that the magic numbers 28 and 50 appear due to the spin-orbit interaction.

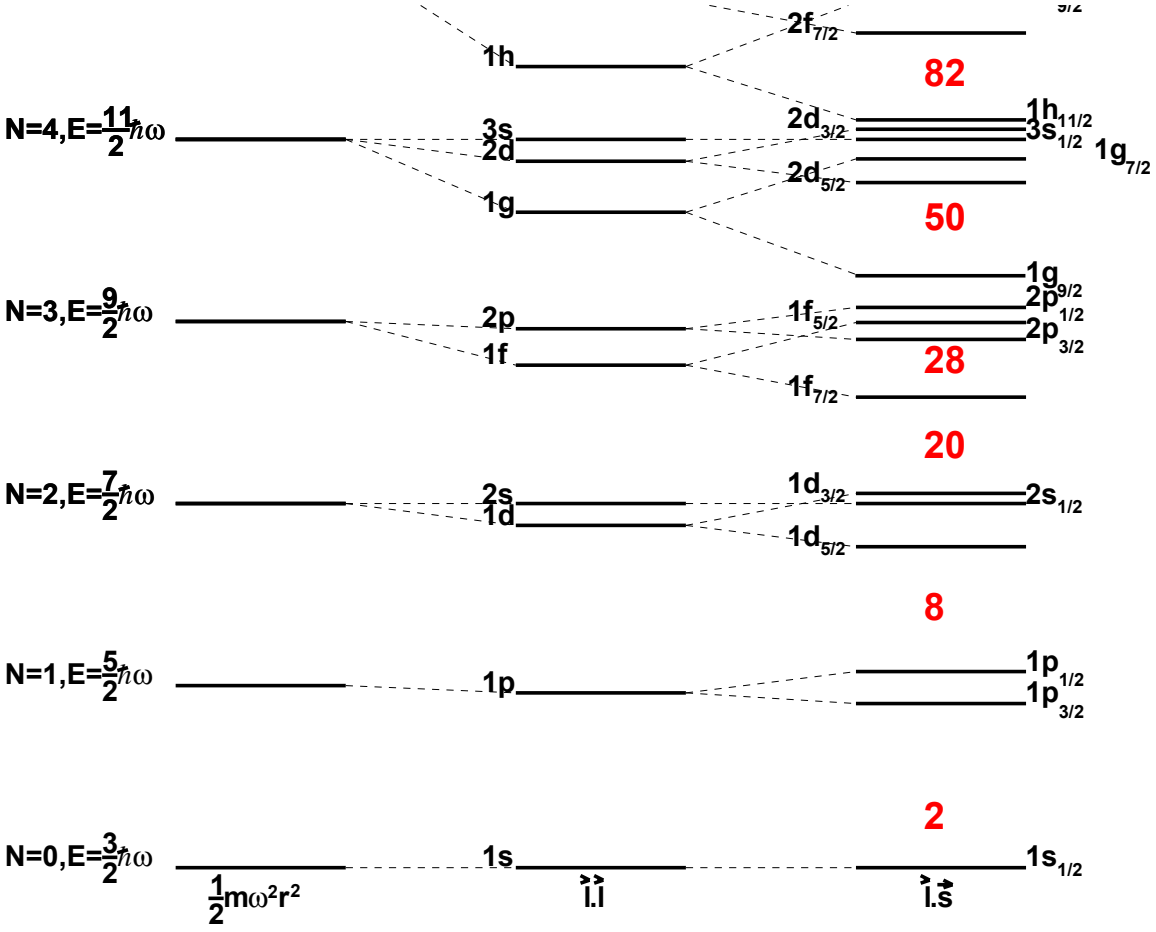

Figure 1.2: *Single-particle spectrum of the Hamiltonian 1.15*

1.2.3 The residual interaction

So far we did not treat the residual interaction:

$$V = \sum_{i<j=1}^{A} W(i,j) - \sum_{i=1}^{A} U(i). \tag{1.16}$$

We want to solve the entire Schrödinger equation, i.e. for the total Hamiltonian $H = H^{(0)} + V$. We assume to have a basis of many-body states by coupling single-particle states to good quantum numbers (J,T) where J corresponds to the good angular momentum coupling between j_1 and j_2, it is the same for the good total isospin T. These many-body states are eigenfunctions of $H^{(0)}$.

$$H^{(0)}\Phi_{JT,k} = E^{(0)}_{JT,k}\Phi_{JT,k}, \tag{1.17}$$

where k corresponds to other quantum numbers and the energy of a (J,T) state is the sum of single-particle energies

$$E^{(0)}_{JT,k} = \sum_{i=1}^{A} \epsilon_i. \tag{1.18}$$

Let us assume d is the number of basis states $|\Phi_k\rangle$. Then we need to solve the eigenvalue problem:

$$H\,|\Psi_p\rangle = E_p\,|\Psi_p\rangle\,, \tag{1.19}$$

where the wave function $|\Psi_p\rangle$ is a linear combination of the basis states

$$|\Psi_p\rangle = \sum_{k=1}^{d} a_{kp}\,|\Phi_k\rangle\,, \tag{1.20}$$

with the orthonormalization condition $\sum_{k=1}^{d} a_{kp}a_{kp'} = \delta_{pp'}$. So one has to solve

$$(H^{(0)} + V)\sum_{k=1}^{d} a_{kp}\,|\Phi_{kp}\rangle = E_p \sum_{k=1}^{d} a_{kp}\,|\Phi_{kp}\rangle\,. \tag{1.21}$$

By multiplying equation (1.21) by $\langle\Phi_l|$ we get

$$\sum_{k=1}^{d} a_{kp} \langle\Phi_l|(H^{(0)} + V)|\Phi_k\rangle = \sum_{k=1}^{d} E_p a_{kp} \langle\Phi_l|\Phi_k\rangle$$

$$\sum_{k=1}^{d} a_{kp} \langle\Phi_l|(H^{(0)} + V)|\Phi_k\rangle = \sum_{k=1}^{d} E_p a_{kp} \delta_{lk}.$$

We get a system of d equations

$$\sum_{k=1}^{d} H_{lk} a_{kp} = E_p a_{lp} \tag{1.22}$$

with

$$H_{lk} = \langle\Phi_l|H^{(0)} + V|\Phi_k\rangle = \langle\Phi_l|H^{(0)}|\Phi_k\rangle + \langle\Phi_l|V|\Phi_k\rangle$$

or

$$H_{lk} = E_k^{(0)} \delta_{lk} + V_{lk}.$$

One has to diagonalize the matrix H_{lk} in order to solve this eigenproblem and get the eigenvalues E_p associated to the coefficients a_{kp}.
In shell-model calculations, to solve this many-body problem, we divide the space in three subspaces:

- the core, which corresponds to the orbits which are always full,
- the valence space, which are all the available orbitals for the valence nucleons,
- and the external space, which are the orbitals above the valence space that remain always empty.

The valence space depends on the region we are interested in the Segré chart. Because we are in a truncated Hilbert space in shell-model calculation, the residual interaction corresponds to an effective interaction that should reproduce the properties of the region of interest.

1.2.4 Structure of the effective interaction

The goal of the modern shell model is to describe the nuclear structure properties using microscopic effective interaction. To derive the effective interaction, the starting point is the bare NN two-body force using a realistic NN potential and then we get the microscopic effective interaction via a given renormalization procedure based on G-matrix or using a low-momentum interaction V_{low-k} [13] with further addition of in-medium many-body effects using perturbation theory. However such effective interactions have a problem since they do not give rise to the correct saturation and shell gaps observed in nuclei, especially the spin-orbit magic numbers.
As it was shown by Dufour and Zuker [14], it can be useful to decompose the effective Hamiltonian as follows:

$$H = H_m + H_M, \tag{1.23}$$

where H_m is the monopole term of the Hamiltonian that represents a spherical mean field and is responsible for the global saturation properties and spherical single-particle energies while H_M is the multipole term that contains all the correlations such as the pairing, the quadrupole or the octupole terms. We can write the following property for a closed-shell nucleus (CS):

$$\langle CS \pm 1|H|CS \pm 1\rangle = \langle CS \pm 1|H_m|CS \pm 1\rangle\,, \tag{1.24}$$

which means that for closed shell nuclei $\pm$ 1 particle, only the monopole part of the Hamiltonian is non-zero.
In the isospin representation, we have:

$$H_m = \sum_{i,\tau} n_{i,\tau}\epsilon_{i,\tau} + \sum_{i,j,\tau,\tau'} V_{ij}^{\tau\tau'} \frac{n_{i\tau}(n_{j\tau'} - \delta_{ij}\delta_{\tau\tau'})}{1+\delta_{ij}\delta_{\tau\tau'}} \tag{1.25}$$

with the monopole interaction:

$$V_{ij}^{\tau\tau'} = \frac{\sum_J V_{ijij}^{J,\tau\tau'}(2J+1)\Big(1+(-1)^J\delta_{ij}\delta_{\tau\tau'}\Big)}{(2j_i+1)\Big(2j_l+1-\delta_{ij}\delta_{\tau\tau'}\Big)}, \tag{1.26}$$

where i, j denote the valence orbitals and τ stands for proton or neutron.
The effective-single-particle energies (ESPE) of one orbit is defined as the one-proton(neutron) separation energy of this orbit, where the energy is calculated with the monopole interaction as given in equation 1.25 [15].
To overcome the problem of the effective interaction mentioned earlier, an adjustment of the monopole term is imposed to be in agreement with the spectroscopic data. Those phenomenological monopole corrections are due to take into account the three-body force in the effective interaction (in a truncated space). Nevertheless promising work is currently done [16] to take into account the three-body force in the realistic interaction.

2

Physics of neutron-rich nuclei in the region of $Z = 28$

Contents

In the last two decades, experiments with exotic beams made possible the study of the evolution of the shell gaps far from stability. The measurements showed some surprisingly changes in nuclear shell structure. These evolutions are driven by the monopole part of the effective interaction whose interplay with the correlations (pairing, quadrupole...) can lead to rapid structure changes. As we said, the monopole part is responsible for the

change of the ESPE and it was shown that its tensor term could play a significant role [17].
An example of proton-shell evolution in exotic nuclei is the breakdown of the $Z = 8$ shell closure in the unbound ^{12}O measured by D. Suzuki *et al.* [18]. In this work they measured through the ^{14}O(p,t)^{12}O transfer reaction a low $0^+(2^+)$ excited state at 1.8 MeV pointing out the quenching of the gap. This quenching is particularly interesting since in the ^{12}Be mirror nucleus, a breakdown of the $N = 8$ shell closure has been measured by measuring single-particle states in ^{11}Be through knock-out reaction by N. Alahari *et al.* [19]. The mirror symmetry of shell quenching is then demonstrated. The low-mass region is indeed particularly interesting to test the mirror symmetry since it is not possible for medium-mass to access the mirror nuclei of the neutron-rich region.
The region of ^{78}Ni ($N/Z \approx 1.8$) is of great interest nowadays in nuclear physics and the question of its doubly magic character remains open. From ^{68}Ni to ^{78}Ni the neutron orbit $\nu g_{9/2}$ is filling up. This addition of neutrons could polarize the proton core because of the proton-neutron interaction and then modify the $Z = 28$ shell gap between the $\pi f_{7/2}$ and $\pi p_{3/2}$ (or $\pi f_{5/2}$) orbitals. Moreover the tensor interaction between neutron and proton could play an important role in this region and modify the shell gaps toward ^{78}Ni [20]. We can notice that it is very similar as the case of shell evolution in silicon isotopes where it was observed evidences of the disappearance of the $Z = 14$ and $N = 28$ shell closures in ^{42}Si [21]. Indeed, the evolution of the spin-orbit splitting $\pi d_{5/2} - \pi d_{3/2}$ is probed with the neutron filling of the $\nu f_{7/2}$ orbital. These shell quenching are ascribed to the action of the proton-neutron tensor forces. Since ^{42}Si is the analogous nucleus of ^{78}Ni, one can wonder about the doubly magic character of ^{78}Ni. Finally, the spectroscopic data is very important to constrain the shell model effective interaction in this region.
We shall focus on the $Z = 28$ shell gap toward this key nucleus. The aim of this work is to investigate the change of proton shell structure of neutron-rich Copper isotopes via transfer reaction and to understand the mechanism at stake behind the change of structure using shell model calculation.

2.1 The neutron-rich Copper region

2.1.1 Experimental $E(2_1^+)$ in Nickel isotopes

The evolution of the energy of the first 2_1^+ in an isotopic chain is a valuable clue to

see the appearance of a shell gap. In figure 2.1 we can see the evolution of the first 2_1^+ state between ^{54}Ni and ^{72}Ni. The values are taken from reference [22] for $^{54-68}$Ni and from [23, 24] for $^{70-72}$Ni. One can clearly see the doubly-magic character of ^{56}Ni and ^{68}Ni. By measuring the first 2_1^+ in ^{78}Ni we should see the persistence or not of the $N = 50$ and $Z = 28$ gaps and test the robustness of these gaps. However, no value is currently known for $E(2_1^+)$.

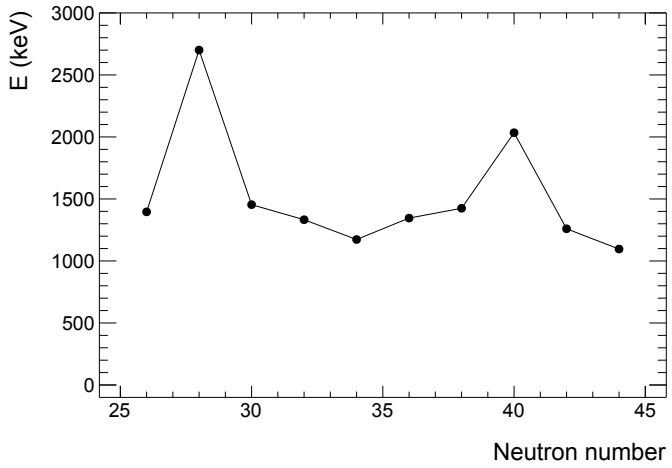

Figure 2.1: *Experimental $E(2_1^+)$ values in Ni isotopic chain [22, 23, 24, 25]*

2.1.2 Binding energies

The evolution of the proton-separation energy in an isotopic chain can give us a hint about the evolution of the gap with the neutron number. In figure 2.2 one can see the evolution of the proton-separation energy S_p for Copper isotopes ($Z = 29$) in blue and for Nickel isotopes ($Z = 28$) in red. The values are taken from the new atomic mass evolution [26]. In figure 2.3, we can see the difference of the S_p between Nickel and Copper isotopes, which corresponds to the correlated gap. We have to note that the masses are known up to $N = 44$, the last three points in both figures are not measured but are estimated. From this figure we clearly see the higher binding energy (equation 1.1) for $N = 28$ and $N = 40$ that tells us about the magic character of ^{56}Ni and ^{68}Ni. Above $N = 40$ the binding energy starts decreasing until $N = 44$ that might suggest a possible reduction of the gap.

This trend can also be caused by correlations present in the mid-shell nucleus ^{72}Ni and is not necessarily an indicator of changes in the shell structure.
To investigate the $Z = 28$ gap evolution, Copper isotopes are very good candidates as they are composed of one proton outside a Nickel core. They have been studied extensively both experimentally and theoretically. Neutron-rich Copper isotopes have been studied already in the 70's through transfer reactions in direct kinematics and since the 90's more neutron-rich nuclei have been investigated thanks to the development of radioactive ion beam facilities. A review on the topic and on the magic number evolution has been given by Sorlin and Porquet [27]. We shall detail here the more neutron-rich Copper isotopes.

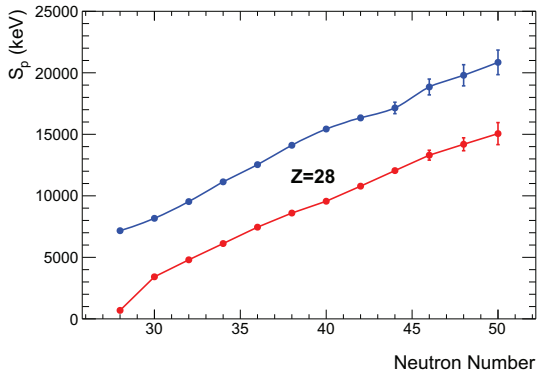

Figure 2.2: *Proton separation energy as a function of neutron number in red for the Nickel isotopes and in blue for the Copper isotopes [26]*

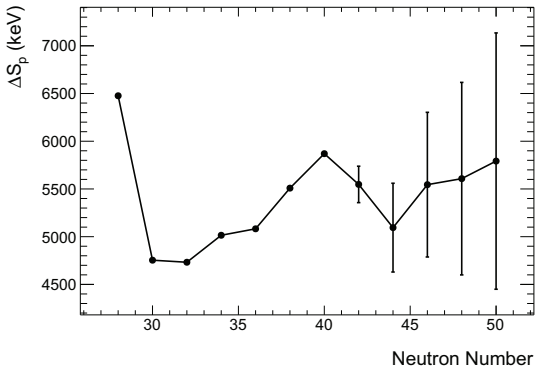

Figure 2.3: *Difference of proton-separation energies between Copper and Nickel giving a hint of the $Z = 28$ gap evolution toward the ^{78}Ni*

The graphical method

We already saw in the motivation the evolution of the $Z = 28$ gap in figure 2.3 through the proton separation energy S_p difference (Koopman's theorem) between Zinc (Z) and Copper ($Z + 1$):

$$\Delta S_p = S_p(Z) - S_p(Z + 1) \approx \epsilon_{p_{3/2}}(Z, N) - \epsilon_{f_{7/2}}(Z, N). \tag{2.1}$$

The single-particle energies in Copper $(Z+1)$ are slightly shifted from their position in Nickel (Z) by an amount $\Delta\epsilon$ as it is shown in figure 2.4:

$$\epsilon_{p_{3/2}}(Z+1,N) = \epsilon_{p_{3/2}}(Z,N) + \Delta\epsilon. \tag{2.2}$$

One way to determine this shift is the so-called graphical method. This prescription is explained by Heyde *et al.* in reference [28]. ΔS_p has to be corrected by applying the graphical method as it is represented in figure 2.5 by ΔS_p^{ext}:

$$\Delta S_p^{ext} = S_p(^A Ni) - S_p^{ext}(Z=28) \tag{2.3}$$

$S_p^{ext}(Z=28)$ is the extrapolated linear function at $Z=28$ which fit the proton separation energy of $(A+1,Z+1)$, $(A+3,Z+3)$, $(A+3,Z+5)$ nuclei where (A,Z) refers to the Nickel isotope. ΔS_p^{ext} is the quantity which estimates better the gap. By applying this graphical method, one can see in figure 2.6 the evolution of ΔS_p^{ext} in red. We see that the difference between ΔS_p and ΔS_p^{ext} is minimum at $N=28$ because of the character doubly magic of this nucleus, while the difference is the highest for $N=32$ and $N=44$ where the collectivity is enhanced and because it corresponds to open shell nuclei.

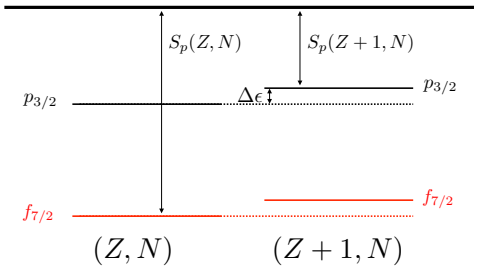

Figure 2.4: *Representation of the changes induced in the proton single-particle energy*

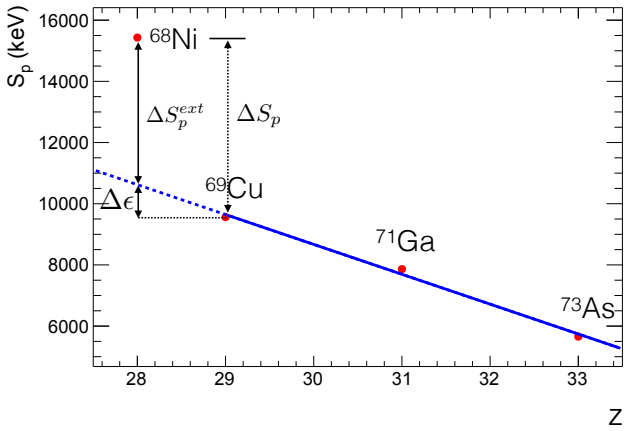

Figure 2.5: *Graphical method in order to obtain the particle-hole energy in Copper isotope*

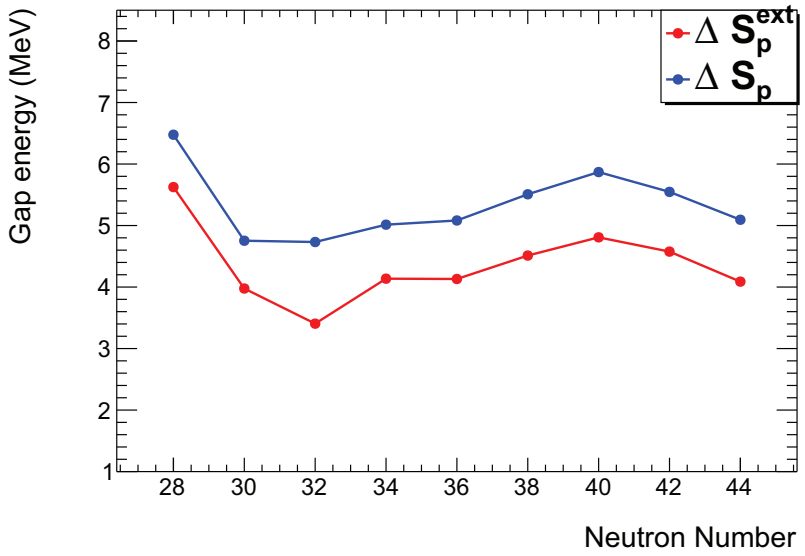

Figure 2.6: *Evolution in Copper isotopes of the* ΔS_p *in blue and* ΔS_p^{ext} *in red*

In addition, another quantity which is interesting to look at the evolution is the nucleon pairing energy defined as:

$$\Delta E_{pairing} = 2S_p(Z+1, N) - S_{2p}(Z+2, N) \tag{2.4}$$

where $(Z + 1)$ corresponds to a Copper isotope and $(Z + 2)$ to a Zinc isotope. In table 2.1 are listed the pairing energy $\Delta E_{pairing}$ for the different isotopes and the estimated gap through the graphical method. We can note that for $N < 40$ $\Delta E_{pairing} \approx 1.5$ MeV while beyond $N = 40$ the pairing energy gain about 0.5 MeV to reach 2 MeV, which is the sign that an orbital of higher l becomes closer. This might correspond to the drop in energy of the $\pi f_{5/2}$ orbital which is known in Copper isotopes.

N	$\Delta E_{pairing}$ (MeV)	ΔS_p^{ext} (MeV)	$\Delta\epsilon$ (MeV)
28	-1.588	5.625	0.851
30	-1.686	3.976	0.777
32	-1.672	3.405	1.327
34	-1.591	4.136	0.878
36	-1.471	4.131	0.951
38	-1.376	4.512	0.996
40	-1.556	4.808	1.061
42	-1.937	4.576	0.971
44	-2.008	4.088	1.006

Table 2.1: *Details about the pairing corrections and the extrapolated separation energy difference*

2.1.3 Experimental status in neutron-rich Copper isotopes

At the end of the 90's, the main characteristic observed in neutron-rich Copper isotopes above $N = 40$ was the strong decrease in energy of the first $5/2^-$ state in ^{71,73}Cu. This work was performed by Franchoo *et al.* by β-decay of ^{71,73}Ni [29, 30]. Moreover odd-A $^{67-73}$Cu were investigated by Coulomb excitation with radioactive beams at ISOLDE by Stefanescu *et al.* [31]. In this work the transition probabilities $B(E2 : 5/2^- \rightarrow 3/2^-_{gs})$ were measured and a reduction of the $B(E2)$ was observed for $N \geq 40$ pointing to a single-particle character for the $5/2^-$ state beyond $N \geq 40$ ($B(E2) < 5$ W.u.) while it is somewhat more collective for $N < 40$ ($B(E2) > 10$ W.u.) (see figure 2.7). This is consistent with the small spectroscopic factors in ^{63,65,67}Cu for the $5/2^-$ state (0.5, 0.55 and 0.3 respectively [32]).
Flanagan *et al.* by means of collinear laser spectroscopy performed at ISOLDE [33] have shown a spin inversion for the ground state: the ground state becomes $5/2^-$ in ^{75}Cu while it is a $3/2^-$ ground state for lighter odd-Copper isotopes. Then if we assume that beyond $N = 40$ the $5/2^-$ state corresponds to a pure proton particle configuration (figure 2.8), we can say that from $N = 40$ to 46 there is a decrease in energy between $\pi f_{5/2}$ and $\pi p_{3/2}$. This behavior appears as soon as we start filling the $\nu g_{9/2}$ orbital. This suggests a possible reduction of the proton gap towards ^{78}Ni. It is well established that there is a

strong monopole shift of the $\pi f_{5/2}$ orbital beyond $N = 40$ [29, 30] while the situation for its spin-orbit partner ($\pi f_{7/2}$ orbital) is not so clear.

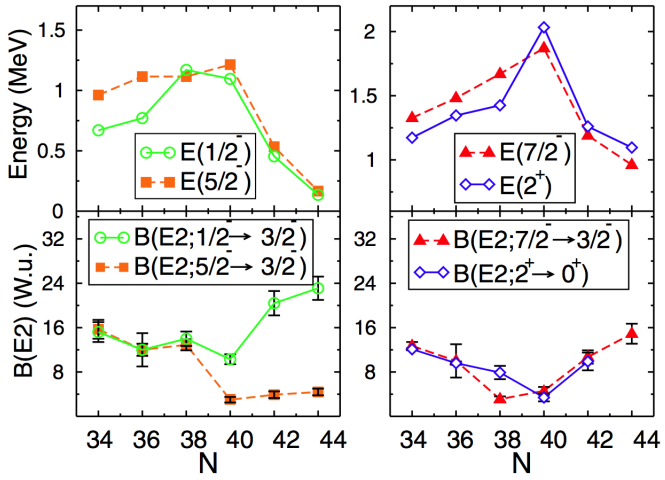

Figure 2.7: *Systematics of the energies of the lowest* $1/2^-$, $5/2^-$ *and* $7/2-$ *states in* $^{63-73}$*Cu along with the* 2^+ *levels in the even-even* $^{62-72}$*Ni, and the associated experimental* $B(E2)$ *values [31]*

The position of the $\pi f_{7/2}$ orbital in Copper isotopes is linked to the size of the $Z = 28$ shell gap. Because its strength can be fragmented, it is interesting to perform transfer reactions in order to extract the spectroscopic factors of each $7/2^-$ state and then calculate the centroid of the strength. For this purpose pick-up reactions were done up to ^{69}Cu in direct kinematics. Zeidman and Nolen performed (d,^{3}He) pick-up reaction [32] while Ajzenberg-Selove *et al.* performed $(\vec{t}, \alpha)$ pick-up reaction using a polarized triton beam [34]. The advantage of polarized beam is that we can distinguish the spin of a state with the shape of the analysing power A_y that is different between $5/2^-$ and $7/2^-$ for instance while we know only the angular momentum L for an unpolarized beam.

At $N = 40$ for ^{69}Cu, two $7/2^-$ states are assigned at 1712 and 1872 keV respectively. From Zeidman's experiment [32] we know that the first state has a quite high spectroscopic factor ($C^2S = 2.7$) while the second state has a small one ($C^2S = 0.45$). Then the state at 1712 keV is interpreted to be mainly proton-hole state $\pi f_{7/2}^{-1}$ while the one at 1872 keV is interpreted as the coupling between the single proton in the $\pi p_{3/2}$ orbital with the 2^+

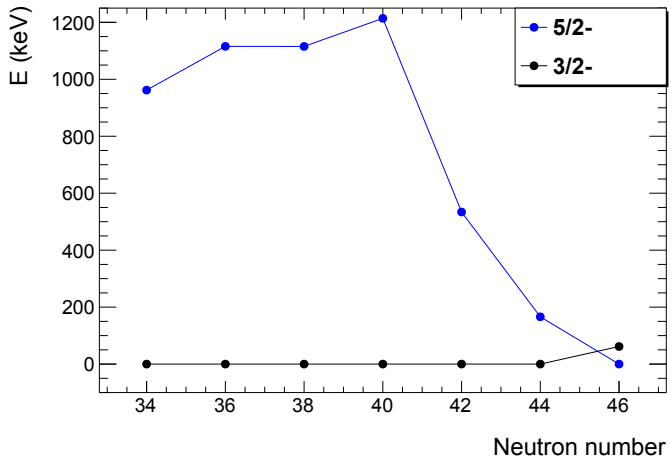

Figure 2.8: *Evolution of the first* $3/2^-$ *and* $5/2^-$ *states in Copper isotopes*

of the Nickel core: $|7/2^-\rangle = |2^+ \otimes p_{3/2}\rangle$ as it is explained by Ishii *et al.* [35]. Only these two states were measured in Zeidman's work that correspond to only 40% of the strength, meaning that most of the proton-hole strength lies at higher energy. Moreover in those transfer experiments the $5/2^-$ state at 1214 keV has a very large spectroscopic factor ($C^2S = 1.5$ for Zeidman and $C^2S = 1.2$ for Ajzenberg-Selove) while we do not expect to have so much proton in the $\pi f_{5/2}$ orbital in ^{70}Zn. The peak of interest is broader than the others and the authors assume that there are two levels in this peak that correspond to a $5/2^-$ and $7/2^-$ doublet. Then the spacing of these two unresolved states is less than 15 keV. Nevertheless no other state has been observed around this energy in β decay while this decay should populate such a state because of the ground state of ^{69}Ni which is $I^\pi = 9/2^+$. The conclusion about the $5/2^-$ state thus remains unclear in ^{69}Cu.
For ^{71}Cu, no spectroscopic factors were known, but two $7/2^-$ states are assigned at 981 keV and 1190 keV. In deep inelastic collisions Ishii *et al.* [36] populated a $19/2^-$ microsecond isomer that feed the $7/2^-$ state at 1190 keV in a $E2$ cascade. From that a $7/2^-$ assignment was made for the state at 1190 keV. This isomer was also populated by Grzywacz *et al.* [37] by producing Copper isotopes through the reaction of ^{86}Kr on a ^{nat}Ni target. In this experiment only the 1190 keV was seen through the decay of the isomer. Concerning the state at 981 keV, based on the value of the log ft (>5.9) in β decay of ^{71}Ni which has a $9/2^+$ configuration, and based on the similar pattern between ^{69}Cu and ^{71}Cu, a spin and parity of $7/2^-$ was suggested. Moreover, Stefanescu *et al.* [31] in Coulomb excitation populated

only the state at 1190 keV. Based on particle-core coupling model [38] this state was interpreted to be $|7/2^-\rangle = |2^+ \otimes p_{3/2}\rangle$ coupling while the state at 981 keV was interpreted to have a single-particle character. The only experimental data for the state at 981 keV is reported by Franchoo *et al.* from β-decay [29, 30] and more recently by Doncel *et al.* [39]. In the latter case, in-beam γ-ray spectroscopy was performed using the multi-nucleon transfer reaction ^{76}Ge + ^{238}U at Legnaro with the AGATA demonstrator in combination with the PRISMA magnetic spectrometer. From the measurement through the recoil distance Doppler-shift method, the value was obtained for the half-life of $7/2^- \rightarrow 3/2^-_{gs}$ transition at 981 keV that is $t_{1/2} = 13.9 \pm 11.1$ ps giving a value of $B(E2) = 3 \pm 2$ W.u. From that value, they conclude a single-particle character of the state. However the errors are very large and no spectroscopic factors are known in ^{71}Cu. It seems very important to perform a transfer reaction to extract spectroscopic factors for the populated states in this nucleus, to establish the characteristics of the state at 981 keV and to estimate the centroid of the $\pi f_{7/2}$ strength.
To conclude, one can see in figure 2.9 the systematic of the first $3/2^-$ and $5/2^-$ and $7/2^-$ states in Copper isotopes where the spectroscopic factors are given up to ^{69}Cu from reference [32]. In this same figure the systematic of the 2^+_1 in Ni isotopes is also reported. The dashed line corresponds to the $7/2^-$ in Cu isotopes with a large value of $B(E2)$. These states correspond to the coupling between the 2^+ of the Nickel core with the single proton in the $\pi p_{3/2}$ orbital: $|2^+ \otimes p^1_{3/2}\rangle$. It is now important to quantify the spectroscopic value of each $7/2^-$ states in ^{71}Cu to determine the centroid of the $\pi f_{7/2}$ strength.

Experimental similarities in gallium isotopes

The gallium isotopes with three protons in the $2p_{3/2}$ orbital contain two more protons with respect to Copper isotopes. The ^{70,72,74,76}Ge(d,^{3}He)^{69,71,73,75}Ga pick-up reaction was performed by Rotbard *et al.* [40]. In this work they extracted 25% to 38% of the $\pi f_{7/2}$ strength and we can see the evolution of the measured centroid in figure 2.10 in red. In this figure we also see the evolution of the $5/2^-$ experimental centroid for ^{69,71,73,75}Ga [40], from what they have measured, while for ^{77,79,81}Ga only the energy of the first $5/2^-$ state is plotted [41, 42]. We see a drop in energy as soon as we start filling the neutron $g_{9/2}$ orbital, and the inversion between $5/2^-$ and $3/2^-$ was proposed at $N = 50$ for ^{81}Ga by Verney *et al.* [41]. Even though the drop in energy of the $5/2^-$ is less drastic than in the Copper isotopes the trend is the same and the inversion seems also to occur. However,

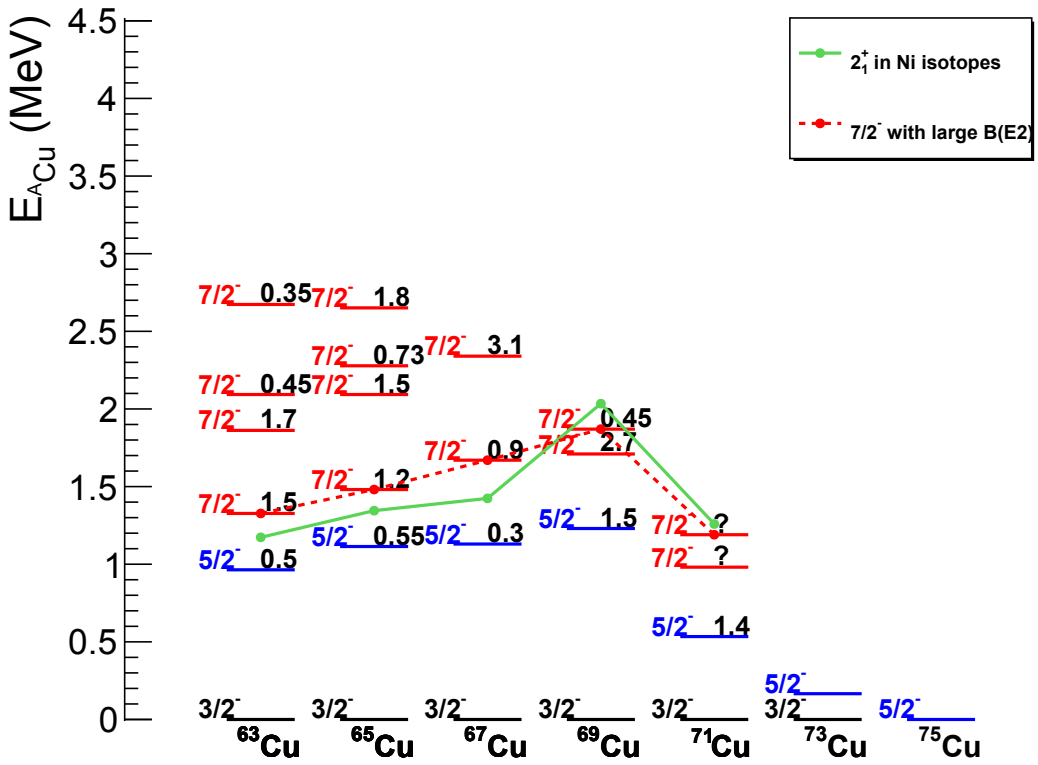

Figure 2.9: *Systematic of the first* $3/2^-$ *and* $5/2^-$ *and* $7/2^-$ *states in Copper isotopes and systematic of the* 2_1^+ *in Ni isotopes*

from the data the trend of the $7/2^-$ when filling the $\nu g_{9/2}$ orbital is not so clear especially because we miss most of the strength. However, it seems that the behavior of the $5/2^-$ shift looks similar between Copper and Gallium isotopes beyond $N = 40$ suggesting that the same phenomena could be at stake in these nuclei. However one has to be careful about the conclusion because the three protons in $p_{3/2}$ ($f_{5/2}$) orbits can couple to $3/2^-$, $5/2^-$ or $7/2^-$ states, which are different from single-particle orbitals. Then the evolution of the $\pi f_{7/2}$ orbital in the neutron-rich gallium isotopes could bring us new information about the evolution of the $Z = 28$ gap. However a lot of strength is missing because the force is more fragmented. In addition the Copper isotopes are closer to a closed shell,

where we can assume a more single-particle character of the levels. It should thus be easier to infer the shell evolution from the Copper isotopes.

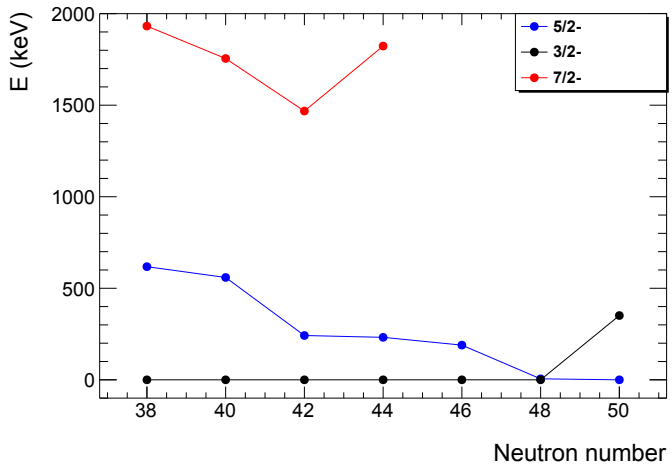

Figure 2.10: *Evolution of the first* $3/2^-$ *state, the* $5/2^-$ *experimental centroid is plotted for* ^{69,71,73,75}*Ga while it is only the first* $5/2^-$ *state for* ^{77,79,81}*Ga, and the* $7/2^-$ *experimental centroid is plotted for* ^{69,71,73,75}*Ga [40, 41, 42]*

2.1.4 Overview of theoretical calculations

The theoretical work on the Copper isotopes has been very rich as well. I shall summarize here some results within the shell-model framework.
First shell-model calculations were performed by Smirnova *et al.* [43] using a valence space composed of $2p_{3/2}$, $1f_{5/2}$, $2p_{1/2}$ and $1g_{9/2}$ orbitals. They reproduce the first states $3/2^-$, $5/2^-$ and $1/2^-$ but the valence space used cannot reproduce the $7/2^-$ hole-state coming from a hole in the $\pi f_{7/2}$ orbital. In this work the $5/2^-$ state is systematically about 600 keV higher compared to experiment, however the slope of the decrease in energy is the same. The calculations predict an inversion between $\pi f_{5/2}$ and $\pi p_{3/2}$ for $N = 50$ while it occurs at mid-shell for $N = 46$, i.e ^{75}Cu. In the paper of Sieja and Nowacki [44], the theoretical calculations correctly reproduce this inversion and shell evolution from ^{68}Ni to ^{78}Ni is discussed in detail where the systematics of the low-lying states and magnetic moments are obtained in good agreement with the experimental data. This is due to the

inclusion of more proton degrees of freedom, indeed the $\pi f_{7/2}$ is included in the valence space while previous shell-model calculations used a ^{56}Ni core. In this work the $Z = 28$ shell gap is reduced by about 0.7 MeV when the $g_{9/2}$ neutron orbital is filled from ^{68}Ni to ^{78}Ni.

Since experimentally there is a strong downward monopole shift of the $\pi f_{5/2}$ orbital, it is clear that the interaction $V^{pn}_{f_{5/2}g_{9/2}}$ is attractive. A simple explanation of this effect has been provided in terms of tensor force by Otsuka [17, 20]. The effect of the tensor force was also investigated by and Smirnova *et al.* [45, 46]. The structure of the tensor force is:

$$S_{12} = \frac{3}{r^2}(\vec{\sigma_1}.\vec{r})(\vec{\sigma_2}.\vec{r}) - \vec{\sigma_1}.\vec{\sigma_2} \propto \left[S^{(2)}.Y^{(2)}\right]^{(0)} \tag{2.5}$$

where $S^{(2)} = [\sigma_1^{(1)} \otimes \sigma_2^{(1)}]^{(2)}$. Because the spin operators are coupled to rank 2, the total spin S of the two interacting nucleons must be $S = 1$ otherwise the tensor force is null. This tensor force is analogous to the interaction between a magnetic field $\vec{B}_1$ produced by a dipole $\vec{\mu}_1$ with another dipole $\vec{\mu}_2$. The effect of this tensor force on the evolution of nuclear shells is well discussed in [17]: Let us denote by $j^\nu_> = l^\nu_> + 1/2$ the orbital that is filled by the neutrons (in our case it corresponds to the $\nu g_{9/2}$ orbital), $j^\pi_> = l^\pi_> + 1/2$ corresponds to $\pi f_{7/2}$ and $j^\pi_< = l^\pi_< - 1/2$ corresponds to $\pi f_{5/2}$. We have the following relation:

$$(2j^\pi_> + 1)V^{\pi\nu}_{j^\pi_>,j^\nu_>} + (2j^\pi_< + 1)V^{\pi\nu}_{j^\pi_<,j^\nu_>} = 0. \tag{2.6}$$

This equation means that the interaction is stronger in the case $j^\nu_>$ and $j^\pi_<$ than in the case $j^\nu_>$ and $j^\pi_>$ (figure 2.12). In our case we have:

$$V^{\pi\nu}_{\frac{5}{2},\frac{9}{2}} = -\frac{4}{3}V^{\pi\nu}_{\frac{7}{2},\frac{9}{2}}. \tag{2.7}$$

The interaction is attractive between $j^\nu_>$ and $j^\pi_<$ while it is repulsive between $j^\nu_>$ and $j^\pi_>$. We can see a schematic view of this effect in figure 2.11. One can see that this tensor force can have an important impact on the $Z = 28$ gap between $N = 40$ and $N = 50$ while the $\nu g_{9/2}$ neutron orbital is filling up. Especially at $N = 50$, the gap is precisely the spin-orbit gap while at $N = 40$ the gap corresponds to the energy distance between $\pi f_{7/2}$ and $\pi p_{3/2}$ orbitals. In [17] the distance in energy between the effective single particle energy $1f_{5/2}$ and $1f_{7/2}$ is reduced about 2.3 MeV between $N = 40$ and $N = 50$ (from 3.8 MeV to 1.5 MeV).

One other important effect that is intensively discussed nowadays is the three-body force.

Smirnova *et al.* [46] performed spin-tensor decomposition of an effective two-body shell-model interaction in order to quantify the role of different terms of this interaction in the evolution of the shell gaps in the $T = 1$ channel (neutron-neutron or proton-proton interaction). A spin-tensor decomposition is the expansion of an interaction V as a sum of scalar, vector and rank-2 spherical tensor. Moreover a comparison is done between microscopic effective interaction and phenomenological effective interaction in different valence spaces. The microscopic effective interaction does not reproduce the right shell-gap while the adjusted realistic interaction reproduce them. By comparing the different terms of the spin-tensor decomposition for the two different interactions it can provide a quantitative insight into the role of $3N$ components giving rise to the spin-orbit shell closure. The conclusion of these works is that the central and the vector parts of the interaction are the most sensitive to the effect of the three-nucleon forces while the tensor part is not affected much.

In this work, we are interested in the $Z = 28$ gap evolution with the neutron filling, between $N = 40$ and $N = 50$. Thus we will probe the proton-neutron interaction and in this case it is expected that the shell evolution is mainly driven by the tensor force and not by the $3N$ forces. From the spin-tensor decomposition we know that the tensor force acts mainly on the monopole part of the interaction and not on the multipole part.

The extraction of spectroscopic factors of $7/2^-$, $3/2^-$ and $5/2^-$ states giving the centroid of the strength along the isotopic Copper chain towards $N = 50$ can provide a strong constraint on the interaction that is at stake in this region of the nuclear chart and especially it will probe the strength of the tensor force.

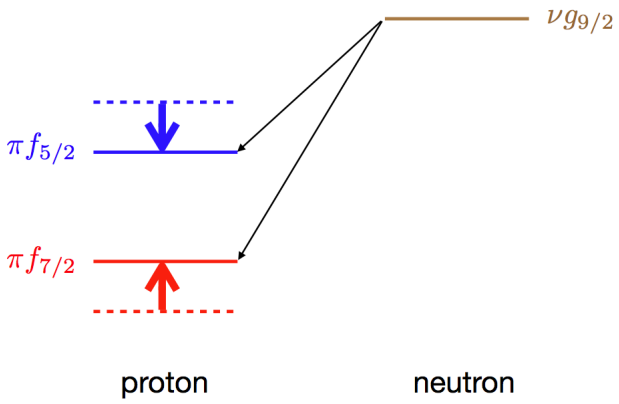

Figure 2.11: *Schematic picture of the monopole interaction produced by the tensor force between $\nu g_{9/2}$ and πf orbitals*

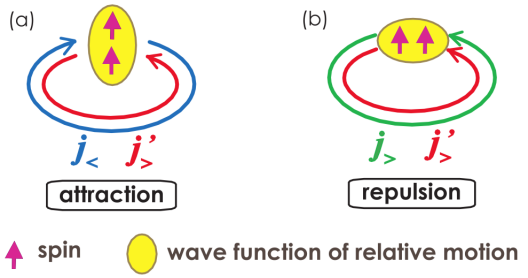

Figure 2.12: *Schematic picture of the tensor force acting between two nucleons on orbit j and j' [17]*

3

Experimental method: the (d,^{3}He) pick-up reaction

Contents

To study the proton-hole strength in the Copper isotopes we have performed (d,^{3}He) transfer reaction where one proton is exchanged between the beam and the target. One proton is removed from Zinc that enables us to probe the proton-hole states in Copper.

A transfer reaction is a direct process where one or several nucleons are exchanged between the beam and the target. These reactions are studied between a few MeV to tens of MeV per nucleon. It is a very powerful tool for nuclear spectroscopy: it can give the energy within limit of resolution, the spin and parity when the beam is polarized and in general the angular momentum and we can also determine the spectroscopic factor of a given state. In our case of the (d,^{3}He) reaction, a proton is exchanged between the beam and the target as we can see in figure 3.1. We want to measure the $f_{7/2}$ proton-hole strength through this pick-up reaction by extracting for each populated state its spectroscopic factor.

3.1 Spectroscopic factor

3.1.1 Definition

The spectroscopic factor was introduced to relate transfer reaction and nuclear structure. From a theoretical point of view we define it as the overlap between a nucleus of A nucleons in an initial state $|\phi_0^A\rangle$ and a nucleus with $A \pm 1$ nucleons in the final state k $|\phi_k^{A\pm1}\rangle$:

$$S_\pm = \int |\langle \phi_0^{A\pm1} | a^{(\dagger)} | \phi_0^A \rangle|^2 d\mathbf{r}, \tag{3.1}$$

where $a^{(\dagger)}$ is the creation or annihilation operator. This spectroscopic factor $S_\pm$ tells us how the nucleus $A \pm 1$ can be modeled as a core ϕ_0^A plus a hole or a particle. In other words, it measures the degree to which a state populated in a transfer reaction is a single-particle state. Although this quantity is a usual extraction for the experimentalist, it is not an observable since it is not conserved through a unitary transformation [47, 48]. The observable is the cross section, from what we extract a spectroscopic factor using a given reaction model. Even if we are aware of this problem that $H_{shellmodel} \neq H_{reaction}$ and that we are model dependent when we extract spectroscopic factors, we shall do it here for

both nuclei in a consistent way in order to be able to compare the results in the same model framework.

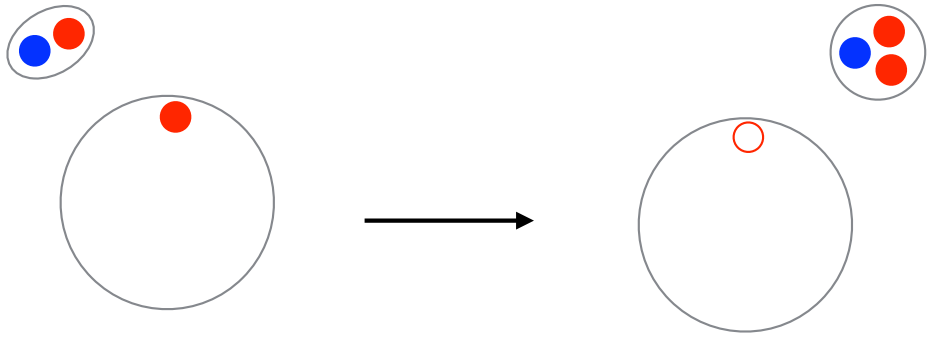

Figure 3.1: *Pick-up reaction scheme where a proton is exchanged between the beam and the target*

3.1.2 Extraction of the experimental spectroscopic factor

In the case of a direct reaction, to extract the experimental spectroscopic factor, one has to compare the theoretical cross section to the experimental one. In the case where only one orbital contributes to the final state, we have:

$$C^2 S_{exp} = \frac{\sigma_{exp}}{\sigma_{th}^{sp}} \tag{3.2}$$

where C^2 corresponds to the isospin Clebsch-Gordan and σ_{th}^{sp} is the theoretical cross section for a single transfer particle. We see clearly that $C^2 S_{exp}$ depends on the model of reaction used. It is then very important to understand and describe the reaction model used. To do so we shall use the Distorted-Wave Born Approximation (DWBA) that is explained in the next section.
Once we have extracted the experimental $C^2 S_{exp}$ we can compare it with the theoretical one $C^2 S_{th}$ calculated in the shell-model formalism.

3.2 Distorted-Wave Born Approximation

Before explaining the different approximations leading to the DWBA model, it seems important to remind some aspects and general results about scattering theory. Of course this reaction model is well explained in several books and lectures for example by Norman K Glendenning [49] and Eric Bauge [50].

3.2.1 Scattering theory and general results

General results

First, I would like to remind the differential cross section of an elastic scattering process. Let's start with the following process :

$$\alpha \rightarrow \beta. \tag{3.3}$$

The ingoing wave function is a plane wave $\chi_\alpha = e^{i\vec{k_\alpha}.\vec{r}}$ being the solution of the Schrödinger equation:

$$-\frac{\hbar}{2m_\alpha}\Delta\chi_\alpha = E_\alpha\chi_\alpha. \tag{3.4}$$

The outgoing wave function tends asymptotically to a spherical wave $\chi_\beta = f(\theta)\frac{e^{ik_\beta r}}{r}$ where $f(\theta)$ is called the scattering amplitude and depends on the scattered angle. In order to determine the cross section for the reaction we start to calculate the incident flux $\vec{j}_{inc}$ and the outgoing flux $\vec{j}_\Omega$ in the solid angle $d\Omega$. We can see a schematic view of the process in figure 3.2.

By definition of the flux, we have (cf Messiah [51], Chap 4):

$$\vec{j} = \frac{1}{m}Re\Big(\chi^*(\frac{\hbar}{i}\nabla\chi)\Big) = \frac{\hbar}{2im}(\chi^*\nabla\chi - \chi\nabla\chi^*) \tag{3.5}$$

Thus the incident flux can be written as:

$$\vec{j}_{inc} = \frac{\hbar}{m_\alpha}\vec{k}_\alpha \tag{3.6}$$

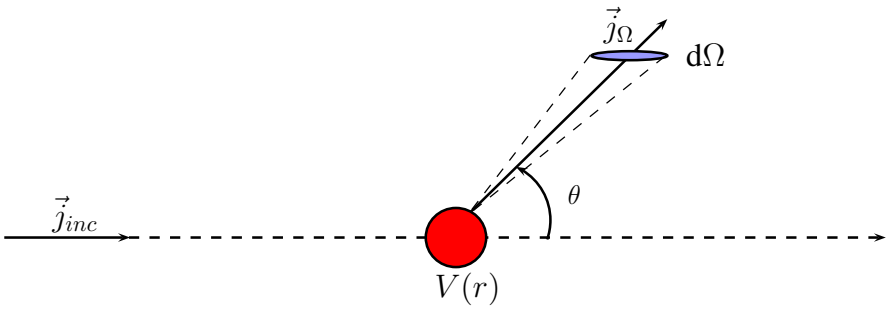

Figure 3.2: *Diffusion by a potential $V(r)$ into the solid angle $d\Omega$*

and the outgoing flux:

$$\vec{j}_\Omega = \frac{\hbar}{m_\beta r^2}\vec{k}_\beta |f(\theta)|^2 \tag{3.7}$$

Then, we can deduce the cross section $d\sigma$ in a surface of area $A = r^2 d\Omega$ as the ratio of the fluxes:

$$d\sigma = \frac{\vec{j}_\Omega}{\vec{j}_{inc}} r^2 d\Omega \tag{3.8}$$

Finally we have

$$\left(\frac{d\sigma}{d\Omega}\right)_{\alpha\beta} = \frac{m_\alpha}{m_\beta}\frac{k_\beta}{k_\alpha}|f(\theta)|^2 \tag{3.9}$$

All the information about the differential cross section is in the function $f(\theta)$. Now we need to know how to calculate it.

Scattering theory

Let us consider the following reaction:

$$A + a \rightarrow B + b. \tag{3.10}$$

The Hamiltonian for the A and a nuclei are H_A and H_a respectively and the corresponding Schrödinger equations are:

$$\begin{cases} (H_a - \epsilon_a)\Phi_a = 0 \\ (H_A - \epsilon_A)\Phi_A = 0. \end{cases} \tag{3.11}$$

The wave function Φ_A is the intrinsic wave function of A and depends on the coordinate of this nucleus and ϵ_A is the eigenvalue. Idem for Φ_a.
We can introduce the relative coordinate r_α for the entrance channel and the corresponding kinetic energy operator by:

$$T_\alpha = -\frac{\hbar}{2m_\alpha}\nabla_\alpha^2, \tag{3.12}$$

where $m_\alpha = \frac{m_a m_A}{m_a + m_A}$ is the reduced mass.
The two nuclei A and a interact with each other during the reaction through the two-body interaction V_{ij}. Thus we can write the entrance potential as follows:

$$V_\alpha = \sum_{i\in a, j\in A} V_{ij}. \tag{3.13}$$

The total Hamiltonian for the entrance and exit channels is:

$$H = H_\alpha + T_\alpha + V_\alpha = H_\beta + T_\beta + V_\beta, \tag{3.14}$$

where $H_\alpha = H_A + H_a$ and $H_\beta = H_B + H_b$ refers only to the intrinsic structure of the nucleus and we note:

$$\begin{cases} \Phi_\alpha = \Phi_A \Phi_a \\ \Phi_\beta = \Phi_B \Phi_b \end{cases} \tag{3.15}$$

Φ_α and Φ_β satisfy

$$(H_\alpha - \epsilon_\alpha)\Phi_\alpha = 0 \tag{3.16}$$

where $\epsilon_\alpha = \epsilon_A + \epsilon_a$.
Now, for the entire system $A + a$ described by the total wave function Ψ_α we have:

$$\begin{cases} (H_\alpha + T_\alpha + V_\alpha)\Psi_\alpha = E\Psi_\alpha \\ (H_\beta + T_\beta + V_\beta)\Psi_\beta = E\Psi_\beta \end{cases} \tag{3.17}$$

Now if we consider that there is no interaction between the two nuclei $A - a$ and $B - b$ these equations become:

$$\begin{cases} (E - H_\alpha - T_\alpha)\phi_\alpha = 0 \\ (E - H_\beta - T_\beta)\phi_\beta = 0 \end{cases} \tag{3.18}$$

where $\phi_\alpha = e^{i\vec{k_\alpha}.\vec{r_\alpha}}\Phi_\alpha$ and $\phi_\beta = e^{i\vec{k_\beta}.\vec{r_\beta}}\Phi_\beta$. Finally $\frac{\hbar^2 k_\alpha^2}{2m_\alpha} = E_\alpha = E - \epsilon_\alpha$ is the kinetic energy of the relative motion in the α channel and $E_\beta = E - \epsilon_\beta$ is the relative kinetic energy in the β channel. Indeed if there is no interaction, we have just a plane wave for the relative motion. ϕ_α is the solution when there is no interaction between the A and a nuclei.
We multiply equation 3.17 by Φ_β which corresponds to the wave function for the $B + b$ system in the output channel and we integrate over the internal coordinate $d\xi$ we have:

$$(E_\beta - T_\beta)(\Phi_\beta, \Psi_\alpha) = (\Phi_\beta, V_\beta \Psi_\alpha), \tag{3.19}$$

where $(\Phi_\beta, \Psi_\alpha)$ corresponds to the integration on the internal coordinates and we note :

$$\psi_\beta(r_\beta) = (\Phi_\beta, \Psi_\alpha) = \int \Phi_\beta^* \Psi_\alpha d\xi. \tag{3.20}$$

we can then rewrite the previous equation as

$$(E_\beta - T_\beta)\psi_\beta = (\Phi_\beta, V_\beta \Psi_\alpha). \tag{3.21}$$

We can resolve this kind of equation through Green's function method and extract the scattering amplitude of such a process:

$$f_{\beta\alpha}(\theta) = -\frac{m_\beta}{2\pi\hbar^2} \int e^{-i\vec{k_\beta}.\vec{r}} (\Phi_\beta, V_\beta \Psi_\alpha^{(+)}) d\vec{r} \tag{3.22}$$

where the angle θ corresponds to the angle between $\vec{k_\beta}$ and $\vec{k_\alpha}$. The $(+)$ sign that appears is used to denote the outgoing wave condition at $r \to \infty$ while a $(-)$ sign would be used to denote an incoming wave. More frequently we use the T-matrix instead of the scattering amplitude which is written as:

$$T_{\beta\alpha} = \langle \phi_\beta | V_\beta | \Psi_\alpha^{(+)} \rangle \,, \tag{3.23}$$

where, I remind here $\phi_\beta = e^{i\vec{k_\beta}.\vec{r_\beta}}\Phi_\beta$. The relation between the scattering amplitude and the T-matrix is:

$$f_{\beta\alpha} = -\frac{m_\beta}{2\pi\hbar^2} T_{\beta\alpha}. \tag{3.24}$$

Now, in order to get the cross section of the reaction we need to calculate this transition matrix between the ingoing channel α and the outgoing channel β :

$$\left(\frac{d\sigma}{d\Omega}\right)_{\beta\alpha} = \frac{m_\alpha m_\beta}{(2\pi\hbar^2)^2}\frac{k_\beta}{k_\alpha}|T_{\beta\alpha}|^2. \tag{3.25}$$

3.2.2 Optical potential

Equation 3.23 gives the transition matrix where Ψ_α is the exact solution and contains the description of everything in the incoming channel. In this part we shall see how to calculate this transition matrix by doing some physical approximations.
We introduce a potential $U_\alpha(r_\alpha)$ that only depends on the relative coordinate between the two nuclei. We choose U_α in order to describe as well as possible the elastic scattering and then the transfer reaction is interpreted as a small perturbation compared to the elastic scattering. If U_α were the whole interaction between the nuclei a and A the Schrödinger equation would become:

$$(H_\alpha + T_\alpha + U_\alpha - E)\Psi_\alpha = 0, \tag{3.26}$$

We can separate this equation in an intrinsic nuclear part contained in H_α with the wave function Φ_α and in a part containing the relative motion where the solution is the wave function χ_α:

$$(T_\alpha + U_\alpha - E_\alpha)\chi_\alpha = 0. \tag{3.27}$$

Then the total wave function is the product of the nuclear wave function with the relative one as: $\Psi_\alpha = \Phi_\alpha\chi_\alpha$.
Since U_α depends only on the relative coordinates it cannot cause any modification in the nuclei and can only describe the elastic scattering. In order to describe the transfer reaction that corresponds to a missing flux in the elastic channel, U_α must be complex and contain an imaginary part. This potential U_α is called the optical potential and is written as:

$$U_\alpha(r) = V_c - Vf(x_0) + \left(\frac{h}{m_\pi c}\right)^2 V_{so}(\sigma.\mathbf{l})\frac{1}{r}\frac{d}{dr}f(x_{so}) - i\left[Wf(x_W) - 4W_D\frac{d}{dx_D}f(x_D)\right], \tag{3.28}$$

where $V_c = ZZ'e^2/r$ if $r > R_c$ and $V_c = (ZZ'e^2/2R_c)(3 - r^2/R_c^2)$ if $r < R_c$, and $f(x_i)$ is a Wood-Saxon function:

$$f(x_i) = \frac{1}{1 + \exp(\frac{r - r_i A^{1/3}}{a_i})}. \tag{3.29}$$

The imaginary part in the potential is negative to describe the missing flux in the elastic channel. It corresponds to the flux in the other channel of reaction (inelastic).
Then by introducing this global potential we can write the T-matrix as follows:

$$T_{\beta\alpha} = \langle e^{i\mathbf{k}'_\alpha \cdot \mathbf{r}_\alpha} | U_\alpha | \chi_\alpha^{(+)} \rangle \, \delta_{\alpha\beta} + \langle \chi_\beta^{(-)} \Phi_\beta | V_\beta - U_\beta | \Psi_\alpha^{(+)} \rangle \,, \tag{3.30}$$

where the first term of equation 3.30 corresponds to the elastic-scattering transition and the second one to the transfer solution.

3.2.3 Born approximation

In order to calculate the second term of equation 3.30 we shall perform the DWBA approximation that is to replace the total wave function Ψ_α by the product of the internal wave function Φ_α with the distorted wave function χ_α that describes the elastic scattering:

$$\Psi_\alpha^{(+)} = \Phi_\alpha \chi_\alpha^{(+)}. \tag{3.31}$$

Then we can write for the transfer part of the transition matrix:

$$T_{\beta\alpha}^{DWBA} = \langle \chi_\beta^{(-)} \Phi_\beta | V_\beta - U_\beta | \Phi_\alpha \chi_\alpha^{(+)} \rangle \,, \tag{3.32}$$

or

$$T_{\beta\alpha} = \int \chi_\beta^{(-)*}(\mathbf{k}_\beta, \mathbf{r}_\beta)(\Phi_B \Phi_b | V_\beta - U_\beta | \Phi_A \Phi_a) \chi_\alpha^{(+)}(\mathbf{k}_\alpha, \mathbf{r}_\alpha) \mathrm{d}\mathbf{r}_\alpha \mathrm{d}\mathbf{r}_\beta. \tag{3.33}$$

3.2.4 Selection rules

For the transfer reaction, the selection rules are:

$$\vec{J_B} = \vec{J_A} + \vec{j} = \vec{J_A} + \vec{L} + 1\vec{/}2, \tag{3.34}$$

with $\vec{L}$ the transferred angular momentum. Concerning the parity conservation, we have the following rule:

$$\pi_B = \pi_A(-1)^L. \tag{3.35}$$

Example : (d,^{3}He) transfer reaction

Let us consider the following reaction where we have proton pick-up:

$$A(= B + p) + d \rightarrow B +^3 He(= d + p).$$

We can write the Hamiltonian of the entrance channel α as:

$$H_\alpha = H_A + H_a + K_{aA} + V_{aA}$$

here $a = d$, so :

$$H_\alpha = H_A + H_d + K_{dA} + V_{dA}.$$

V_{dA} is the interaction between the deuteron and the nucleus A :

$$V_{dA} = \sum_{i \in d, j \in A} V_{ij}.$$

We can decompose the potential into two parts :

- the elastic scattering part U_{dA}
- the inelastic process part W_{dA}:

$$V_{dA} = U_{dA} + W_{dA}.$$

The distorted waves are solutions of the potential describing the elastic scattering:

$$(K_{dA} + U_{dA}) \left|\chi^{(+)}_{dA}\right\rangle = \epsilon_{dA} \left|\chi^{(+)}_{dA}\right\rangle .$$

In the same way we define the distorted wave of the outgoing channel $\beta =^3\mathrm{He}B$: $|\chi^{(-)}_{^3\mathrm{He}B}>$, such as:

$$(K_{^3HeB} + U_{^3HeB}) \left|\chi^{(-)}_{^3HeB}\right\rangle = \epsilon_{^3HeB} \left|\chi^{(-)}_{^3HeB}\right\rangle .$$

The matrix transition for the inelastic process $\alpha \to \beta$ is:

$$T_{\alpha\beta} = \langle \chi^{(-)}_{^3HeB} \Phi_B \Phi_{^3He} | W_{dA} | \chi^{(+)}_{dA} \Phi_A \Phi_d \rangle \tag{3.36}$$

and we can write:

$$W_{Ad} = V_{Ad} - U_{Ad} = V_{pd} + (V_{dB} - U_{Ad}) \approx V_{pd} \tag{3.37}$$

where we assume that V_{dB} and U_{dA} have the same order of magnitude. Then

$$T_{\alpha\beta} = \langle \chi^{(-)}_{^3HeB} \Phi_B \Phi_{^3He} | V_{pd} | \chi^{(+)}_{dA} \Phi_A \Phi_d \rangle \,. \tag{3.38}$$

Moreover, we assume that V_{pd} only depends on the relative distance $d-p$ and the we can write:

$$T_{\alpha\beta} = \int d\mathbf{r}_\alpha d\mathbf{r}_\beta \chi^{(-)*}_\beta(\mathbf{r}_\beta, \mathbf{k}_\beta) \langle \Phi_B | \Phi_A \rangle \langle \Phi_{^3He} | V_{pd} | \Phi_d \rangle \chi^{(+)}_\alpha(\mathbf{r}_\alpha, \mathbf{k}_\alpha). \tag{3.39}$$

We can consider separately the integral

$$\langle \Phi_B | \Phi_A \rangle = \int \Phi^{M_B *}_{J_B}(\xi) \Phi^{M_A}_{J_A}(\xi, r_p) d\xi.$$

In our case $A = B + b$, so in the shell model framework, we can write:

$$\Phi^{M_A}_{J_A} = \sum_{jlmM_B} \beta_{jl} \langle J_B j M_B m | J_A M_A \rangle \Phi^{M_B}_{J_B} \phi^m_{nlj} \tag{3.40}$$

where ϕ^m_{nlj} corresponds to the wave function of the individual proton. One has not to forget the isospin between the ingoing and outgoing channel

$$\langle \Phi_B | \Phi_A \rangle = \sum_{jlmM_B} \beta_{jl} \langle T_A t N_A n | T_B N_B \rangle \langle J_B j M_B m | J_A M_A \rangle \phi^m_{nlj}(\mathbf{r}_p) \tag{3.41}$$

where $n = N_B - N_A$ and the spectroscopic factor is defined as

$$S_{lj} = \beta^2_{jl}. \tag{3.42}$$

The isospin is often included in the spectroscopic factor and correspond to C^2S

$$C^2S = S_{lj} \langle T_A t N_A n | T_B N_B \rangle^2 \tag{3.43}$$

where $t = \frac{1}{2}$ and $n = N_B - N_A$.

3.2.5 Zero range approximation

Even though a finite-range calculation will be performed for the analysis in this work, we used the zero-range approximation in a first step. We have done it especially because previous work employed this approximation to calculate cross sections. In order to compare our results with them we want to do the calculations like them in a coherent way. The zero-range approximation assumes that the transferred particle (here the proton) and the particle a (here the deuteron) are at the same position. In this way the form factor has the following form

$$\langle \Phi_{^3He} | V_{pd} | \Phi_d \rangle = D_0 \delta(\vec{r}_{^3He} - \vec{r}_d), \tag{3.44}$$

reducing the number of integrations to be performed.

3.2.6 The DWBA code

In this work we have used two different programs for the calculation of the single-particle transfer cross section. First of all we have used the DWUCK4 code that enables us to perform zero-range calculation. We have used this code in a first step especially for the ^{69}Cu nucleus to be consistent with previous work where spectroscopic factors were extracted using a zero-range calculation. We performed also finite-range calculation using the DWUCK5 code in a second step for both Copper isotopes. Because we use the same potentials and the same calculation for both isotopes, we are able to compare the evolution of the strength in a consistent way.

Part II

Single-particle states in ^{69}Cu

4

Experimental setup

Contents

The NSI47 experiment was performed in March 2013 at the Orsay tandem using the split-pole spectrometer. The goal was to study the ^{69}Cu nucleus through the ^{70}Zn(d,^{3}He)^{69}Cu one-proton transfer reaction. The tandem facility provides a good quality deuteron beam of 27 MeV (13.5 MeV/A) in order to perform the reaction of interest in direct kinematics. The beam was then sent onto a 95% purified ^{70}Zn target. In this chapter we describe the experimental setup: first we briefly describe the beam production, then the Split-pole and finally the focal place detection system is described.

4.1 Beam production

Tandem accelerator is an electrostatic engine used to accelerate different ions. The charged particles gain energy under a high static field. The high voltage is created by charges in the center of the machine. In this part there is a positive high voltage up to 15 MV (maximum voltage). The acceleration of the desired ions is done in two steps: first the atoms we want to accelerate are transformed into negative ions and injected at one extremity of the tandem where they feel the electrostatic field. In the center of the machine these ions are stripped through a thin layer of carbon becoming positive ions and one more time accelerated because they are repulsed in the second part of their trajectory. In this experiment, a deuteron beam was produced at 27 MeV using a duoplasmatron ion source at an average intensity of 200 nA. The beam was then transported toward a ^{70}Zn target located at the the focal point of an Enge split-pole magnetic spectrometer.

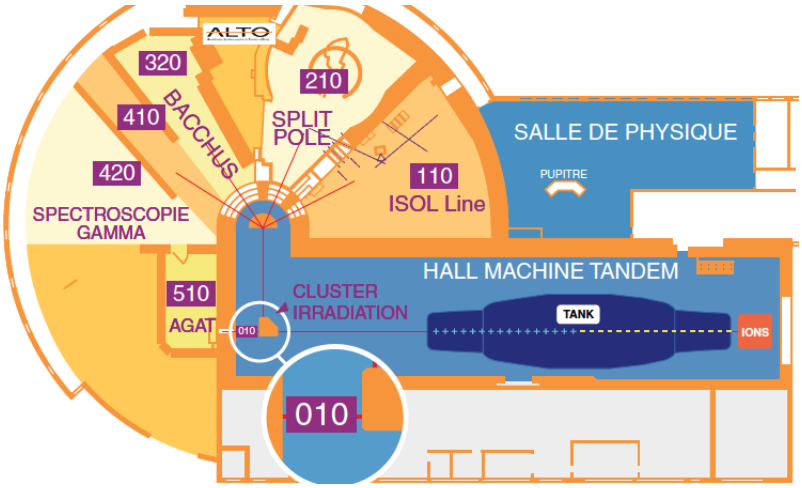

Figure 4.1: *Experimental areas at the ALTO facility, the Split-pole is in the room 210*

4.2 Split-pole spectrometer and detection system

4.2.1 The spectrometer

The recoil light particles of interest are detected with an Enge Split-pole magnetic spectrometer [52]. This spectrometer (figure 4.4) has two separated pole pieces enveloped by a single coil in order to focus the particles over a broad range of energies. Thanks to the split-pole, the particles are momentum analysed once they are focused on the focal plane detection system. One specificity of the spectrometer and this focal plane detection system is the Doppler shift characteristic for the reaction. It has to be taken into account for the final resolution. Indeed, for one energy of a particle corresponds one unique position into the focal plane: this is a dispersive spectrometer. For a two-body reaction the energy of the emitted particle depends on the angle. Because of the acceptance of the split-pole for a given populated state in the residual nucleus, the position of the particles in the focal plane will be broader as it is illustrated in figure 4.3. To understand the displacement δ (figure 4.2) of the focal plane due to this effect, let us define some characteristics of the spectrometer. One of them is the dispersion D defined as follows:

$$D = \frac{\Delta y}{\Delta \rho}. \tag{4.1}$$

For the split-pole we have $D = 1.8$ [52].
The other main characteristic of the spectrometer is the magnification M_H defined as follows:

$$M_H = \frac{\Delta \theta}{\Delta \theta_e}, \tag{4.2}$$

where $\Delta\theta$ is the angle between the central ray and the divergent ray from the same reaction at the entrance and $\Delta\theta_e$ is the same but at the exit. For the split-pole we have $M_H = 0.34$ throughout the range of the spectrometer. As we can see in figure 4.2, the displacement δ for the detector is defined as:

$$\delta \approx \frac{\Delta y}{\Delta \theta_e}. \tag{4.3}$$

By replacing Δy and $\Delta\theta_e$ by the previous equations and considering infinitesimal angles, we have:

$$\delta = D M_H \frac{\Delta \rho}{\Delta \theta} = D M_H \frac{\mathrm{d}\rho}{\mathrm{d}\theta} = \frac{D M_H}{B} \frac{\mathrm{d}(B\rho)}{\mathrm{d}\theta}, \tag{4.4}$$

where B is the constant magnetic field inside the spectrometer. The displacement δ in equation 4.4 is given in meter. The focal plane is situated at 295 mm behind the last magnet. Then, after correction for the displacement, the focal plane detection system is placed at $295 + 1000\delta$ mm behind the last magnet to have the best resolution in excitation energy. The displacement depends of course on the angle, thus a new displacement was set up in order to have the resolution as good as possible for each angle. In other words, the detection system was moved at each angle to optimize de resolution. In table 4.1 we can see the different displacement δ set for the different angles. One can note that the displacement increase with the angle, because the slot of the kinematic line is also bigger with the angle as we can see in figure 4.5.

θ_{lab} (deg)	4	6	9	12	15	18	21	24
δ (mm)	-1.4	-2.1	-2.9	-4.1	-5.1	6.1	-7.0	-8.0

Table 4.1: *List of the different displacement δ for our reaction of interest for each angle in the laboratory frame*

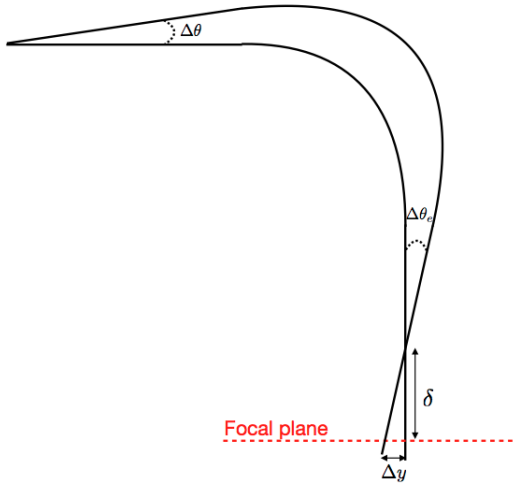

Figure 4.2: *Illustration of the kinematic displacement δ*

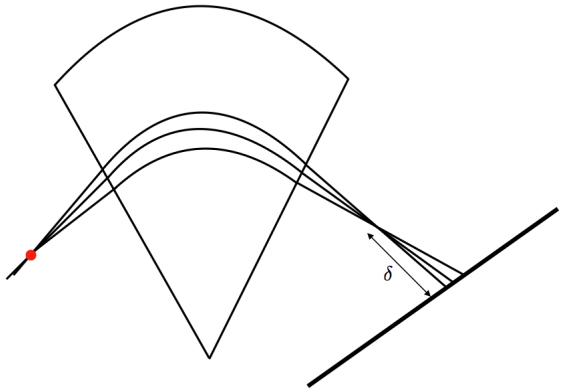

Figure 4.3: *Illustration of the dispersion due to the acceptance of the spectrometer*

For Split-pole, the focal plane detection system is characterized by the minimum rigidity $\rho_{min} = 63$ mm and the maximum one. Because the detection system is at 45 degrees

to the focal plane the maximum rigidity is given by $\rho_{max} = \rho_{min} + L\cos\frac{\pi}{4}$ where L is the active area of the detector. Knowing that the active area of the detection system is 30 cm, we find $\rho_{max} = 84.1$ cm. These two values define the maximum range of excitation energy achievable in one setting of the magnetic field.
One other important characteristic of the spectrometer is its acceptance $\Delta\Omega$. For the split-pole, the nominal acceptance is 1.7 msr but it depends on the opening of the vertical and horizontal slits. For our experiment the opening of the vertical slits was $L_v = 8$ mm and the opening of the horizontal ones was $L_h = 10$ mm, and because the target is at $R = 262.2$ mm from the opening of the spectrometer we have the acceptance:

$$\Delta\Omega = \frac{L_v L_h}{R^2} = 1.16 \text{ msr} \tag{4.5}$$

This has to be taken into account for the normalisation procedure.
Finally, it is important to set the appropirate magnetic field B in order to select the region of excitation energy we are interested in. As we can see in figure 4.5, the $B\rho$ line as a function of the angle is slightly flat between 0 and 25 degrees, then with one setting of the magnetic field we will be able to measure the range from 0 to 7 MeV of excitation energy for ^{69}Cu. To do so we have set the magnetic field at $B_{transfer} = 1.45$ T. Nevertheless, for the elastic scattering, the magnetic rigidity of the scattered deuteron is quite different. Indeed it corresponds to the maximum of kinetic energy, so a bigger magnetic rigidity. In order to detect the elastic deuterons in the focal plane we set the magnetic field at $B_{elastic} = 0.7$ T.

4.2.2 The detection system

The focal plane detection system consists of three detectors. The first one is a 50 cm long high-resolution position-sensitive proportional counter [53]. Nevertheless the active zone is $L = 30$ cm long. This detector (figure 4.6) is composed of an anode made of five wires at a 2 mm spaced apart. The applied electric field is normal to the anode wire plane. Below this plane at 5 mm, there is the cathode plane composed of metallic strips at a 2.54 mm spaced and at 45 degrees to the normal of the anode plane. The signal in the cathode wires is induced by the anode signal when a particle passes through the detector. Finally

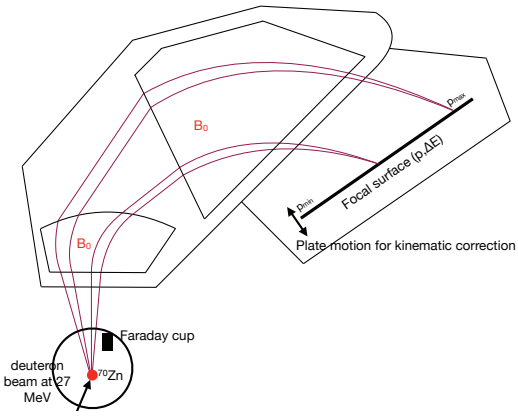

Figure 4.4: *Schematic view of the split-pole spectrometer.*

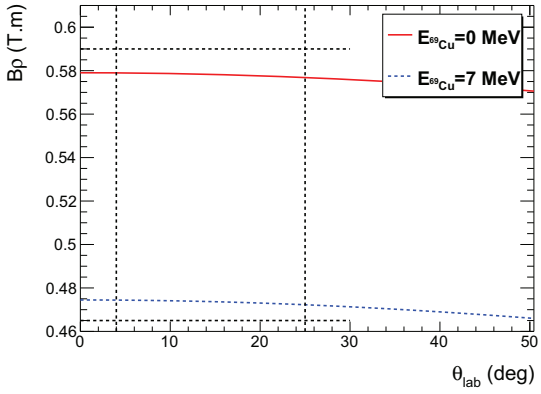

Figure 4.5: *Bρ line as a function of the angle for different excitation energies: red line for the ground state and blue line for 7 MeV excitation energy. The horizontal dotted lines correspond to the acceptance of the spectrometer*

the induced cathode charge is converted into a position signal by connecting each cathode strip to a delay line. The time range of the delay line is 1 μs. That means that we have to be careful with the counting rate of detected particles in the focal plane. The position is given by the time difference between the time corresponding to small $B\rho$ (T_{small}) and the time corresponding to high $B\rho$ (T_{high}). Indeed the time difference of the centroid of the pulse at each extremity of the delay line is proportional to the position of the particle. But in order to have always the same start and stop as it is illustrated in figure 4.7, the T_{small} is delayed with Δt =1 μs as the TAC range is 2 μs. In this way the signal from T_{small} arrives always after T_{high} and the position is given by:

$$\text{Position} = T_{small} + \Delta t - T_{high} \propto \rho, \tag{4.6}$$

where the position is proportional to the magnetic rigidity $B\rho$. The largest position channel corresponds to the maximum range of the TAC that is 2 μs and corresponds to the channel number 32768. The observed resolution in channels for our experiment corresponds to a time resolution of $\sigma = 2$ ns that corresponds to a spatial resolution in the focal plane of $\sigma = 0.21$ mm or $\sigma_{FMHM} = 0.49$ mm.
The second detector is a proportional counter that provides a ΔE signal that corresponds

to the energy loss in the gas. The gas used in the detector is iso-butane at a pressure of 300 mbar. With these two signals combined one can discriminate the different particles in a $B\rho$ versus ΔE spectrum. Finally, behind the position detector, there is plastic scintillator measuring the residual energy. The active area of this plastic is smaller than the position detector reducing the achievable range of excitation energy for the residual nucleus. That is why, no condition on the plastic will be applied in order to have a zone as broad as possible.

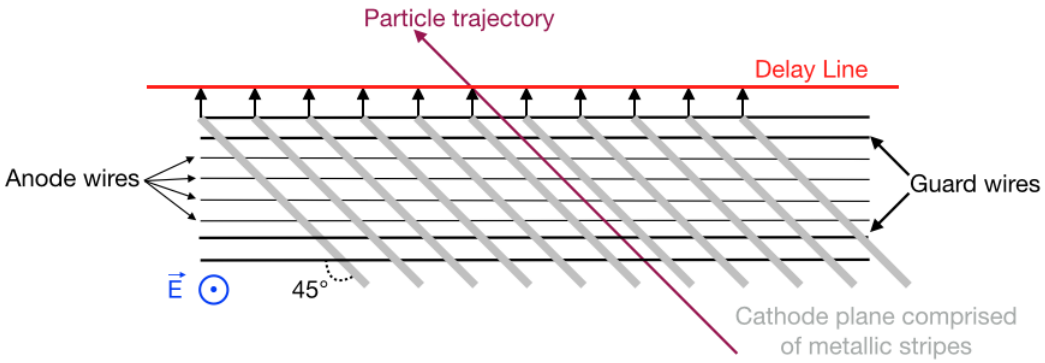

Figure 4.6: *Schematic view of the position-sensitive counter.*

The Faraday cup

The last essential device needed for the normalisation is the Faraday cup place after the reaction chamber. This Faraday cup with 10^{-10} Coulomb per pulse is crucial for counting the number of incident ions. Then if we measure N_F pulses, we can determine the total number of incident particles in the following way:

$$N_{beam} = \frac{N_F}{Q}\frac{10^{-10}}{e} \tag{4.7}$$

where Q, is the charge of the ion beam and e is the elementary charge. In our case we have a deuteron beam, so $Q = Z = 1$. The number of particles N_{beam} will be used for the normalisation procedure to get the differential cross section at each angle.

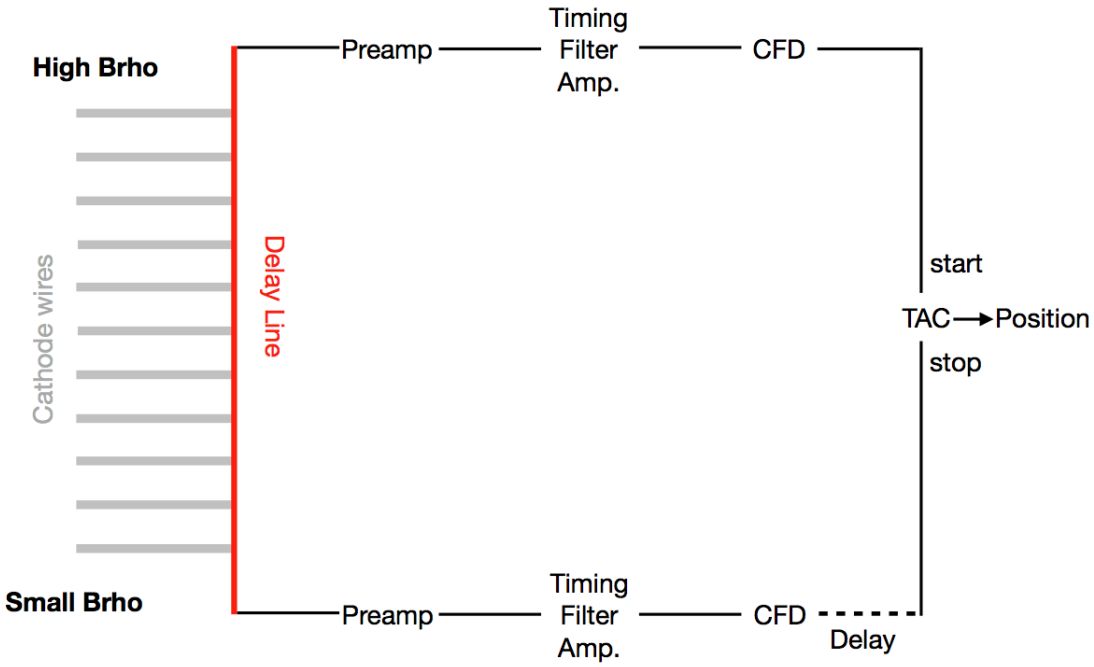

Figure 4.7: *Principle of the delay line to get the position of interaction into the focal plane*

5
Data analysis

Contents

We shall discuss here the different steps of the analysis in order to obtain the information about the populated states in ^{69}Cu. We will first discuss the calibration of the focal plane detector as well as the particle identification. We then discuss the observables

of interest, which are the excitation energy and the angular distributions that contain the nuclear structure information.

5.1 The ^{70}Zn target: contamination and thickness

The target used for the experiment was a 95% ^{70}Zn enriched target (see Appendix A for composition details) deposited on a backing of carbon. Since Zinc oxidizes rapidly a lot of precautions to prevent the target to see oxygen. Nevertheless we clearly see contaminant peaks due to reactions with oxygen. One way to clearly see the different contaminants is to look at the elastic scattering at an angle not too small. In fact by measuring the magnetic rigidity at different angles for the elastic scattering, we can see the kinematic line for each reaction that corresponds to to the elastic channel for each element present in the target. The different kinematic lines are plotted in figure 5.1. The dots correspond to the measured points while the lines correspond to kinematics calculation. We clearly see four different kinematic lines that correspond to Zinc, Carbon, Oxygen and also Silicon. The presence of the three first elements is explained above. But, although we see the presence of silicon in the target, its origin is not very clear.

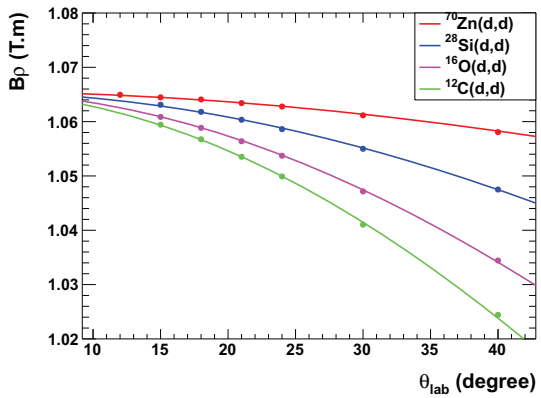

Figure 5.1: *The different kinematic lines corresponding to the different contaminants of the target. Points correspond to the measured $B\rho$ while lines correspond to relativistic kinematic calculation*

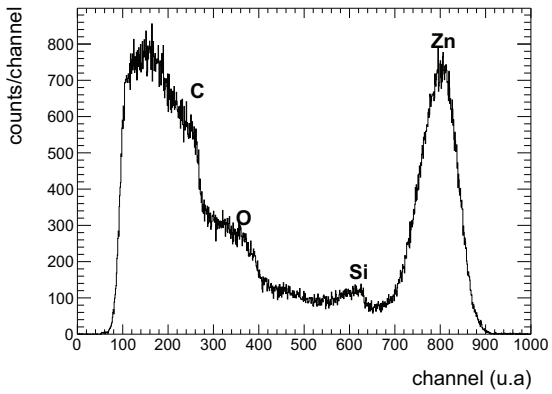

Figure 5.2: *Energy (a.u) of backscattered α particle used to determine the different elements and quantify the number of ^{70}Zn nuclei in the target*

5.1.1 Rutherford backscattering

The quantity of ^{70}Zn is very important to know for the normalisation in order to get the spectroscopic factors. To quantify it, a Rutherford backscattering has been performed at the CSNSM with the help of E. Oliviero and C. Bachelet. Rutherford backscattering (RBS) is a very useful method to see the different elements that compose a material and quantify each element inside the material. For our target, this RBS method was performed using an ^{4}He beam of $E_0 = 1.4$ MeV and the backscattered α particles were detected with a silicon detector placed at 165 degrees in the laboratory frame. The solid angle of the detector is $\Delta\Omega = 3.9$ msr. The relation between backscattered particles of energy E_1 and the incident energy E_0 is:

$$E_1 = \frac{M_1^2}{(M_1+M_2)^2}\Big[\cos\theta + \Big(\Big(\frac{M_2}{M_1}\Big)^2 - \sin^2\theta\Big)^{1/2}\Big]^2 E_0, \tag{5.1}$$

where M_2 is the mass of the target nucleus at rest and M_1 the mass of an α particle. So at a given angle θ the backscattered energy E_1 is well defined for each element. By measuring E_1 we can determine the composition of the target. An example of spectrum for our target is given in figure 5.2. The first peak on the right corresponds to the Zinc part, which is mainly at the surface of the target. But we can also distinguish the presence of silicon and oxygen that correspond to the different bumps in the spectrum and the final bump corresponds to the backing of carbon. In order to well quantify the quantity of Zinc it is necessary to reproduce the profile of the spectrum with the help of the program SIMNRA. After doing so the determined thickness of Zinc is $e = 18.7 \pm 0.9$ μg/cm^2. Since we have a 95% enriched target of ^{70}Zn with a main contaminant of ^{68}Zn for the other 5%, the total atoms of ^{70}Zn is N_{target}[1] $= 1.535 \pm 0.077$ 10^{17} cm^{-2}. We will use this value for the normalisation procedure. The typical error for this kind of measurement is about 5 %. The expected value was $e = 70.0$ μg/cm^2, one can see that we had 3.7 times less of Zinc than expected.

[1] $N_{target} = 0.954\frac{\mathcal{N}_A e}{0.954\times 70+0.046\times 68}$

5.2 Calibration

The main information given by the spectrometer is the particle identification and the position of the detected particle. But in order to know the magnetic rigidity of the particle and thus its energy and finally reconstruct the excitation-energy spectrum of the residual nucleus, we need to calibrate the detector and convert the position into magnetic rigidity $B\rho$.
The calibration is performed using a first-order fit in the following way:

$$B\rho = (a\text{Pos} + b)B, \tag{5.2}$$

where Pos is the position in channel at the focal plane detection system. For this calibration, we have used different peaks corresponding essentially to the elastic channel. Because of the target contamination, we were able to use four peaks of the elastic scattering using the Zinc and the different contaminants at 40 degrees (Si, O and C). We have also used a fifth point that corresponds to the reaction ^{12}C(d,^{3}He)^{11}Be producing ^{11}Be in its ground state at 21 degrees. The different values of the measured positions and the calculated $B\rho$ are listed in table 5.1.

Reaction	Position (u.a)	$B\rho$ (T.m)
^{70}Zn(d,d)	16507.7±3.2	1.05807
^{28}Si(d,d)	15477.8±3.3	1.04750
^{16}O(d,d)	14179.2±4.6	1.03443
^{12}C(d,d)	13198.8±6.1	1.02443
^{12}C(d,^{3}He)^{11}Be	9980.3±5.2	0.49899

Table 5.1: *Measured positions (Pos) and corresponding magnetic rigidity*

We can see the result of the fit in the figure 5.3. Then event by event, in order to get the final magnetic rigidity $B\rho$, we multiply the calibration by the magnetic field B, which was monitored during the experiment. Thus, we can gain in resolution because of the possible fluctuations of the magnetic field that degrade the resolution. Knowing at each time the value of the field enables us to correct for this effect.
After calibration, the resolution in excitation energy is σ = 18 keV in average for the

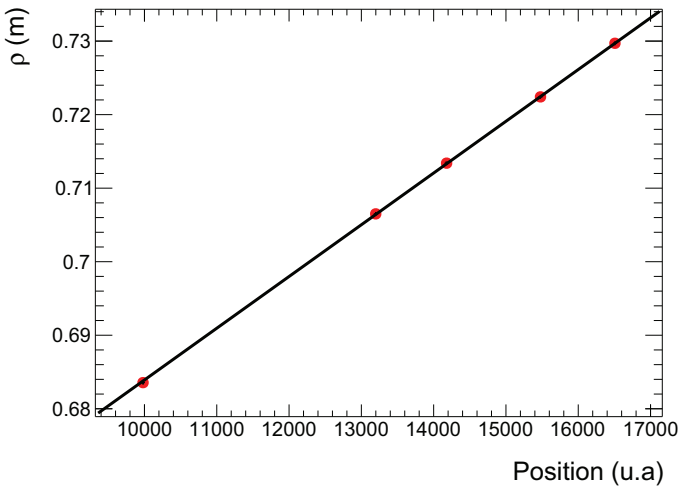

Figure 5.3: *Result of the first order calibration of the curvature ρ as a function of the measured position*

Copper's peaks or $\sigma_{FWHM} = 42.3$ keV. Or in an equivalent way, for a kinetic energy of 20.6 MeV we have $E/\Delta E = 461$. This is a typical value of the split-pole spectrometer and this resolution is enough for us to well resolve each populated peak.

5.3 Particle identification

In order to identify the different particles detected in the split-pole spectrometer we use a $B\rho - \Delta E$ spectrum. We can see such a spectrum in figure 5.4. First I would like to explain the difference between this $B\rho - \Delta E$ spectrum with a more classical $E - \Delta E$ one. With the Bethe-Block formula, we have the following relation:

$$\Delta E \approx AZ^2 \frac{\ln(E)}{E} \tag{5.3}$$

with $E = \frac{1}{2}Av^2$ is the classical kinetic energy of the detected particle. Moreover, we have:

$$A\frac{v^2}{\rho} = ZvB \tag{5.4}$$

Then $v = \frac{Z}{A}(B\rho)$ and $E = \frac{Z^2}{2A}(B\rho)^2$. By replacing it in the equation 5.3, we have :

$$\Delta E \approx \frac{2A^2}{(B\rho)^2} \ln\left(\frac{Z^2(B\rho)^2}{2A}\right) = \frac{2A^2}{(B\rho)^2}\Big(2\ln(Z) + 2\ln(B\rho) - \ln(2A)\Big) \tag{5.5}$$

One can see that ΔE versus $B\rho$ correlation does not depend on Z^2 but on $\ln(Z)$. That is why the separation in Z for a given mass A is not so good compare to a $E - \Delta E$ plot. Neverthless the separation in mass A is much better. That is why the contour used in figure 5.4 includes the tritons. Nevertheless, because of very different kinematics between the (d,t) and (d,^{3}He) transfer reactions the resolutions are different. Indeed the kinematic shifts δ are not the same between those two reactions and then we can see that the tritons are not at all horizontal and rather large because the focal plane was set for the (d,^{3}He) reaction. Then it will be easy to separate their contributions in the final spectrum.

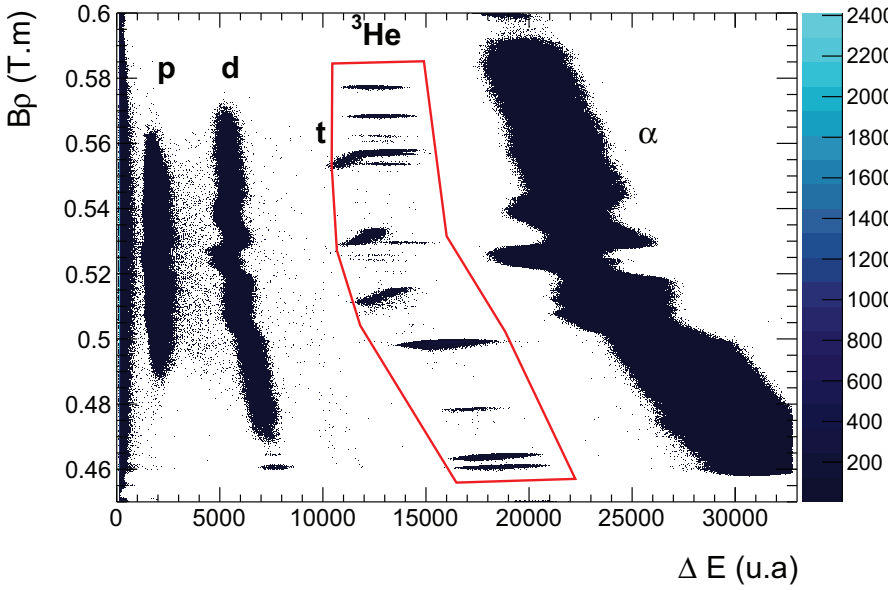

Figure 5.4: *Particle identification in the spectrum $B\rho$ versus the energy loss ΔE*

5.3.1 Reaction with contaminant

As one can see in figure 5.4, it is not possible to clearly separate the triton form the ^{3}He. In addition of the (d,^{3}He) transfert reaction, we select also the (d,t) reaction channel. In figure 5.5, one can see the position in the focal plane detection system of the expected states in the different reaction channels. One can notice that all channels give discrete states except for the ^{70}Zn(d,t)^{69}Zn where we are situated in the continuum for this reaction. It is then most probable that the possible background in our final spectrum comes from this continuum.

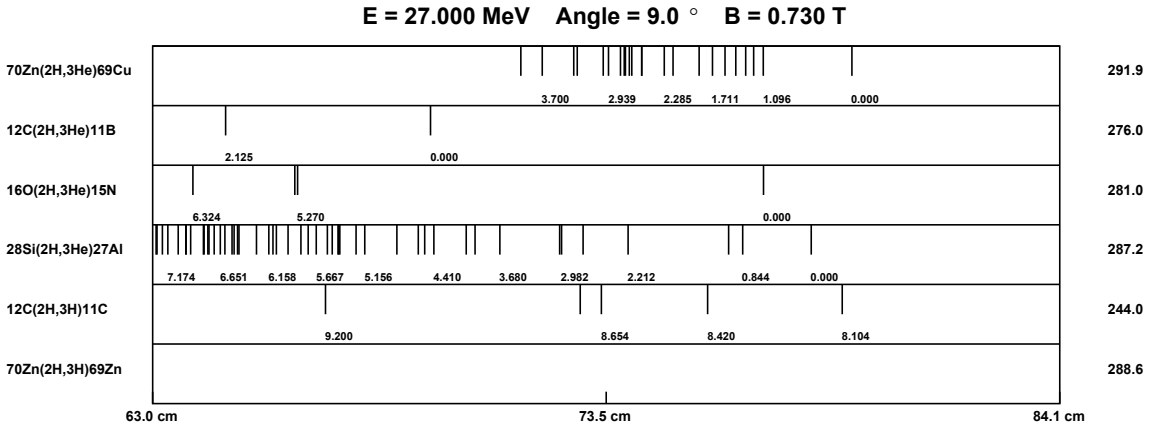

Figure 5.5: *Expected position in the focal plane detection system for the different channel of reaction. The numbers on the right correspond to the position of the focal plane detection system (in mm) for a given reaction to achieve the best resolution*

5.4 Observables of interest

Direct reactions are a great tool for the nuclear structure and in particular here the transfer reaction. Thanks to the two-body kinematics, by detecting the light fragment, we can have access to the information about the residual nucleus by the missing mass method. Considering this two-body reaction:

$$A + a \rightarrow B + b, \tag{5.6}$$

where A is the beam and a the target (a is at rest in the laboratory frame). By detecting the particle b, meaning measuring its energy and its angle θ_{lab} in the laboratory frame, one can reconstruct the angular distribution and the excitation energy of B.

5.4.1 Magnetic rigidity and excitation energy

We can define the energy-momentum four-vector for each nucleus (here we use $c = 1$):

$$P_A = \begin{pmatrix} T_A + m_A \\ \vec{p_A} \end{pmatrix},\ P_a = \begin{pmatrix} m_a \\ 0 \end{pmatrix},\ P_b = \begin{pmatrix} E_b \\ \vec{p_b} \end{pmatrix} \text{ et } P_B = \begin{pmatrix} E_B \\ \vec{p_B} \end{pmatrix}$$

We want to construct the excitation energy of B knowing that we measure the kinetic energy $T_b = E_b - m_b$ and its angle θ_b. We know that:

$$\begin{cases} p_A = \sqrt{T_A^2 + 2m_A T_A} \\ p_a = 0 \\ p_b = \sqrt{T_b^2 + 2m_b T_b} \end{cases} \tag{5.7}$$

because $E^2 = p^2 + m^2$ and $E = T + m$.
The conservation of the impulsion gives $(\vec{p_A} + \vec{p_a})^2 = (\vec{p_b} + \vec{p_B})^2$, so:

$$p_B = \sqrt{p_A^2 + p_b^2 - 2p_A p_b \cos\theta_b}. \tag{5.8}$$

Moreover with the energy conservation we have:

$$E_B = T_A + m_A + m_a - (T_b + m_b). \tag{5.9}$$

Then we can define the excitation energy E_{Bex} of nucleus B as follows:

$$E_{Bex} = m_B - m_{Bgs}, \tag{5.10}$$

where m_{Bgs} is the mass of B in its ground state and m_B is the mass formed in the reaction: $m_B = \sqrt{E_B^2 - p_B^2}$.
Therefore, knowing the beam energy, and measuring the kinetic energy T_b of particle b

together with its angle θ_b, one can calculate the excitation energy E_{Bex} of the nucleus B. Nevertheless here with the split-pole we measure the magnetic rigidity $B\rho_B$. So in order to get the kinetic energy E_B to calculate the excitation energy spectrum we have to use the following relation:

$$B\rho = \frac{\sqrt{T^2 + 2mT}}{cZe}(10^6 e) \tag{5.11}$$

where c is the speed of light and Z the nucleus charge. $(10^6 e)$ term is used to get the magnetic rigidity in T.m when the kinetic energy of the nucleus and its mass are expressed in MeV. By inverting this equation we can get the kinetic energy knowing the magnetic rigidity.

5.4.2 Angular distribution

At a given angle for a populated state in the residual nucleus, we have to normalise the integral of the peak N_{peak} with respect to the beam intensity integrated over the run duration N_{beam}, the number of target nuclei N_{target} in cm^{-2}, and the acceptance of the split-pole $\Delta\Omega$. Thus the normalized cross section is obtained in the following way:

$$\frac{\mathrm{d}\sigma}{\mathrm{d}\Omega} = J(\theta_{CM})\frac{N_{peak}}{N_{beam}N_{target}\Delta\Omega}, \tag{5.12}$$

where $J(\theta_{CM})$ is the Jacobian of the reaction defined as $J(\theta_{CM}) = |\frac{\mathrm{d}\Omega}{\mathrm{d}\Omega_{CM}}|$ and corresponds to the dilatation between the center-of-mass frame and the laboratory frame. Because we are here in direct kinematics, the Jacobian is close to one. Its typical value is 0.924 at 15 degrees in the laboratory frame for a state at 1.71 MeV.
At each angle, for each populated state in ^{69}Cu we normalise the cross-section in order to obtain the angular distribution, the transferred angular momentum L and its associated spectroscopic factor C^2S. The main error is given by the statistical error on the number of counts N_{peak} in the populated peak and is equal to $1/\sqrt{N_{peak}}$. On top of that an error on the determination of N_{peak} is possible because of the subtraction of the background and it is taken into account for the total error.
To obtain large enough angular distributions in order to discriminate between the shape of different transferred angular momenta, we have measured at 4, 6, 9, 12, 15, 18, 21 and 24 degrees for the transfer reaction plus at 30 and 40 degrees for the elastic channel.
The main difficulty we have encountered is the background subtraction in order to well

establish the number of counts in the populated peak. The procedure was to fit over a range in excitation energy large enough to well fit the background, our peak of interest plus if necessary other peaks if they are situated in the range of the fit. Each peak was fitted with a Gaussian shape and the background with a polynomial of order one. We can see in figure 5.6 a typical fit performed for the state at 1.71 MeV at 9 degrees in the laboratory frame. This fit consists in four gaussians plus a linear background. In figure 5.7 all the background plus the contaminant peaks were subtracted in order to get only the peak of interest and obtain its integral. This method is very efficient for the subtraction and enables us to well establish the number of counts in the peak. This method was applied for all the peaks of interest.

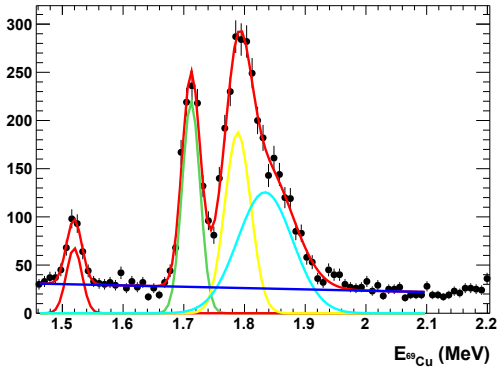

Figure 5.6: *Fit at 9 degrees in the laboratory with multiple Gaussian peaks plus a linear background for the state at 1.71 MeV*

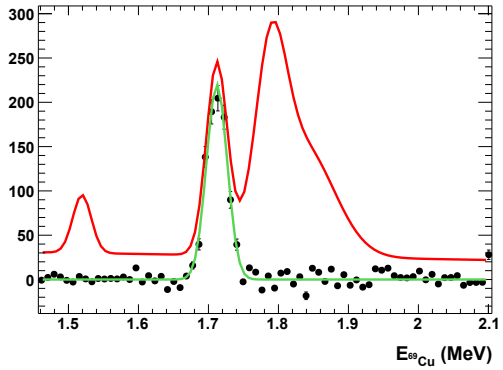

Figure 5.7: *Subtraction of the background plus the contaminant peaks leaving the peak of interest to determine its integral*

6
Results

Contents

THIS chapter will present the results for the ^{70}Zn(d,d) elastic reaction and for the ^{70}Zn(d,^{3}He)^{69}Cu one-proton transfer reaction. In order to extract the transferred angular momentum and the spectroscopic factor, one need to to use a reaction model. For that purpose we will use the standard Distorted Wave Born Approximation (DWBA) model as already explained.

6.1 Elastic scattering

In order to constrain the deuteron entrance channel optical potential used in the DWBA calculations, we have measured the elastic scattering ^{70}Zn(d,d)^{70}Zn. To get the normalized cross section, we have determined for each angle the integral of the elastic peak as we can see in figure 6.1. The peaks we can see at higher energy correspond to the elastic channel on the contaminants present in the target. The result of the angular distribution is shown in figure 6.2. We can see a good agreement between the calculation and the measured cross section giving confidence in the normalisation procedure and in the optical potential used in the entrance channel. No minimization was done to calculate the cross section, only the parametrization was applied in our case. The optical potential used in the entrance channel is the relativistic Daenick potential [54] covering (d,d) reactions from 12 to 90 MeV. This potential was obtained from data on $27 \leq A \leq 238$. The parameters used both for the in-going and out-going channels are listed in the table 6.1. For the out-going channel as we will see in the next section, the Perey and Perey parametrization [55] was used. This is the best available potential for (^{3}He,^{3}He) in our case and it was obtained for $A > 40$ and $E < 40$ MeV.

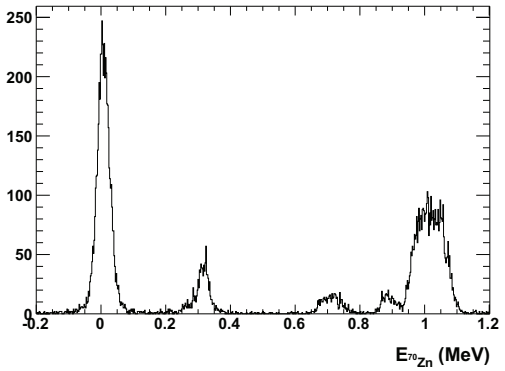

Figure 6.1: *Excitation energy spectrum of ^{70}Zn at $\theta_{lab} = 40^o$, the peaks at higher excitation energy correspond to elastic scattering on the contaminants in the target*

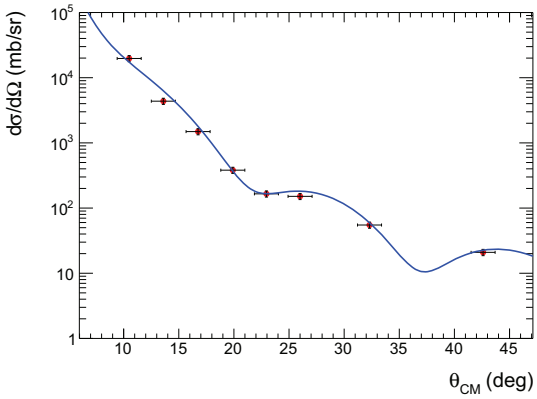

Figure 6.2: *The ^{70}Zn(d,d) elastic cross-section after normalisation (red dot), compared to calculation using relativistic Daenick optical potential*

	V	W	W_D	r_c	r_0	a_0	r_i	a_i	V_{so}	λ
d	86.76	0.90	12.12	1.30	1.17	0.75	1.32	0.81	6.34	
^{3}He	156.5	42.2	0	1.30	1.20	0.72	1.40	0.88	2.50	
p	adj			1.25	1.25	0.65				25

Table 6.1: *Optical potential for ^{69}Cu*

6.2 The transfer reaction

6.2.1 Magnetic rigidity and excitation energy

Once we have measured at a given angle the magnetic rigidity of the particles into the focal plane, we can select the ^{3}He as we saw the figure 5.4 and reconstruct the excitation energy spectrum for the reaction of interest. We can see in figure 6.3 the correspondance between the measured magnetic rigidity and the excitation energy spectrum for the ^{70}Zn(d,^{3}He)^{69}Cu at 21 degrees in the laboratory frame. Of course in these spectra there are some peaks which correspond to reactions on the different contaminants of the target. I remind here that it is not possible to clearly separate the ^{3}He from the triton. But in the sets of magnetic field for our experiment, only the tritons from ^{12}C(d,t)^{11}B were detected into the focal plane and correspond to the broader peaks due to the very different kinematics between this reaction and our reaction of interest as explained above. Because of this we can easily identify the contribution of the (d,t) reaction in our spectra. However there is still ^{3}He coming from other reactions in this region of interest as we saw in figure 5.5. Indeed, if the ^{3}He has the correct kinematics, for each angle its position on the excitation-energy spectrum should not change. If we see a shift in position with the angle, it means that this ^{3}He comes from another reaction and thus does not match with a state in ^{69}Cu. This fact is illustrated in figure 6.4. Two dotted lines of the same color correspond to the same state of a contaminant nucleus. We see clearly that the shift depends on the nucleus and thus on the reaction. The more the kinematics are different the bigger is the energy shift between two angles for a contaminant peak. In this way it is easy to detect the states we have populated in ^{69}Cu during the experiment. Thereby, we have seen eight populated states in ^{69}Cu between the all range accessible within our

settings. In order to get the information about nuclear structure we shall compute angular distributions for all these peaks. In this way, we will get the transferred angular momentum thanks to the shape of the angular distribution.

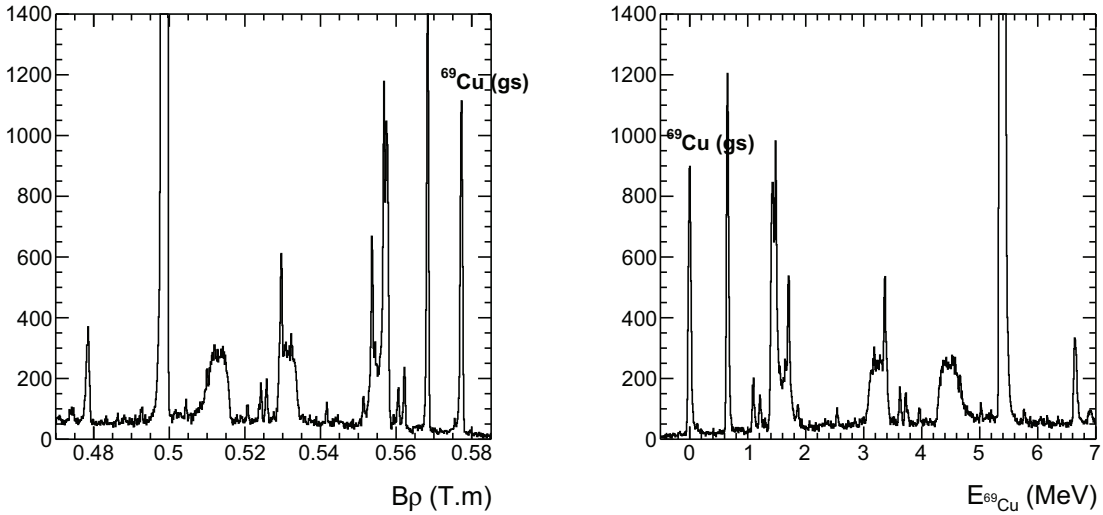

Figure 6.3: *Measured magnetic rigidity $B\rho$ and the associated excitation energy spectrum for the $^{70}Zn(d,^{3}He)^{69}Cu$ at $\theta_{lab} = 21$ degrees*

6.2.2 Angular distributions

We can now do the same work for the populated states in ^{69}Cu as we have performed for the elastic channel. We construct the angular distribution for each state with the same normalisation procedure and then extract the spectroscopic factor C^2S by comparing the result with the one-proton pick-up cross-section calculated with a DWBA code. In a first step, in order to compare our results with the ones of Zeidman [32], we have performed a zero-range (ZR) calculation using the DWUCK4 code. We used the same parameters of the Wood-Saxon potential for the transferred proton as Zeidman: $r_0 = 1.20$ fm and $a_0 = 0.70$ fm. We have also performed calculation using $r_0 = 1.25$ fm and $a_0 = 0.65$ fm as they are listed in the table 6.1 in order to be consistent with most of the literature. The other parameters are not the same as Zeidman's due to the beam energy dependance of

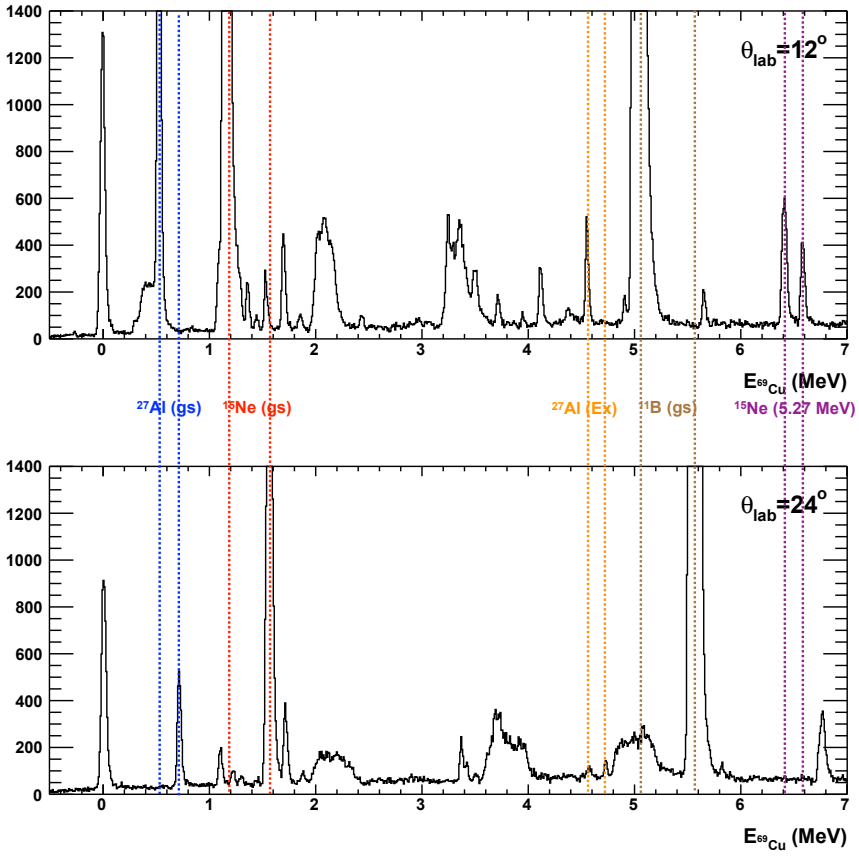

Figure 6.4: *Excitation energy spectrum of ^{69}Cu at θ_{lab} = 12 and 24 degrees illustrating the energy shift for the contaminant peaks. Two dotted lines of the same color correspond to the same state of a contaminant nucleus*

the parameters. In a second step we have performed a finite-range (FR) calculation using the DWUCK5 code. In the case of the finite-range calculation, we have used the Brida *et al.* potential [56] for the form factor to describe the overlap between the deuteron and ^{3}He. It consists of a parametrization using a Wood-Saxon plus a Gaussian potential. Finally we have to take into account for the normalisation procedure that the spectroscopic overlap between the deuteron and the ^{3}He is $<^2$ H$|^3$He $>= 1.33$.
We can see in figures 6.5, 6.6, 6.7, 6.8, 6.9, 6.10, 6.11 and 6.12 the angular distributions of the different populated states in the ^{69}Cu. Our results are compared in table 6.2 with the

ones of Zeidman [32]. Our final results using $r_0 = 1.25$ fm and $a_0 = 0.65$ fm and finite-range calculations are listed in table 6.3. The error associated with the spectroscopic factor is about 0.1 to 0.2. Moreover the difference between the two values of radius and diffuseness for the transferred proton used in the calculation gives a difference for the spectroscopic factor of 10 to 15%. Finally, the error associated with the position of the peaks is 0.01 MeV.

First of all, we see that we are in agreement with the populated states in common for the assigned spin and parity J^π. It was not possible in this experiment to assign the state at 1.10 MeV due to the presence of contaminant peaks in this energy range at low angles. We are also in agreement for the spectroscopic factors except for the $5/2^-$ state at 1.23 MeV. Indeed we have measured a spectroscopic factor twice smaller than Zeidman *et al.*. Moreover, we see that we were able to determine the angular distributions of three more states with their spectroscopic factors. Particularly we have measured a new $L = 3$ state at 3.35 MeV that corresponds to 30 % of the strength for a $f_{7/2}^{-1}$ proton-hole state. The two other states at 3.70 MeV and 3.94 MeV correspond to a $L = 2$ and $L = 0$ state respectively. These two states must correspond to a part of the inner *sd* shell of the nucleus.

In order to quantify the measured strength, it is interesting to look at the sum of the spectroscopic factors of the $7/2^-$ populated state. For the zero-range calculation the sum is $\sum C^2S_{7/2^-} = 4$ or 50% of the strength and for the finite-range calculation we have $\sum C^2S_{7/2^-} = 5.4$ or 67% of the $f_{7/2}$ proton-hole state. First we see that there is quite a difference between a zero-range and a finite-range calculation for the determination of the spectroscopic factors, we have a difference of 17%. In both cases, one can wonder where is the missing strength. A part of the answer might be in the energy of the beam that is not enough to populate $L = 3$ states at higher excitation energy. It can be pointed out that the energy of the beam was 27 MeV or 13.5 AMeV. Indeed, as we can see in figure 6.15, the cross section decreases with the excitation energy. Thereby, we want to give a limit of measurable spectroscopic factor as a function of the excitation energy.

[32]			This work		
E (MeV)	J^π	C^2S	E (MeV)	L (J^π)	C^2S (ZR)
0	$3/2^-$	1.3	0	1 ($3/2^-$)	1.60(11)
1.11	$1/2^-$	0.46	1.10	-	-
1.23	$5/2^-$	1.5	1.23	3 ($5/2^-$)	0.90(13)
1.74	$7/2^-$	2.7	1.71	3 ($7/2^-$)	2.70(10)
1.87	$7/2^-$	0.45	1.87	3 ($7/2^-$)	0.55(12)
3.30	-	-	3.35	3 ($7/2^-$)	2.00(8)
3.70	-	-	3.70	2 ($3/2^+$)	2.60(21)
3.95	-	-	3.94	0 ($1/2^+$)	0.80(6)

Table 6.2: *Summary of transferred angular momentum L, spin-parity (J^π) and the associated spectroscopic factor C^2S for the populated states in ^{69}Cu using the zero-range calculation DWUCK4 and as reference [32] $r_0 = 1.20$ fm and $a_0 = 0.70$ fm*

E (MeV)	L (J^π)	C^2S (ZR)	C^2S (FR)	χ^2/NDF
0	1 ($3/2^-$)	1.40(15)	1.50(17)	0.69/6
1.10	-	-	-	-
1.23	3 ($5/2^-$)	0.80(11)	0.70(10)	1.53/2
1.71	3 ($7/2^-$)	2.00(11)	2.50(14)	14.27/5
1.87	3 ($7/2^-$)	0.40(10)	0.50(10)	8.76/3
3.35	3 ($7/2^-$)	1.60(10)	2.40(15)	2.23/4
3.70	2 ($3/2^+$)	1.90(25)	1.50(20)	2.39/5
3.94	0 ($1/2^+$)	0.70(06)	0.70(10)	9.37/4

Table 6.3: *Summary of transferred angular momentum L, spin-parity J^π and the associated spectroscopic factor C^2S for the populated states in ^{69}Cu. We compare zero-range and finite-range calculation using $r_0 = 1.25$ fm and $a_0 = 0.65$ fm*

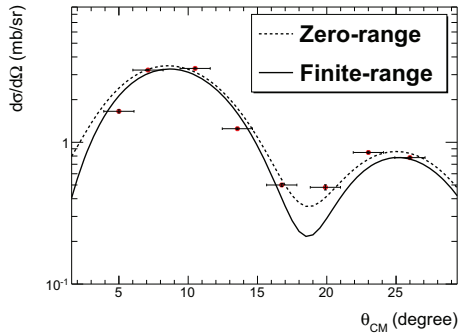

Figure 6.5: *Differential cross-section compared to the DWBA calculation for the ground state*

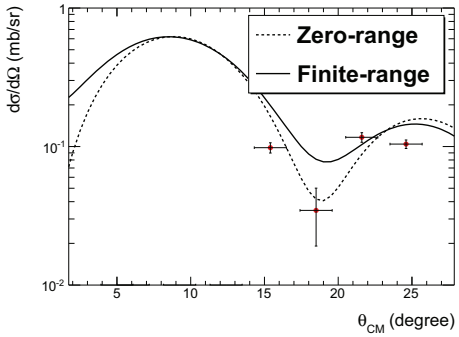

Figure 6.6: *Differential cross-section compared to the DWBA calculation for the state at 1.11 MeV*

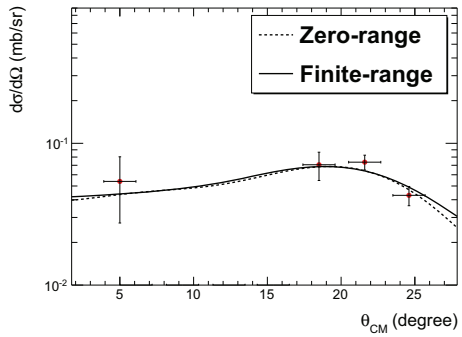

Figure 6.7: *Differential cross-section compared to the DWBA calculation for the state at 1.23 MeV*

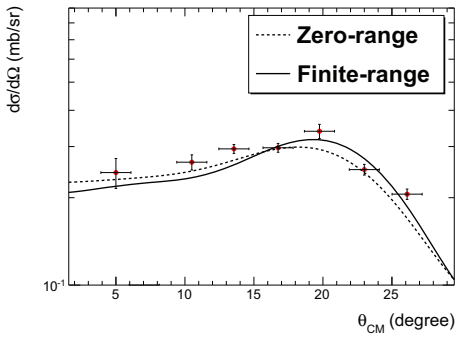

Figure 6.8: *Differential cross-section compared to the DWBA calculation for the state at 1.71 MeV*

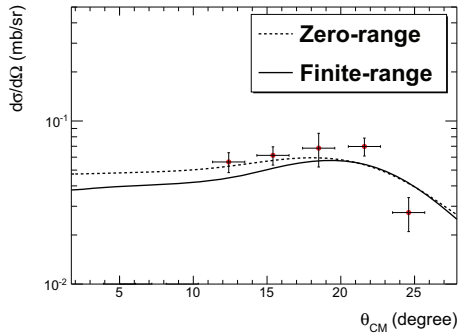

Figure 6.9: *Differential cross-section compared to the DWBA calculation for the state at 1.87 MeV*

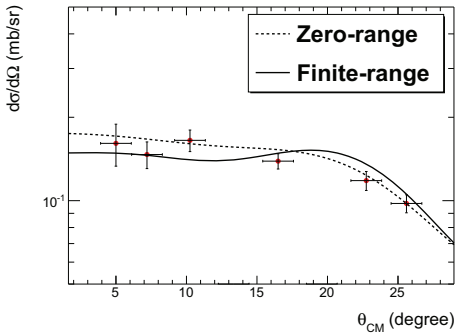

Figure 6.10: *Differential cross-section compared to the DWBA calculation for the state at 3.35 MeV*

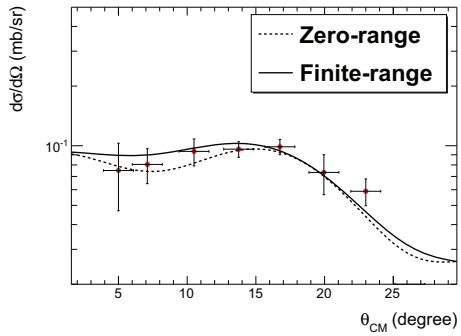

Figure 6.11: *Differential cross-section compared to the DWBA calculation for the state at 3.70 MeV*

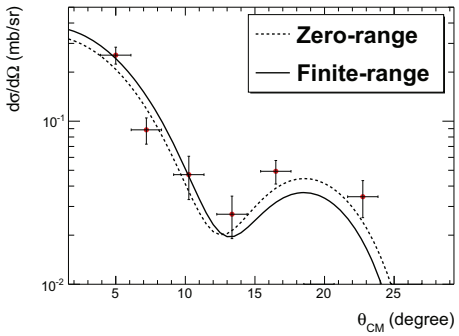

Figure 6.12: *Differential cross-section compared to the DWBA calculation for the state at 3.94 MeV*

6.3 Detection limit

As we can see in figure 6.15 the cross section drops with the excitation energy. We can wonder about the detection limit of our experimental setup. First of all we need to know the number of counts in a peak to detect it. To do so, we have simulated a realistic flat background with an additional peak corresponding to a Gaussian peak with a resolution that corresponds to the experimental one (σ = 18 keV). To determine the number of counts needed to detect a peak, we have simulated different numbers of events

in the Gaussian peak and with the goodness-of-fit test we have determined that we need 130 counts in this peak to detect it with a confidence level of 95%. To do this, we have simulated 10000 times a flat background plus a x counts Gaussian peak. At each iteration it was fitted by a linear fit and then the χ^2 distribution of the fit was plotted. Indeed as we can see in figure 6.14, the centroid of the χ^2 distribution divided by the number of degree of freedom (NDF = 198 here) is $\mu = 1.14$. If a peak would have been populated with 130 counts or more, it would have been identified with a probability larger than 95% in our experiment.

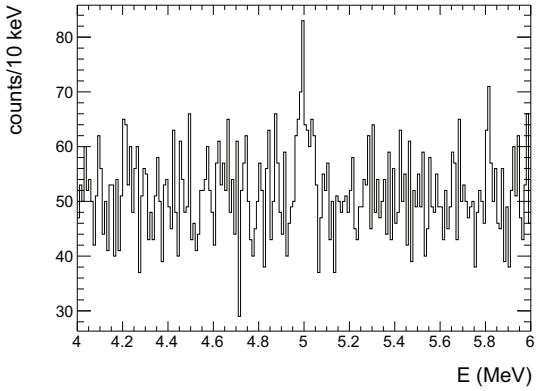

Figure 6.13: *Simulated flat background plus a 130 counts gaussian peak at 5 MeV with a $\sigma = 18$ keV*

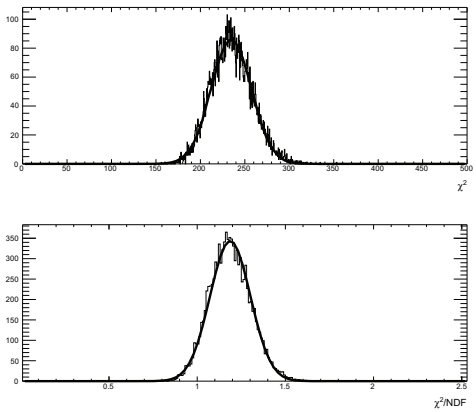

Figure 6.14: *χ^2 distribution obtained from a linear fit of 10000 simulated flat background plus a 130 counts gaussian peak as we can see in figure 6.13 (NDF=198)*

Now we have fixed the detection limit at 130 counts, let us start to give the minimum spectroscopic factor accessible in the experiment for a given energy. We know that the spectroscopic factor for the $L = 3$ state at 3.35 MeV is 2.4 using the finite-range calculation. The integral for this state at 21 degrees in the laboratory frame (where the cross-section is the highest) is about 700 counts. Then by fixing the detection limit at 130 counts we can establish the minimum spectroscopic factor we can access at this energy: $C^2S_{lim}(3.35) = \frac{130\times2.4}{700} = 0.44$. Now by comparing the different calculated cross

section in figure 6.15, we can determine a minimum spectroscopic factor as a function of the excitation energy. Thus we can see in figure 6.16 the different established C^2S_{lim} for different excitation energies giving the detectable area in our experimental setup with a confidence level of 95%.

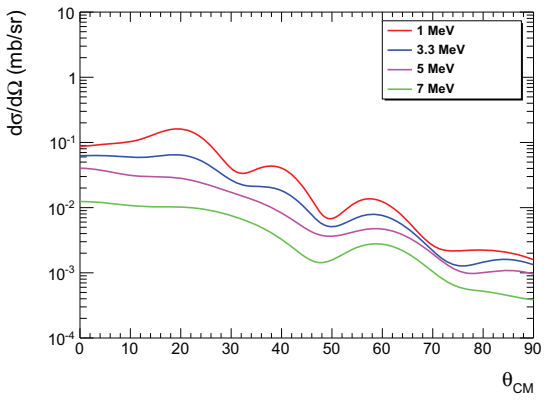

Figure 6.15: *Evolution of the cross section for $L = 3$ as a function of the excitation energy in ^{69}Cu using the finite-range DWUCK5 code*

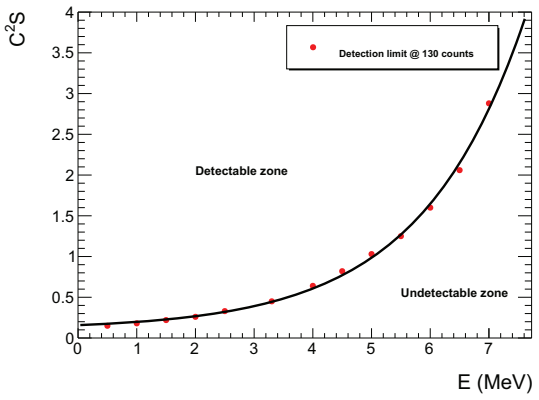

Figure 6.16: *Limit of detection as a function of the excitation energy. The limit depends on the limit number of counts to detect a peak with our detection system*

Actually, the behavior of C^2S_{lim} curve is exponential as a function of the excitation energy and follows this function:

$$C^2S_{lim}(E) = \alpha + \beta \exp(\gamma E). \tag{6.1}$$

The result of the fit as we can see on figure 6.16 gives:

$$\begin{cases} \alpha = 0.104 \pm 0.036 \\ \beta = 0.053 \pm 0.010 \\ \gamma = 0.562 \pm 0.027 \end{cases} \tag{6.2}$$

As we will see in section 10.3, we can use this constrain on the missing strength to estimate the $\pi f_{7/2}$ centroid.

6.4 Conclusion

In this work we have brought out spectroscopic information about the structure of ^{69}Cu by means of the ^{70}Zn(d,^{3}He) one-proton transfer reaction performed at Orsay using a deuteron beam at 27 MeV. We have used the missing-mass method with the split-pole spectrometer that could provide us a good resolution.
The results show clearly eight populated states. The five first states are in agreement with previous works [32, 34] except for the spectroscopic factor of the $5/2^-$ state at 1.23 MeV where they measured C^2S=1.5. One explanation could be the large error bars they obtained at low angle in the center of mass frame. In addition, we could determine three new angular distributions and learn more about the nuclear structure of ^{69}Cu at higher excitation energy up to 3.94 MeV. Especially, a new $L = 3$ state has been observed giving a total measured $\pi f_{7/2}^{-1}$ proton-hole strength of 66%. Finally a limit on the spectroscopic factor was given as a function of the excitation energy in order to constrain the missing strength.
Because we are interested in the evolution of this proton-hole strength evolution with the filling of the $g_{9/2}$ neutron orbital, toward ^{78}Ni, we shall now study the case of ^{71}Cu ($N = 42$) in the next part. This nucleus is the first Copper isotope with an even number of neutrons in the $\nu g_{9/2}$ orbital.

Part III

Single-particle states in ^{71}Cu

7
Experimental Setup

Contents

We describe in this chapter the experimental protocol used for the study of different reactions: the elastic scattering ^{72}Zn(d,d)^{72}Zn and two transfer reactions, ^{72}Zn(d,t)^{71}Zn and ^{72}Zn(d,^{3}He)^{71}Cu. The experimental contraints leading to the choice of the experimental setup will be explained. The data analysis as the simulations have been done using the NPTool[1] program developed at IPN Orsay [57, 58]. This program is based on Geant4 [59] for the simulations and on Root [60] for the analysis.

7.1 General presentation

In order to study the $\pi f_{7/2}^{-1}$ proton-hole states in a more neutron-rich Copper isotope such as the ^{71}Cu, one has to perform the transfer reaction in inverse kinematics: the deuteron is used as a target while the heavy ions, which is radioactive, here the ^{72}Zn, is the beam. Such a reaction has become achievable with the development of radioactive ions facilities that can provide accelerated exotic nuclear beams. Through the development of such facilities, study of single-particle energies far away from stability becomes possible. A review of the different technic for the production of radioactive ion beams and the different available facilities over the world are discussed by Y. Blumenfeld *et al.* in reference [61]. In direct kinematics the center of mass frame matches almost with the laboratory frame when the target nucleus is heavy enough, while in the case of inverse kinematics it is not the case anymore. This leads to very different kinematic lines by comparison to the direct kinematics case as we can see in figure 7.1 where we have plotted the kinetic energy of light particles as a function of the angle in the laboratory frame for three channels of reaction. In this experiment, we have performed the reaction with a secondary beam of ^{72}Zn at 38 MeV/nucleon that was transported toward a deuteron target.
Our goal is to perform angular distributions of the emitted light particles from the reaction. For that purpose it is important to know the kinematics of this two-body reaction in order to optimize the experimental setup for the detection of these light particles. Moreover, we need to couple this kinetic information with the probability of reaction. We know from DWBA calculations that the probability of reaction is higher at small angle in the

[1] Nuclear Physics Tool

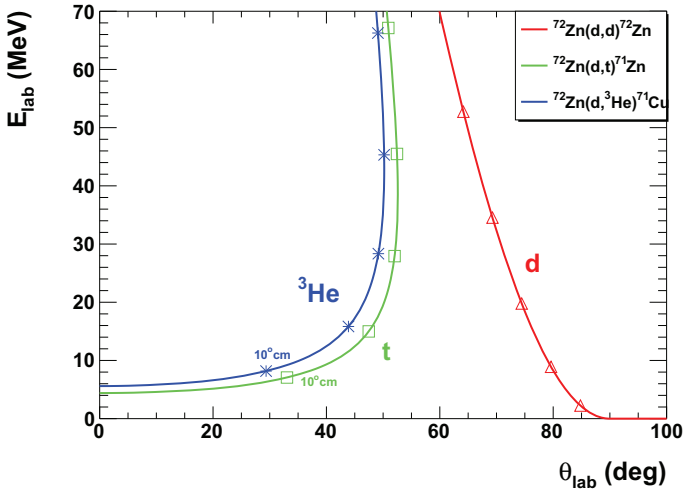

Figure 7.1: *Kinematics line of the different reactions. The elastic scattering in red, the (d,t) transfer reaction in green and the (d,^{3}He) in blue. Dots are plotted on the kinematic lines every 10^{o} in the center-of-mass frame*

center of mass frame, for $\theta_{CM} < 25^{o}$ that corresponds to $\theta_{lab} < 50^{o}$. For $\theta_{CM} > 25^{o}$, we lose at least one order of magnitude for the cross section. All these elements tell us to use a detection system placed at forward angles in the laboratory frame in order to determine the energy and the angle of the light particles (t and ^{3}He). To do so, we have used the charged particle detectors MUST2[2] to detect the ^{3}He emitted from the reaction. Four of them where placed at forward angles for the transfer reactions (d,^{3}He) and (d,t) while for the elastic scattering measurement we have used two MUST2 at ninety degrees. During this experiment two other MUST2 telescopes where also placed at backward angles for the (d,p) reaction channel.
Moreover, the energy of the emitted ^{3}He is smaller than 21 MeV for $\theta_{lab} < 47.5^{o}$ that corresponds to the energy for an ^{3}He to cross 300 μm of silicon, which is the first stage of the MUST2 array. This means that the ^{3}He are stopped in this first layer. So in order to discriminate the ^{3}He from the other light particles we need to add a 20 μm silicon detector in front of each MUST2 at forward angles to select our particles in a $E - \Delta E$ spectrum. The thickness of 20 μm is quite thin but if we have used thicker detector, the ^{3}He of very low kinetic energy would not have been detected because the residual energy in the

[2]MUr à STrips

MUST2 array would have been too low and under the threshold. Indeed you already need an ^{3}He of 4.1 MeV to cross 20 μm of silicon, and the ^{3}He of interest coming from the transfer reaction arise with a kinetic energy between 5.6 and 21 MeV.
Because the beam was produced by fragmentation, two beam tracking detectors were used in order to reconstruct the angle of the beam as the position of interaction on the target. These detectors were placed upstream the CD_2 target and enable us to determine the angle of the emitted ^{3}He particle.
Finally, in order to detect the heavy fragment from the reaction, we have used a plastic detector and an ionization chamber. The idea is to separate the heavy fragment by $E - \Delta E$ or $E - TimeOfFlight$ method.
In this way, it was possible to measure different reaction channels such as the (d,d), (d,t) and (d,^{3}He) reactions, in a large angle range in the same time. We can see a scheme of the experiment and a real picture in figures 7.2 and 7.3 respectively. It is quite different compare to the ^{69}Cu case where the setup was fixed for the only reaction of interest and the measurements were done angle by angle.

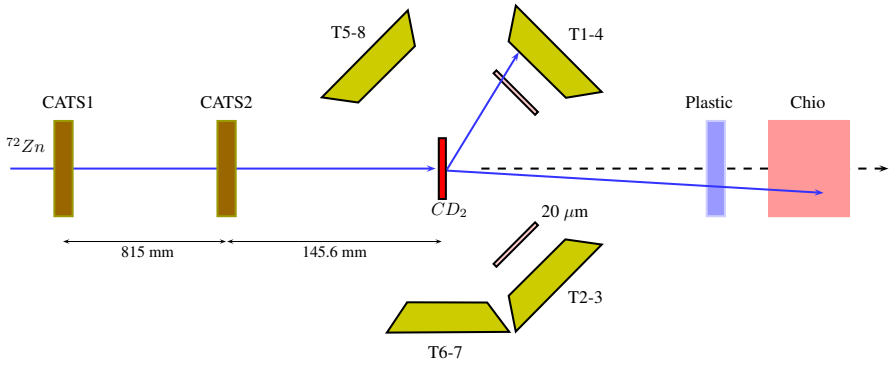

Figure 7.2: *Scheme of the experimental setup*

7.2 Beam production

The E552 experiment was performed in April 2011 at GANIL[3]. A general plan of the GANIL facility is shown in figure 7.4. One can see the three cyclotrons C01, CSS1 and

[3]Grand Accélérateur National d'Ions Lourds

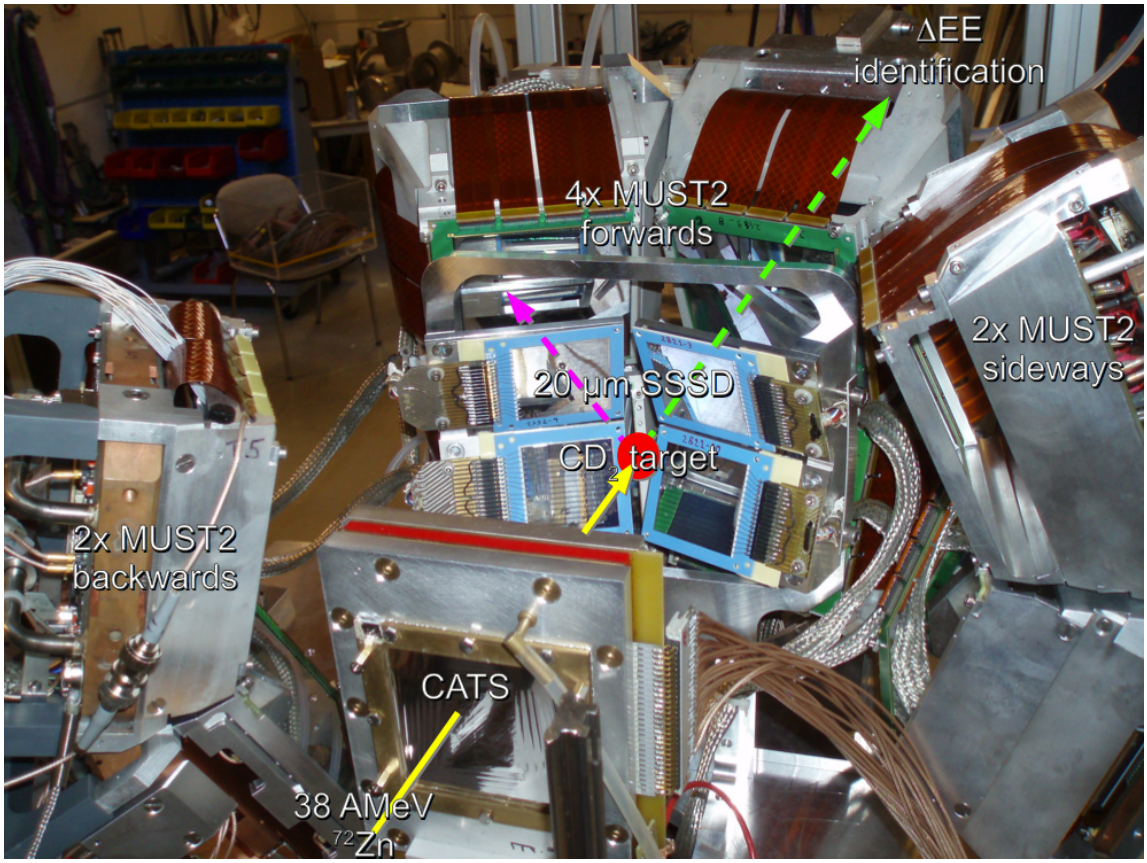

Figure 7.3: *Experimental setup on the Lise beam line at GANIL*

CSS2 that produce the required energy of the primary beam.
For our experiment, the secondary beam of ^{72}Zn was produced by fragmentation. The primary beam of ^{76}Ge was produced by an ECR[4] source that transforms into plasma the germanium. Then the primary beam was accelerated through C0, CSS1 and CSS2 cyclotrons up to 61 MeV/u at a frequency of 11.07 MHz and at an average intensity of 20 enA. It was sent toward the LISE[5] spectrometer [62] in order to produce the secondary beam by fragmentation with a ^{9}Be target of 732.8 μm thickness. After fragmentation the beam was purified through the LISE spectrometer.
We can see a schematic view of the LISE spectrometer in figure 7.5. It is mainly composed of two magnetic dipoles where the magnetic rigidity was $B\rho_1 = 2.3043$ T.m and $B\rho_2 =$

[4]Electron Cyclotron Resonance
[5]Ligne d'Ion Super Épluché

2.1466 T.m respectively. A wedge thickness of 223.5 μm is placed between the two dipoles in order two purify and slow down the beam to 38 MeV/u in our case. Once the thickness of the wedge fixed with the ratio $B\rho_1/B\rho_2$, each ion with the same value of $S = A^3/Z^2$ will be focused in the same place at the end of the spectrometer [63]. We can play also with the slits to perform more drastic selections of the beam. There is also a third dipole at the end of the line that is used to transport the beam in the experimental area. After the third dipole, there is a Wien filter [64] that is a velocity filter. In our experiment, it was no intended to use it, however it was used for few runs during the experiment to deviate a little bit the beam in order to avoid burning central wire of the beam tracking detector (CATS).
In addition a 300 μm silicon detector is placed in D6 in order to identify the different ions present in the beam. It consists of an energy loss ΔE in the silicon versus the time of flight between the silicon detector and the radio-frequency of the CSS2. We can see a typical spectrum in figure 8.2. In only few runs this information was encoded in order to see the different contaminants but not during the entire experiment.

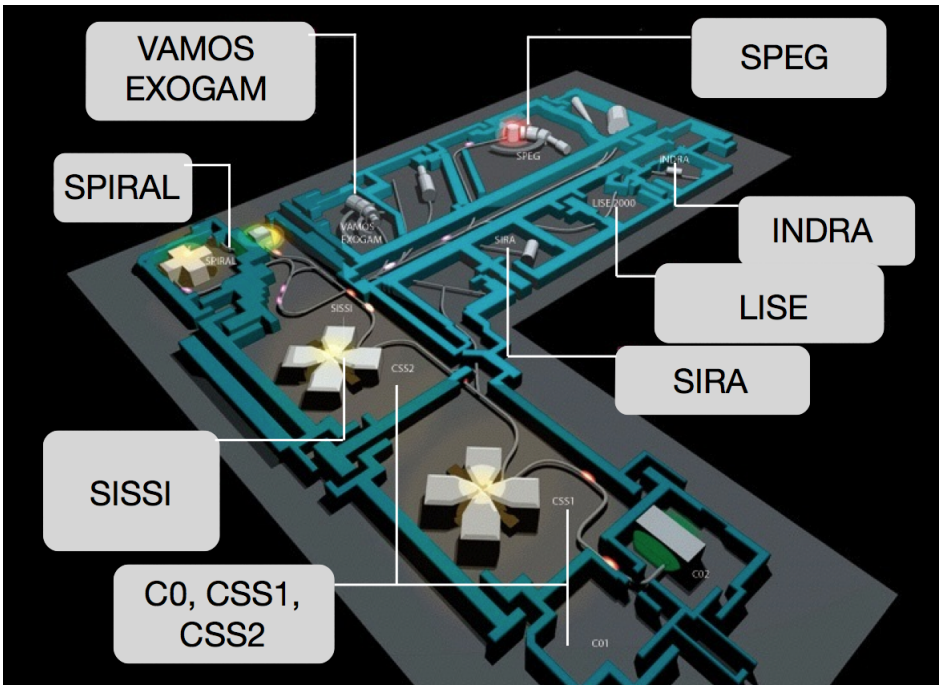

Figure 7.4: *Accelerator and experimental areas at GANIL*

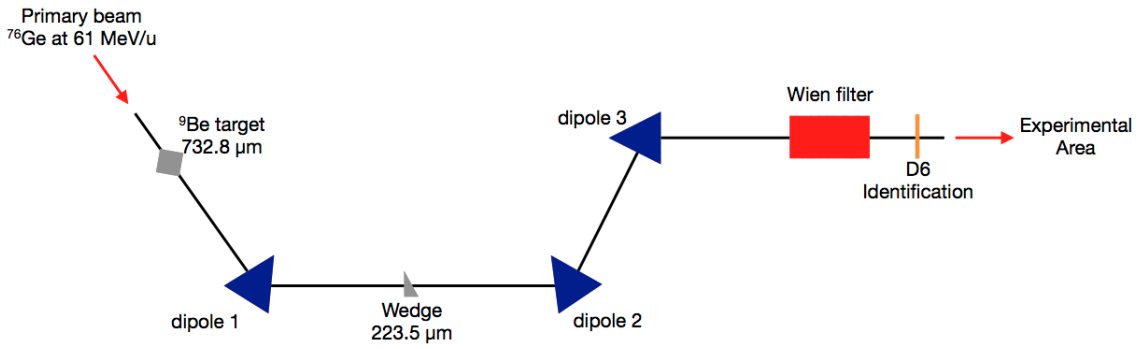

Figure 7.5: *Scheme of LISE spectrometer*

7.3 Targets

In our target holder we had four different targets. Three of them were a deuterated polypropylene (CD_2) target with a thickness of 0.26(2) mg/cm^2 for two of them and 0.68 mg/cm^2 for the last one. During all the experiment we ran with a thickness target of 0.26 mg/cm^2. This choice of thickness is a compromise to take between the statistics and the energy resolution. Indeed because our ^{3}He of interest have very low kinetic energy, the energy loss in the target is important, thus in order to keep a resolution in energy good enough we have to use a thin target.
The other main difficulty with this kind of target is that it is composed of ^{12}C, producing a background in the spectra due to the reaction between the beam and the carbon. That is why a last target was used, composed only of carbon, to evaluate the carbon background in our spectra. The thickness of this carbon target was 0.38(2) mg/cm^2.
In addition, for the CD_2 target, the quantity of proton is not zero. And we need to quantify it to well determine the number of deuteron in the target for the normalisation procedure. Thus the number of deuteron is:

$$N_{target} = \frac{2 f N_A e_{CD_2}}{M_C + 2(f M_d + (1-f) M_p)} \tag{7.1}$$

where f is the deuteron fraction in the target, M_C, M_d and M_p the mass of the carbon, deuteron and proton respectively, and $e_{CD_2} = 0.26$ mg/cm^2 is the target thickness. The quantity of protons was determined thanks to the elastic scattering of the ^{72}Zn with the

protons of the target and the quantity $f = 0.98$ was established (see section 9.1.1), giving $N_{target} = 1.923 \pm 0.096\ 10^{19}$ at/cm^2.

7.4 Beam tracking detector : CATS

Beams produced by fragmentation have a large emittance. In order to know the position of interaction on the target and the beam angle event by event with a precision good enough we have used two beam tracking detectors. In addition, these detectors are also used to count the incident beam and provide us a good time information.
In the experiment, we have used two CATS[6] detectors [65]. This detector is a low pressure multi-wire proportional chamber (figure 7.6) used with an isobutane gas (C_4H_{10}). The gas pressure depends on the ion beam and the pressure used in our experiment was 10 mbar. The active area of this detector is 70×70 mm^2. There are two Mylar foils 1.5 μm thick that contain the gas inside. Each detector is made of an anode that is a plane of 71 anode wires in tungsten which have a diameter of 10 μm and there is 1 mm between each wire. In this anode plane we put a high voltage between 600 and 800 V. Either side of the anode there are two cathode planes at a distance of 3.2 mm which are perpendicular between them. The fact that the cathode is segmented provides us with the position information. Each cathode contains 28 gold strips spaced by 0.2 mm and 2.34 mm thick. Then we are able to reconstruct the beam position on the target event by event with a precision less than 1 mm.
The maximum count rate for this detector is about 10^5 particles per second if the beam is not too focused on one part of the detector.

7.5 Detection devices

7.5.1 MUST2 detector

The MUST2 detector [66], was designed to detect the light charged particles emitted from direct reaction of exotic nuclei in inverse kinematic. This detector was already often

[6] Chambre À Trajectoire de Saclay

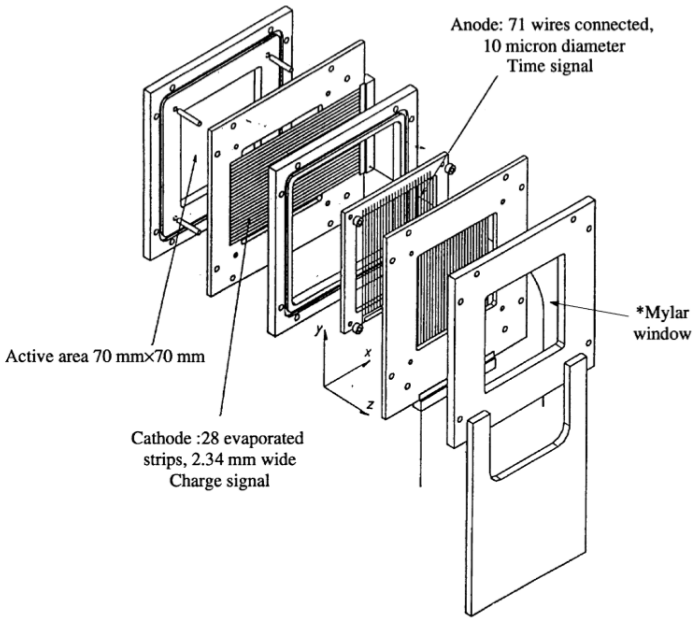

Figure 7.6: *Characteristics of a CATS detector*

used as we can see in the PhD thesis of D. Daisuke [67], S. Giron [68], A. Matta [58] and F. Flavigny [69] for instance. Each telescope is made of three stages (figure 7.7):

- **300 μm silicon** : The first layer is a double sided stripped silicon detector (DSSSD) of 300 μm thickness and the area of this detector is 98×98 mm^2. On both side of the silicon there is an evaporated layer of aluminum of 0.4 μm thickness and each aluminum layer is divided into 128 strips vertically or horizontally. The strip pitch is 0.75 mm, so the angular resolution is 0.15 degree at a distance of 15 cm and the typical energy resolution for a strip is 40 keV. Thus, this DSSSD provides us the energy loss as the time information and also the position of the particle.

- **SiLi** : The second stage of the telescope is a lithium-drifted silicon detector with a thickness of 4.5 mm and an active area of 92×48 mm^2. It is composed of two detectors themselves segmented into 8 pads. For this experiment, the SiLi detector were mounted only on the two MUST2 detectors place at backward angles.

- **CsI** : Finally the last stage of the telescope is made of 16 CsI calorimeter. Each crystal with a thickness of 40 mm is read by a photo-diodes with the same electronics

of the first stage. The area of each crystal is 30×30 mm^2. This last stage measures the residual energy of the light particles which have crossed the other layer(s) of the telescope.

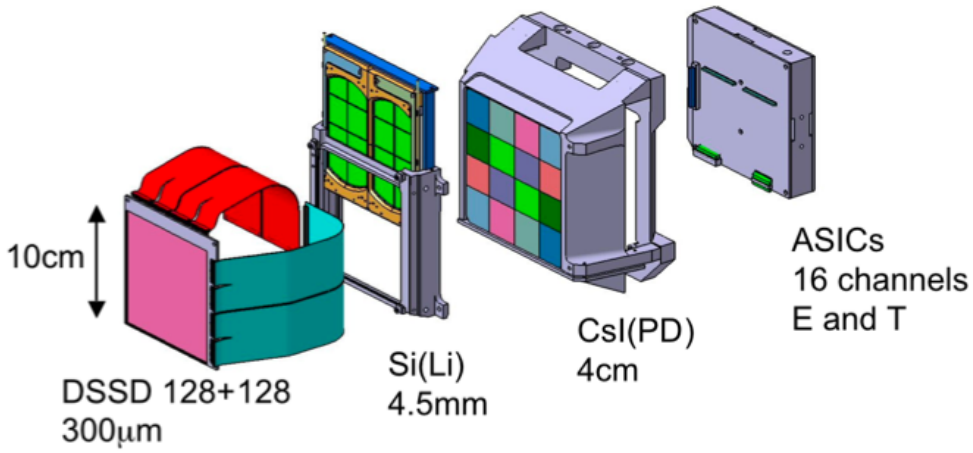

Figure 7.7: *MUST2 detector*

Electronics

The electronics of MUST2 detector is based on ASIC[7] modules which are called MATE[8]. Behind each telescope there is a cooling system designed for the two MUFEE[9]. With the MUVI[10] these three cards constitute the elements of the MUST2 electronics.

- One **MATE** is able to treat 16 strips, which means 16 analog signals. It provides the pre-amplification of the signal and divides the signal in a time and energy signal. If the time signal is higher than the the threshold, two signals are emitted. One of them is a start that will trigger the TAC (Time to Amplitude Converter) used to measure the particle time of flight (the stop signal is external and corresponds to one CATS detector). The second one is a reading request sent to the MATE output.

[7] Application-Specific Integrated Circuit
[8] Must2 Asic Time and Energy
[9] MUst2 Front End Electronic
[10] MUst in VxI

Regarding the energy signal, it is filtered and stocked in a capacitance waiting for the reading order. In this case the signal is encoded in 14 bits. The channels 8192 to 16384 correspond to the X strips while the channels from 8192 to 0 corresponds to the Y ones.

- The **MUFFE** card contains nine MATE. Eight of them are dedicated for the 128 strips of one side of the DSSD and the ninth treats the signals from the SiLi for the MUFEE of the X side and the signals from the CsI for the Y side. Two cards are needed to entirely treat a MUST2 telescope which correspond to 576 parameters. These two cards allow the multiplexing and the transmission of the data to the ADC (Analog to Digital Converter). Moreover this card provides the power supply (bias and high voltage) for the detectors and there is inside a pulse generator to test and calibrate the electronics and finally a temperature probe is able to start an alarm signal if it exceeds a threshold fixed by the user.

- The **MUVI** card deals with all the electronics. It is placed outside the chamber in a VXI crate. When an event is accepted by the trigger, the MUVI card starts the reading of the MUFEE cards, the encoding of the data and the transmission to the acquisition. In other case it orders the reset of the MUFEE which has triggered. In addition it transmits the extern stop signal to the TAC of the MATE. This card is also able to perform low level filtering such as the pedestal subtraction.

Efficiency

As we said before, the light particles such as the triton and the ^{3}He are emitted at forward angles in the laboratory frame. Because the setup was designed to detect the ^{3}He, we want a maximum efficiency of detection for the forward angles between 8 and 50 degrees in the laboratory frame. As we can see in the figure 7.8 for telescope 1 to 4, the simulated efficiency of our reaction of interest producing ^{71}Cu in its ground state is higher than 50% between the angles 13 and 42 degrees in the laboratory frame and it reaches a maximum of 90 % around 35 degrees. Finally the efficiency of the two MUST2 telescopes (6 and 7) at ninety degrees for the elastic scattering reach 20% between 68^{o} and 87^{o} in the laboratory frame (figure 7.9).

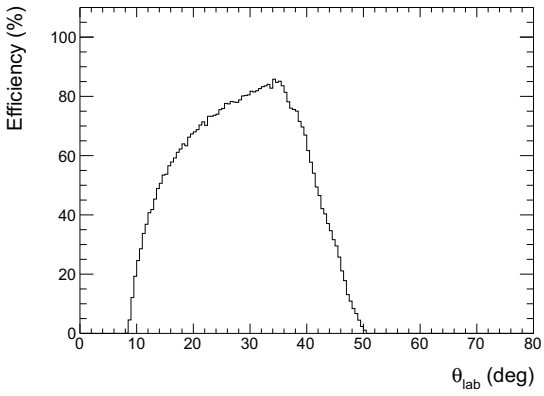

Figure 7.8: *Efficiency of the detection setup in the laboratory frame for T1-4 for the (d,^{3}He) transfer reaction producing the ^{71}Cu nucleus in its ground state*

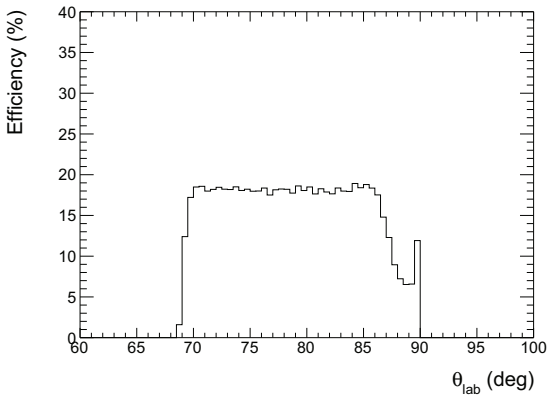

Figure 7.9: *Efficiency of the detection setup in the laboratory frame for T6-7 for the (d,d) elastic scattering*

7.5.2 20 μm silicon detector

Because of the kinematics, the ^{3}He emitted from the reaction have a kinetic energy below 22 MeV. Therefore they are stopped in the first stage of MUST2. In order to separate them from the other light particles such as ^{3}H and α particles the only way is by the time of flight method. Because time of flight separates only in mass we cannot distinguish between ^{3}H and ^{3}He. In order to perform a $E-\Delta E$ identification, we added a 20 μm silicon detector in front of each MUST2 telescope (T1-4) at forward angles. These detectors are Single Sided Stripped Silicon Detector (SSSSD) with 16 strips in the front side. The active area of the detector is 50×50 mm^2 and the typical energy resolution is 100 keV FWHM.
In order not to block the detection surface of MUST2, the SSSSD were mounted on an aluminum frame 67 mm from the DSSSD as we can see in figure 7.10. In this way no active area is lost for the detection.

7.5.3 Plastic

The plastic detector is a NE104 scintillator block with a thickness of 2 cm and an

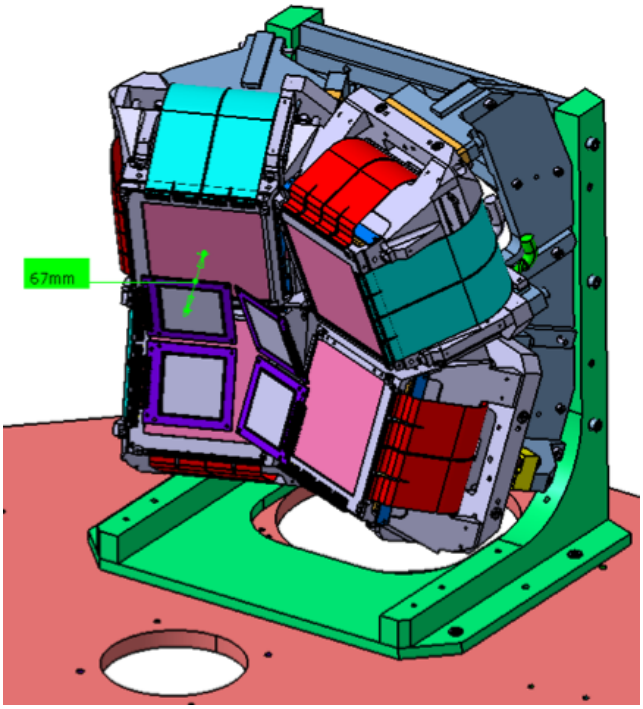

Figure 7.10: *SSSSD detectors in front of the MUST2 telescope.*

active area of 6×6 cm^2 connected to a light-guide and a photo-multiplier. This detector measures the residual energy of the heavy fragment. Its good time resolution can be used to determine the time of flight between one of the CATS detector and the plastic.

7.5.4 Ionization chamber

For this experiment, we have used an ionization chamber of which the signal was digitized. This digitized ionization chamber was used for the first time for the PhD thesis of G. Burgunder [70]. The aim of using an ionization chamber and a plastic is to identify the heavy fragment from the reaction at zero degree. Moreover, because the beam is produced by fragmentation there are also contaminants. That is why this detector is particularly useful.
The ionization chamber has an area of 60×60 mm^2 and is 12 cm long. The two entrance windows are composed of 7 μm thick Mylar foil. The gas used inside is CF_4 at a pressure

of 100 mbar. The cathode situated on top of the detector is connected to a potential at -600 V while the anode at the bottom is at +600 V. The Frisch grid situated 2 cm on top of the anode is fixed on ground potential. Thus the electric field in the drift region between the Frisch grid and the cathode is 2 V.cm^{-1}.Torr^{-1} while the one between the Frisch grid and the anode is 6 V.cm^{-1}.Torr^{-1}. In order to have a good gradient in the drift region, the walls of the chamber have several conductive bands perpendicular to the electric field which are equipotentials.
If we want a count rate about 10^5 pps, the duration of the signal has to be less than 10 μs. The pre-amplifier gain chosen was 360 mV/MeV and the sampling frequency was $f_s = 40$ MHz or one sample every 25 ns. For our sampling we have stocked 350 points per event which means a time of 8.75 μs.

7.5.5 Electronics and data acquisition

The different signals emitted from the different detection systems for the experiment require a logical acquisition. It is defined to avoid a useless trigger that does not correspond to the physics. During the read-out the system is blocked and cannot be used, this is what we call the dead time.
The trigger logic of experiments performed with the MUST2 arrays relies on the GMT[11], which is placed in a VXI crate. It can accept until 16 logic signals authorized to trigger. For the E552 experiment, the events were recorded when one of the following conditions was fulfilled:

1. one of the MUST2 telescope is triggering,
2. one of the CATS divided is triggering,
3. one of the SSSD divided is triggering,
4. plastic divided is triggering,
5. or CHIO divided is triggering.

The first trigger corresponds to the selection of good events while the second one allows us to count the number of incident ions. When one of the logic signals is present at the

[11] Ganil Master Trigger

GMT, it generates a logic signal called FAG[12]. For an event to be treated, the time signal associated to the triggered detector has to be in coincidence with the FAG. The stop signal which is in common for all the detectors is the delayed logic signal from CATS2 and validated by the FAG while the start signal comes from the detectors which has triggered (it comes from MUVI for example in the case of MUST2). Once the signal is accepted, it is encoded by the electronics allowing to stock the energy and the associated time of the event.

[12]Fenêtre d'Acquisition du Ganil

8
Data analysis

Contents

In this chapter we present into details the analysis methods used in order to extract the variables of interest. We detail how we reconstruct the beam trajectory and the beam position on the the target thanks to the CATS detectors, as how we treat the thickness inhomogeneity of the SSSSD detectors in order to identify the light charged particles in a $\Delta E - E$ spectrum with the DSSSD.

8.1 Beam selection

The secondary beam of ^{72}Zn produced by fragmentation at an average intensity of 1.5 10^5 particles per second was not pure. In order to identify all the contaminants of the beam, we have used some LISE runs thanks to $\Delta E - TimeOfFlight$ spectrum in D6. We can see in figure 8.2 the contaminants present during the experiment. However during the experiment, LISE was not in the trigger. So in order to select only the ^{72}Zn beam we used a cut in the time-of-flight spectrum between the HF and the beam tracking detector CATS1. As we can see in figure 8.1 the purity of the beam is $P(^{72}\text{Zn}) \approx 55\%$ and one can see that the main contaminant is ^{74}Ga together with the ^{76}Ge primary beam. For all the analysis, the following condition 10000 < TAC-CATS1-HF < 11200 is applied in order to only select our secondary beam of interest. By applying this condition the relative purity of ^{72}Zn is 90.6% and the one of ^{74}Ga is 9.4%. Then contamination coming from the ^{74}Ga(d,^{3}He)^{73}Zn should be fairly low.

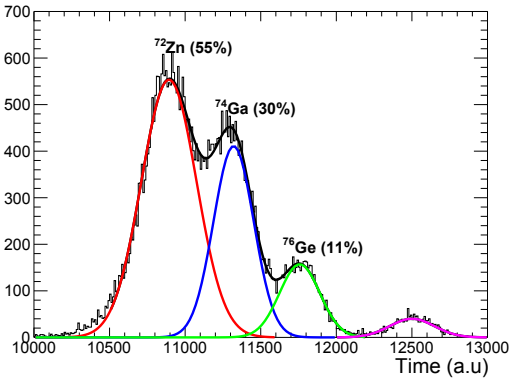

Figure 8.1: *Time CATS1-HF used to select the ^{72}Zn beam*

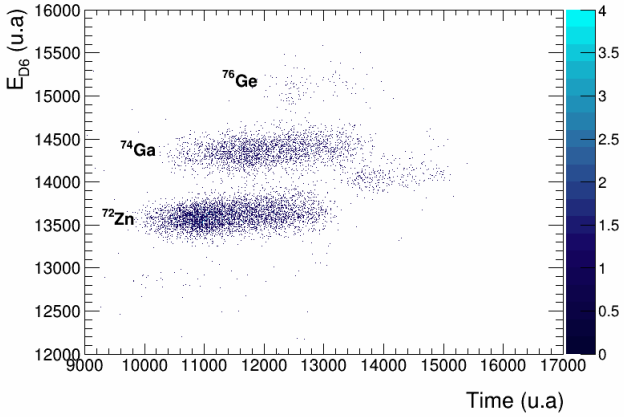

Figure 8.2: *Identification spectrum in D6*

8.2 CATS

The beam-tracking detector CATS was already used in different experiments done at GANIL. We shall treat here how we extract the beam position on the target through different analysis methods.

8.2.1 Calibration

In order to calibrate each strip of the detector we used a pulse generator sent into the anode of the detector. There is then an induced charge on the two cathodic strips plane. By varying the amplitude of the signal delivered by the generator we obtain different peaks that we can determine the position and the resolution (σ) of the signal thanks to a Gaussian fit. We also measure the pedestal, its position P_i and its sigma σ_i for each strip i. After subtraction of the pedestal, a second-order fit is performed. We have the following relation for each strip i for the calibration of the charge Q_i^{cal}:

$$Q_i^{cal} = A_i^0 + A_i^1(Q_i^{raw} - P_i) + A_i^2(Q_i^{raw} - P_i)^2, \tag{8.1}$$

where the A_i^j are the fit parameters of the second-order fit for strip i. We can see the result of the calibration in figure 8.4 for the strips Y of CATS2 detector. It is also important to

note that the position of the pedestal P_i and its sigma σ_i are used to define the threshold of the detector S_i. We consider that a strip is touched if the signal is higher than the threshold defined as follows:

$$S_i = P_i + m\sigma_i \tag{8.2}$$

with $m = 3$ for this analysis.

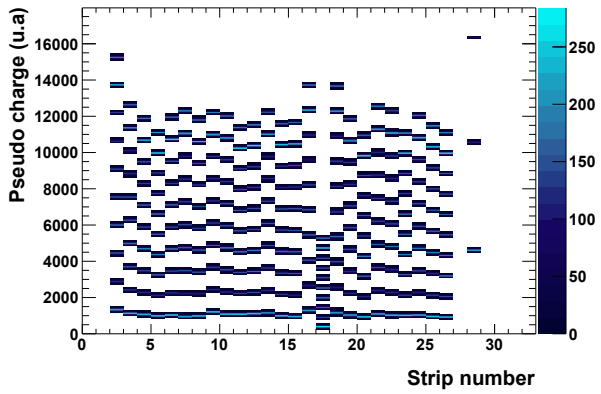

Figure 8.3: *Pseudo charge versus strip number of CATS2 Y before calibration*

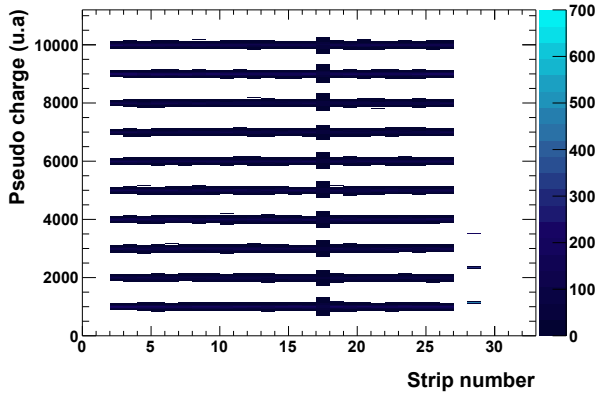

Figure 8.4: *Pseudo charge versus strip number of CATS2 Y after calibration*

8.2.2 Reconstruction methods

In order to have the best possible precision, it is important to determine the centroid of the deposited charges on the X and Y planes. Different methods are available to reconstruct the beam position, we are going to discuss them one by one.

The hyperbolic secant method

In the case where three contiguous strips are touched by a crossing ion, the common way to treat it is to use the hyperbolic secant method. The advantage is the analytical formula of this method. Let us consider a strip N_m that has the largest charge Q_m and the contiguous strips N_{m-1} and N_{m+1} with the respective charge Q_{m-1} and Q_{m+1}. I remind

that the width of a strip is $L = 2.54$ mm. Then the centroid position of the charge is given by [68, 65]:

$$S_h = \frac{a_3}{\pi}\tanh^{-1}\Big(\frac{\sqrt{Q_m/Q_{m+1}} - \sqrt{Q_m/Q_{m-1}}}{2\sinh(\frac{\pi L}{a_3})}\Big) \tag{8.3}$$

where

$$a_3 = \frac{\pi L}{\cosh^{-1}\Big(\frac{1}{2}(\sqrt{Q_m/Q_{m+1}} + \sqrt{Q_m/Q_{m-1}})\Big)}. \tag{8.4}$$

The disadvantage of this method is that we cannot use it when a strip is missing. For example when a strip is burnt. It was the case for the last third of the experiment for CATS2 detector because the beam was too much focused on this detector, which was positioned too close to the target. When such a case appears we can use the Gaussian method to determine the centroid of the position.

The Gaussian method

As we said, the Gaussian method is used when a strip is not available to determine the centroid. With this method the centroid is given by [68, 65]:

$$G = \frac{1}{2}\frac{\ln\Big(\frac{Q_m}{Q_{m-1}}\Big)(X_{m+1}^2 - X_m^2) - \ln\Big(\frac{Q_m}{Q_{m+1}}\Big)(X_{m-1}^2 - X_m^2)}{\ln\Big(\frac{Q_m}{Q_{m-1}}\Big)(X_{m+1} - X_m) - \ln\Big(\frac{Q_m}{Q_{m+1}}\Big)(X_{m-1} - X_m)}. \tag{8.5}$$

Here, the strips are not necessarily contiguous. Q_m is the largest charge on the strip N_m, but if the strip next to the right for instance is not available, we use the next strip with its charge. This method is available when a maximum of two contiguous strips are missing. During our experiment one of the central strip was deteriorated due to beam intensity (strip X 16 of CATS2), this had led us to use this method.
I have explained the possible methods to reconstruct the centroid on CATS detector. For the analysis the hyperbolic secant method was always used for the CATS1 detector while for the CATS2 detector it was used until the strip $X16$ had burnt. From this point the Gaussian method was chosen[1].

[1] From run 329

Reconstruction with mask

In order to check the reconstruction of the beam spot on target, we have used two masks. One in front of the CATS 1 detector and the other one placed on the target holder.
In order to see the beam reconstruction on CATS, we have to trigger with the ionization chamber or the plastic. We can see the reconstruction of mask 1 in figure 8.5. For this reconstruction the slits were set too narrowly closed, that is why we only see a vertical line and one spot. The reconstruction is good for CATS 1 and no wire was missing during the experiment. For the CATS 2 detector, we used a second mask placed on the frame of the target. Because this was done later in the experiment, strip X 16 of CATS2 was not available because already burnt. Different methods have been used in order to improve the reconstruction. We can see in figure 8.6 that the image on target using the Gaussian method remains deformed because of the missing strip. However the resolution of the excitation-energy spectrum of the elastic scattering and also transfer reaction was the same before and after this strip had burnt.

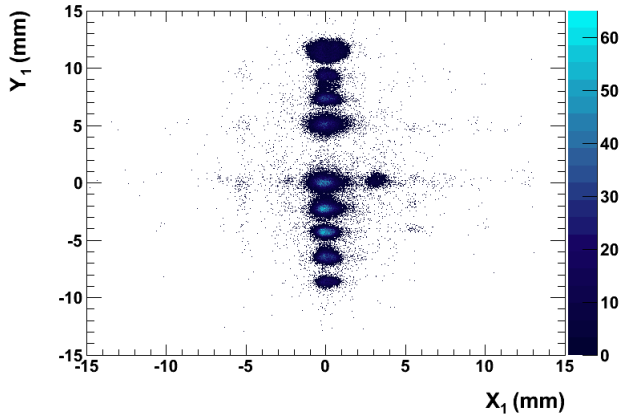

Figure 8.5: *Image of mask 1 using the hyperbolic secant method for the reconstruction*

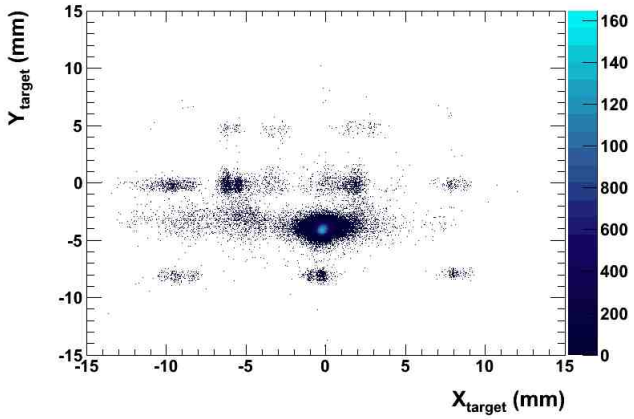

Figure 8.6: *Image of mask 2 placed on the target holder. This run occurred after the strip X16 of CATS2 had burnt*

8.2.3 Reconstruction of the beam on the target

When we have the good reconstruction on the CATS detectors, we have to reconstruct the beam on the target in order to have the position of interaction. If we consider the beam axis as the Z-axis and if the target is perpendicular to the beam, then the (X_{target}, Y_{target}) position is:

$$\begin{cases} X_{target} &= X_1 + (X_2 - X_1)t \\ Y_{target} &= Y_1 + (Y_2 - Y_1)t \end{cases} \tag{8.6}$$

where $t = \frac{l+L}{l}$ and L is the distance between CATS 2 and the target and l the distance between the two CATS.
During the experiment there was an angle $\alpha = 28$ degrees between the beam axis and the target plane. It is necessary to take it into account for a good reconstruction. We now explain how we determine the new coordinates. As we can see in figure 8.7 the equation of the target is:

$$Z_{target} = X_{target}\tan\alpha. \tag{8.7}$$

The equation of the beam in blue is:

$$z_{beam} = ax_{beam} + b, \tag{8.8}$$

where a and b are the two constants we have to determine. The coordinates of CATS correspond the the equation of the beam such as:

$$\begin{cases} Z_1 &= aX_1 + b \\ Z_2 &= aX_2 + b. \end{cases} \tag{8.9}$$

Thus we are able to determine a and b:

$$a = \frac{Z_2 - Z_1}{X_2 - X_1} \tag{8.10}$$

and

$$b = Z_1 - \frac{Z_2 - Z_1}{X_2 - X_1}X_1. \tag{8.11}$$

Finally in order to know the position of interaction, we have to resolve $Z_{target} = z_{beam}$:

$$aX_{target} + b = X_{target} \tan \alpha, \tag{8.12}$$

which gives:

$$X_{target} = \frac{b}{\tan \alpha - a}. \tag{8.13}$$

Now we know X_{target}, we have to determine Y_{target}. Actually for Y_{target} it is the same equation as 8.6 when one has to replace L by $L + Z_{target} = L + X_{target} \tan \alpha$.

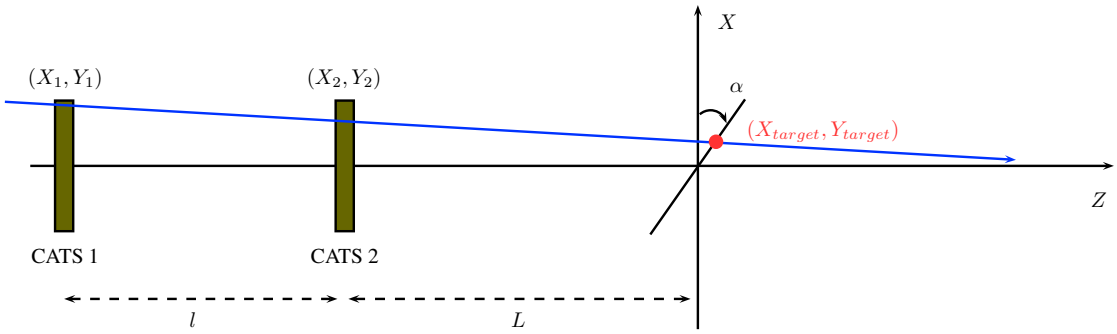

Figure 8.7: *Scheme of beam reconstruction on target*

We can see in figure 8.8 the profile of the beam on CATS1 and CATS2, and the reconstruction of the beam on the target. We have typically on the target $\Delta X \approx 20$ mm and $\Delta Y \approx 8$ mm.

8.3 MUST2 telescope

8.3.1 Energy calibration

The DSSSDs consist of 128 strips on each side of the detector, the X and the Y signals. These signals are read-out by two MUFFEE cards and are of different polarities. That's why the X signals which are of positive polarity are coded from the channel number 8192 to 16384, while the Y signal of negative polarity are coded from 8192 to 0. Thus, the channel that corresponds to the zero energy is the channel 8192. That is why the pedestal

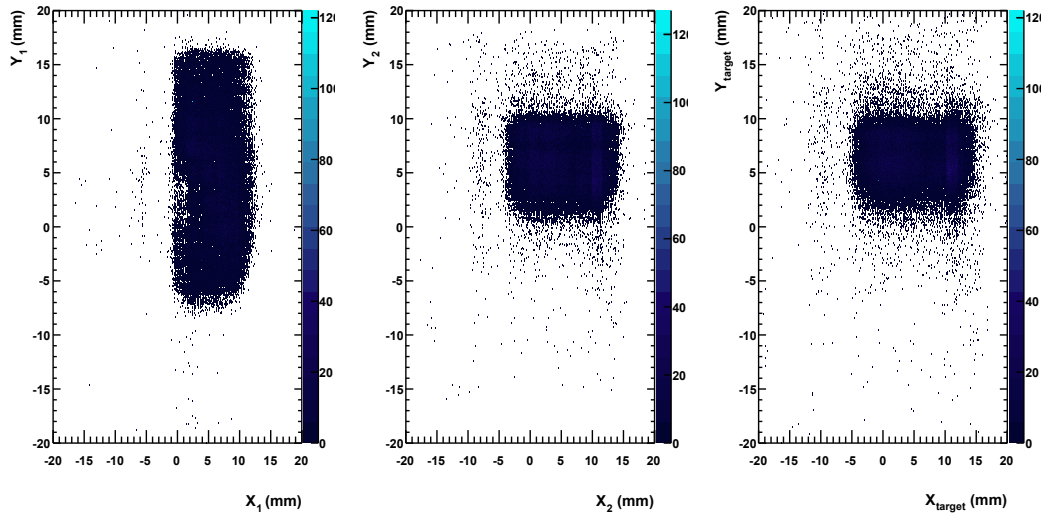

Figure 8.8: *Beam profile on CATS1 on the right, CATS2 on the middle and on the target on the left*

of the different channels is measured before the experiment and realigned between them in the DAS[2] to be the channel 8192.
The three-α source (^{239}Pu, ^{241}Am, ^{244}Cm) was used to calibrate all the strips at the beginning and at the end of the experiment. The three nuclei from the source that are unstable, decay by emitting α particles with well defined energy listed in table 8.2. Each main peak and their satellites were fitted by a sum of Gaussian function for each strip of the DSSSD in order to find a relation between the channel and the energy.
One of the main problem for the calibration of silicon detector is the determination of what we call the dead layer. This dead layer, of which the thickness is not accurately known, is made of aluminum in order to collect the charges, but also of a layer of inert silicon. The α particle loses some energy crossing this material and may induce a systematic error if we do not take it into account. The calibration procedure has determined the dead-layer thickness performing a zero-extrapolation method. In this procedure, we minimize the difference between the position of the calculated pedestal from the fit to the aligned pedestal at the channel 8192. We can see the thickness of the dead layer for the different telescopes in table 8.1.

[2]Data Acquisition System

Detector	Al thickness (μm)
1	0.48
2	0.57
3	0.59
4	0.59
5	0.56
6	0.52
7	0.53
8	0.56

Table 8.1: *Effective aluminum dead layer thickness for MUST2 telescopes*

Source	E_α (MeV)	Relative Intensity	$T_{1/2}$ (year)
	5.15659(14)	70.77(14)	2.411 10^4
^{239}Pu	5.1443(8)	17.11(14)	
	5.1055(8)	11.94(14)	
	5.48556(12)	84.8(5)	432.2
^{241}Am	5.44280(13)	13.1(3)	
	5.38823(13)	1.66(2)	
^{244}Cm	5.80477(5)	76.40(12)	18.1
	5.76264 (3)	23.60(12)	

Table 8.2: *Three-α source energies*

It is possible to sum up each strip for a same detector and fit the result with a sum of Gaussian functions with a fixed relative height corresponding to the decay rate. Then we determine the resolution for each peak. We can see the result of such a fit in figure 8.9. The asymmetric shape of the signal is due to the lower energies of the satellite peaks. The result of the resolution for all the telescopes are summarized in table 8.3. The typical resolution is 40 keV FWHM.

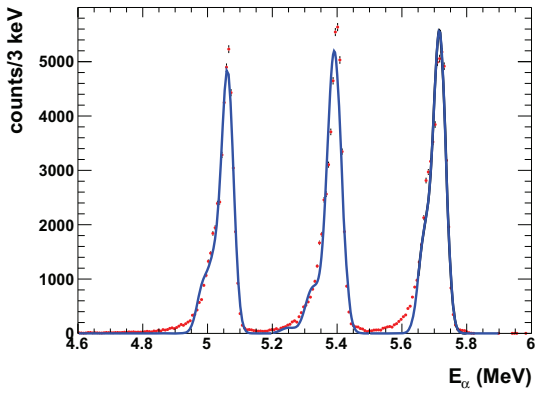

Figure 8.9: *α source energy spectra obtain after summation of all the X strips of telescope 2.*

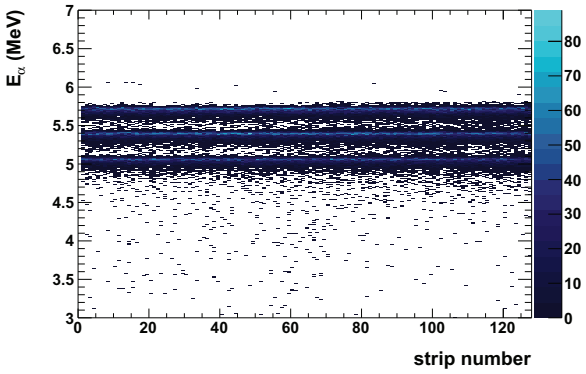

Figure 8.10: *α particle energy in telescope 2 versus the number of strip X. All the strips are well aligned between them.*

Detector	σ_{Pu} (keV)	σ_{Am} (keV)	σ_{Cm} (keV)
1	24	25	23
2	18	22	19
3	19	22	21
4	24	25	23
6	21	23	22
7	19	21	24

Table 8.3: *Average resolution of the MUST2 telescopes for each peak of the three-α source*

8.3.2 Time calibration

The time calibration was performed thanks to a time calibrator module generating a start and stop signal for each strip. The stop signal is delayed compare to the start signal by a fixed number of period varying to cover the whole range. Here the range was 640 ns with a period of 10 ns. The calibration is done at second order taking the first peak as reference. We can see in figure 8.11 a typical spectrum of the time calibrator for the sum of all strips Y of telescope 4. The width is $\sigma = 0.12$ ns giving 282 ps resolution FWHM. Because there is no absolute time, the different telescopes are not necessarily

aligned between them after the calibration. That is why we have to make a selection telescope by telescope.
Actually the correct total time resolution is evaluated at 1 ns because this resolution has to be correlated with the time resolution of the stop signal given by CATS detector.

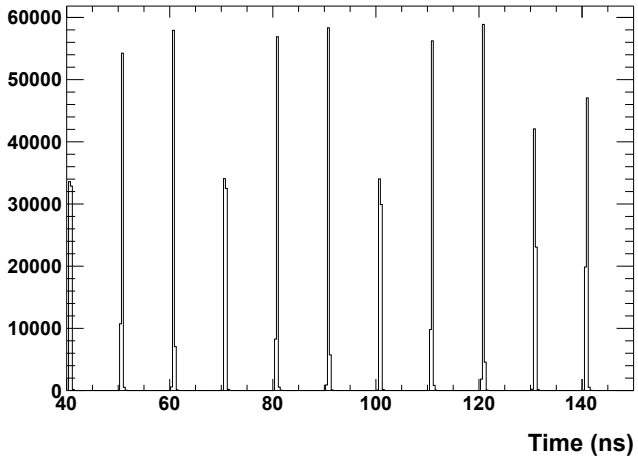

Figure 8.11: *Time calibrator peak for telescope 4. The period between two peaks is 10 ns and the resolution is* $\sigma = 120$ *ps.*

8.4 20 μm Simple Sided Stripped Silicon Detector (SSSSD)

8.4.1 Energy calibration

The 20 μm silicon detectors (SSSSD) were already used in the PhD experiment of A. Matta [58] where he highlighted the problem concerning the energy calibration and the thickness inhomogeneity of these detectors. I will explain here the main issues to calibrate these detectors and to perform a thickness map.
We have used the three-α source in order to perform a calibration of the SSSSD. The range of α particles exceeds the thickness of the detectors, so it was necessary to get

down this 3-α source by 16 cm in order to increase the effective thickness to stop the particle in the active part of the detector, which means increase the incident angle of the α particles. The procedure of calibration is the same as the one used for MUST2. The energy resolution deduced from the calibration for each detector is summarized in table 8.4. And we can see in figure 8.12 a Gaussian fit of the three-α source for all strips of detector 1.

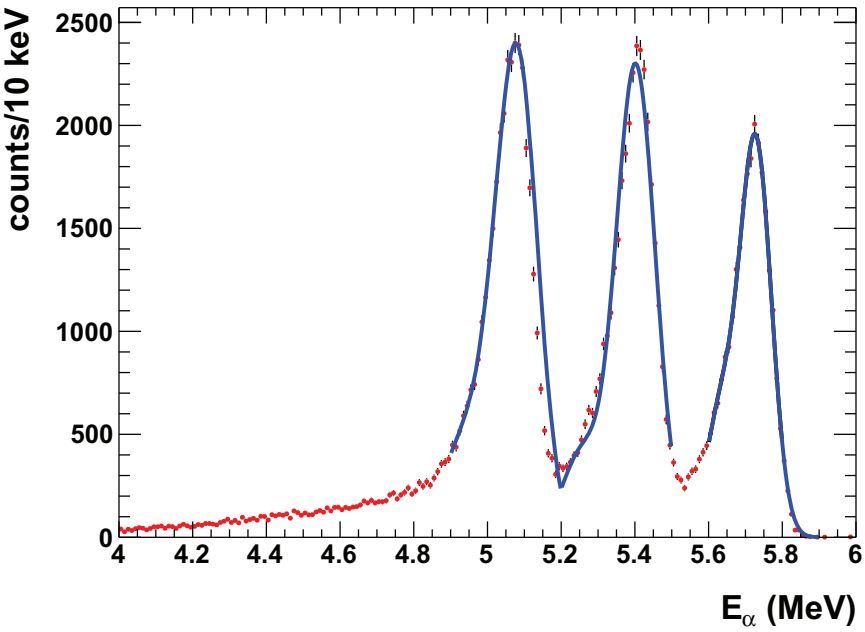

Figure 8.12: *α source energy spectrum obtained after summation of all the strips of detector 1.*

Detector	σ_{Pu} (keV)	σ_{Am} (keV)	σ_{Cm} (keV)
1	54	53	42
2	52	49	43
3	55	60	57
4	59	55	56

Table 8.4: *Average resolution of the SSSSD detectors for each peak of the three-α source. The average width is $\sigma = 52$ keV giving 122 keV FWHM.*

8.4.2 Thickness

The aim of the SSSSD is to perform a $E - \Delta E$ matrix between these 20 μm silicon detectors and the first stage of MUST2 in order to identify ^{3}He from α particles. We can see in figure 8.13 the $E-\Delta E$ spectrum for the 3-α source. We see three lines corresponding to the three different energies proving the thickness inhomogeneity of the SSSSD detectors. Indeed in this same figure the red circles correspond to the same spectrum by selecting one pixel in MUST2. If the SSSSD thickness were homogeneous, the three blue lines should have been as large as the red area. This inhomogeneity makes impossible the

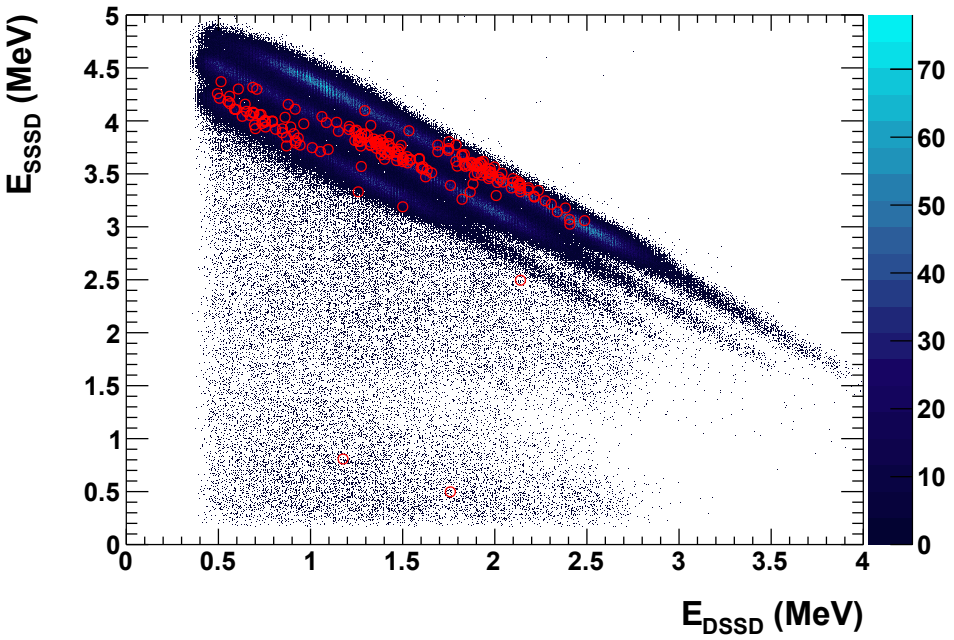

Figure 8.13: *E-ΔE spectrum for all strips of telescope 1 in color. The red circle correspond to the same data for one pixel in MUST2, here $X = 56$ and $Y = 64$.*

identification between ^{3}He and α particles in a $E - \Delta E$ spectrum. It is necessary to perform a thickness map of the SSSSD to correct of this effect.
To determine the thickness we have used the alpha peak with the highest energy at 5.80477 MeV and the energy loss table of such a particle in silicon material. A scheme

of the procedure is visible in figure 8.14. I list here the different steps used to determine locally the thickness:

- We know the position of the α-source (X_0, Y_0) and its energy,
- We know the position of interaction in MUST2 (X_M, Z_M), so the angle θ_n,
- We know the energy measured by MUST2, so we know the energy loss in the SSSSD.
- We can then determine the effective silicon thickness thanks to the energy-loss table of α particles in silicon material.

Because the SSSD is situated at $l = 67$ mm from MUST2, we can reconstruct the position of interaction in space in the SSSSD (X_S, Y_S).

$$\begin{cases} X_S &= X_0 + \frac{(R-r)(X_M - X_0)}{R} \\ Y_S &= Y_0 + \frac{(R-r)(Y_M - Y_0)}{R} \end{cases} \tag{8.14}$$

where R is the distance between the target and MUST2 and $r = \frac{l}{\cos\theta_n}$.
Knowing this position in a square of 1 mm^2 we can determine the thickness thanks to energy loss table. Now we are able to reconstruct the (X, Y) thickness map as we can see in figure 8.15 where the z-axis is in micrometer. In this figure we can see large differences between the nominal thickness of 20$\pm$1.5 μm and the effective silicon thickness measured. The difference is about 25% from the nominal thickness, it varies between 15 to 25 μm. That is why without any specific treatment it is not possible to identify light particles.

Correction of the thickness

In order to take into account our map, we use the Bethe-Block formula connecting the energy loss ΔE and the total energy E of a particle:

$$\Delta E \approx a_1 e_{sssd} A Z^2 \frac{\ln(a_2 E)}{E} \tag{8.15}$$

This formula is more accurate when the thickness is small enough, or when $\Delta E << E$. We can correct the ΔE from the crossed thickness and normalized every event with a thickness of $e_{norm} = 20$ μm as follows:

$$\Delta E_{corr} = \frac{e_{norm}}{e_{sssd}} \Delta E_{sssd} \tag{8.16}$$

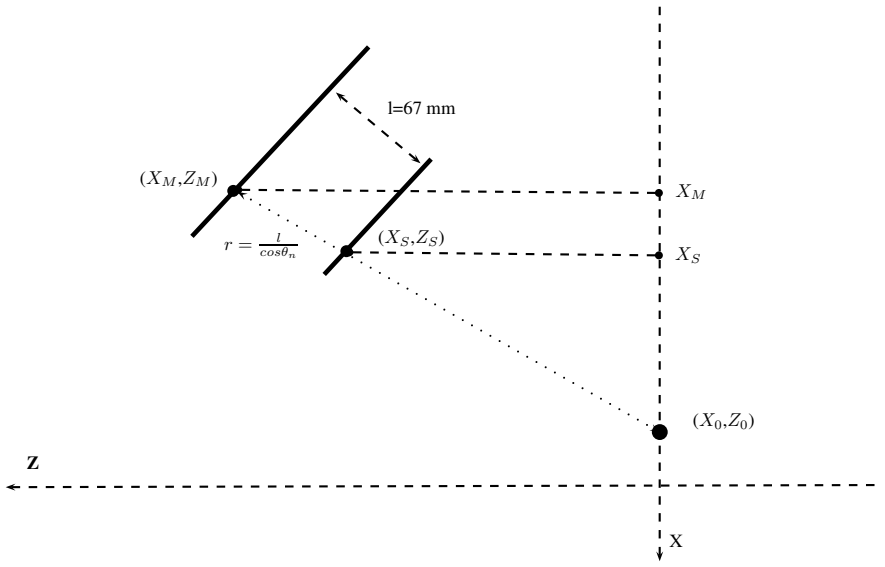

Figure 8.14: *Scheme of the thickness determination*

In the next section we will see how this correction enables us to identify correctly the particles in a $E - \Delta E$ identification and especially the ^{3}He from the α particles.

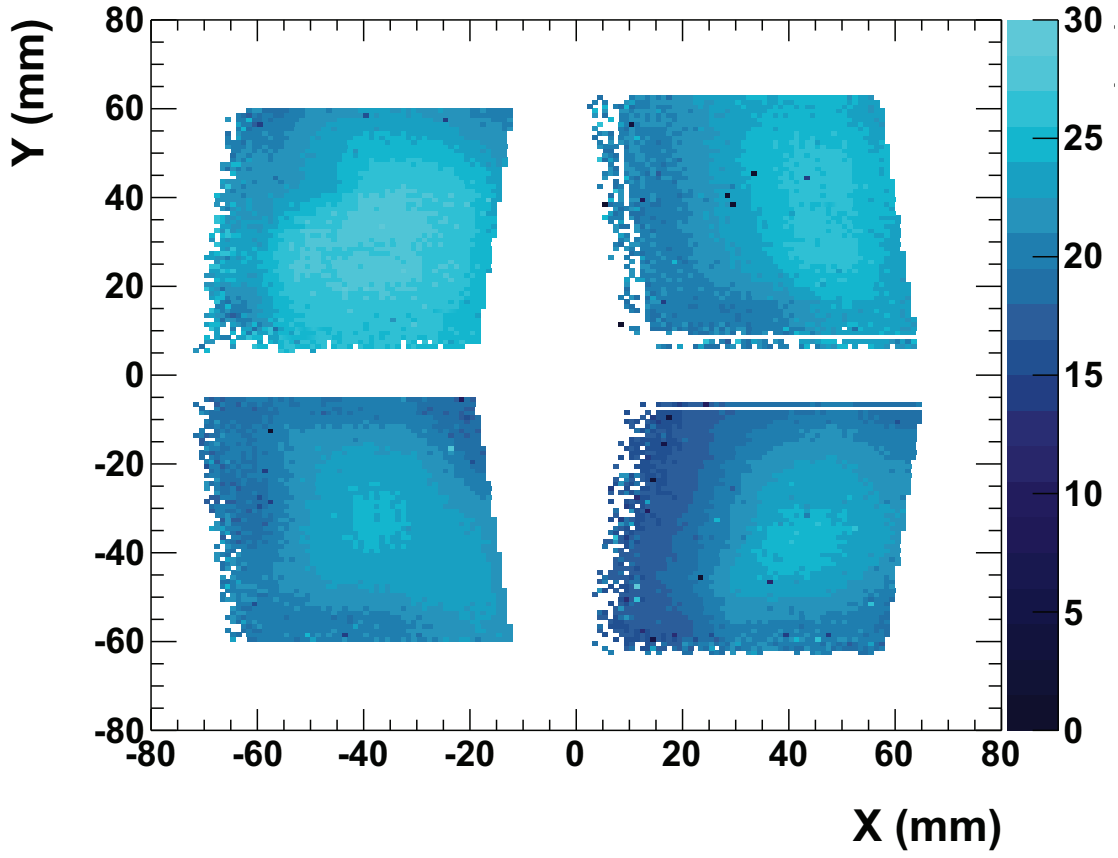

Figure 8.15: *Thickness of the SSSSD in the XY plan, the Z axis is in μm.*

8.5 Particle identification

The aim of this section is to present how we separate ^{3}He particles of energy below 22 MeV with respect to the other light particles such as ^{3}H and α particles. In order to select our ^{3}He of interest we present the method used in three steps:

- time of flight versus the energy deposited in the SSSSD: TOF-ΔE,
- time of flight versus the total energy: TOF-E ($E_{tot} = E_{SSSSD} + E_{DSSSD}$),
- and the ΔE-E identification.

8.5.1 TOF-ΔE identification

The spectrum of the energy deposited in the SSSSD versus the time of flight in MUST2 enables us to well separate the particles in Z, and especially when the energy in the 20 μm is high, as we can see in figure 8.16. The big spot around $\Delta E_{corr} \approx 0.5$ MeV corresponds to particles that cross the first stage of MUST2. But in this plot, we cannot separate between ^{3}He and α particle. This is the first identification step allowing us to select $Z = 2$ particles.

8.5.2 TOF-E identification

The time-of-flight identification allows us to separate particle by mass. Indeed the time of flight t for a distance d is:

$$t = \frac{d}{v} = \frac{d}{\beta c} \tag{8.17}$$

and we can write $\beta = \frac{pc}{E}$ where $pc = \sqrt{E^2 - m^2c^4}$ is the impulsion of the particle and E its total energy. It leads us to:

$$t = \frac{d}{c\sqrt{1 - \frac{m^2c^4}{E^2}}}. \tag{8.18}$$

For a same total energy E, an ^{3}He and a ^{3}H have the same time of flight. However in our case, we have the SSSSD in front of the MUST2 detectors in such a way that the particles

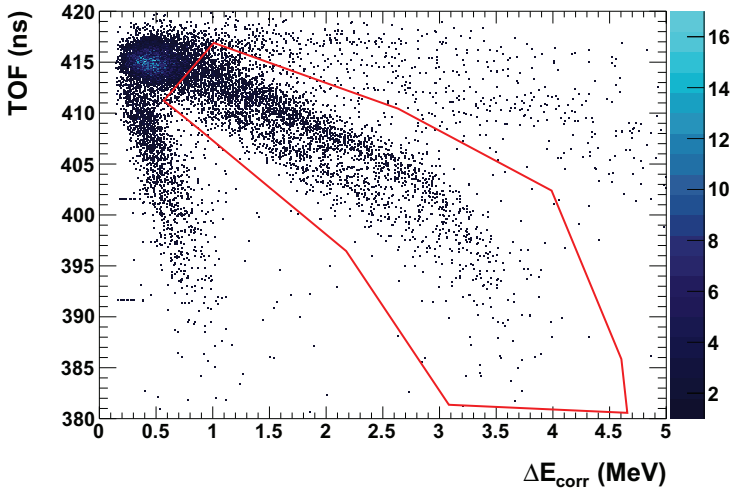

Figure 8.16: *Selecting $Z = 2$ particle within the red line in $TOF - \Delta E$ spectrum for detector 1.*

lose some energy before reaching the DSSSD array. Because of its charge, an ^{3}He loses more energy than a triton. As a matter of fact we need an ^{3}He with a kinetic energy of at least 4.1 MeV in order to cross the 20 μm silicon detector otherwise it will never reach the MUST2 detectors, while a triton needs only around 1 MeV to cross 20 μm of silicon. That is why if we plot the time of flight versus the total energy spectrum, we can separate an ^{3}He from a triton as we can see in figure 8.17. We note also that we observe two main lines corresponding to $Z = 2$ particles. But given the statistic of these lines, the first line cannot correspond to the ^{3}He line. In fact, we do not have a resolution good enough to separate ^{3}He from α particles and these two main lines correspond both to α particles with a different time of flight. In figure 8.18 we actually see three lines corresponding to $Z = 2$ particles with strange position correlation in the MUST2 detectors (figure 8.19). Only the blue one gives a homogeneous repartition in the MUST2 array, which is expected. It turns out that the other two lines (the red and the green one) come from reaction between the beam and the CATS detectors producing α particles. The time of flight is larger for CATS 1 which is farther away than CATS 2 from the target.
To confirm this hypothesis, we have simulated an α source at the position of the target, CATS1 and CATS2 respectively. We have analyzed all the simulations as if everything came from the target. In the TOF-E simulated spectrum (figure 8.20) we can see that the

time of flight is well reproduced. Moreover by selecting the different α lines and looking at the position in the MUST2 array we can see that we also well reproduce the impact position.
Therefore, it confirms that the other α lines correspond to the reaction between the beam and the CATS detectors. Since we can separate them in the TOF-E spectrum, it will not be an issue for the next. But it is interesting to note that the CATS detectors have to be not too close from the target for two reasons: fist of all, if the beam is too focused on a CATS detector, it may burn some central wires and secondly the reaction with the beam may produce α particles, which can be mixed with the particles produced from reaction with the target.

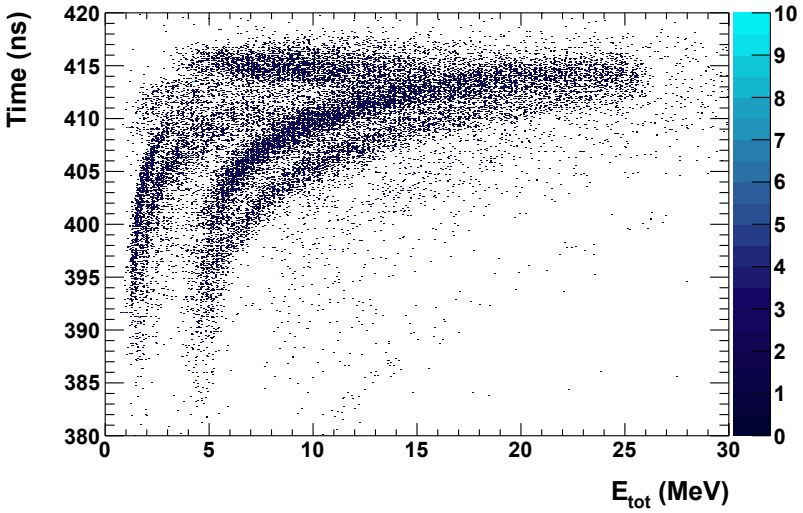

Figure 8.17: *Time of flight versus total energy*

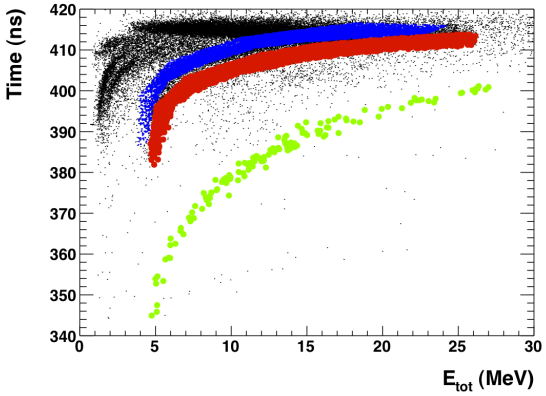

Figure 8.18: *Cut in time of flight spectrum for $Z = 2$ particle.*

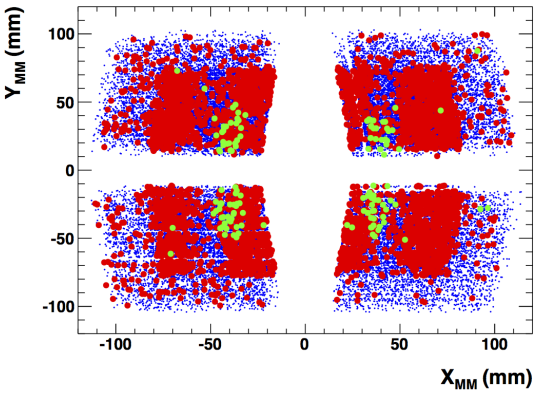

Figure 8.19: *Position in MUST2 telescope for the selected particles.*

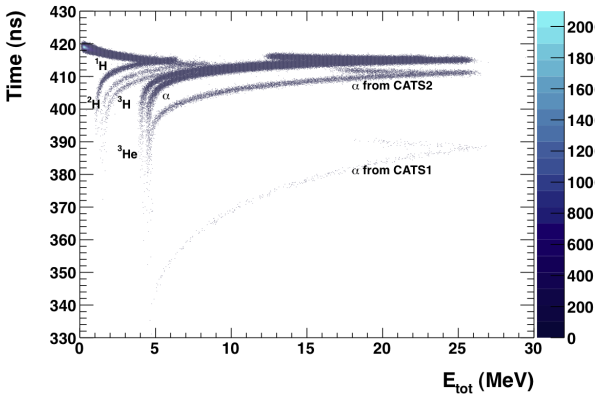

Figure 8.20: *Simulated time of flight spectrum for $Z = 1$ and $Z = 2$ particle.*

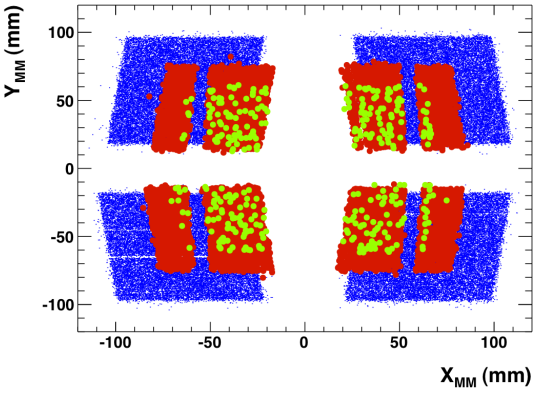

Figure 8.21: *Position in MUST2 telescope for the selected particles.*

8.5.3 E-ΔE identification

The $E - \Delta E$ is a powerful method to identify the particles. Indeed we have seen that:

$$\Delta E \approx a_1 e_{sssd} A Z^2 \frac{\ln(a_2 E)}{E}, \tag{8.19}$$

where a_1 and a_2 are constant and A and Z are the mass and the charge of the particle respectively. We can see that it is possible to separate all the particles with this method because we can separate in mass A and in charge Z. But because of the square, the separation is of course better for particle with different Z. Moreover, as we mentioned earlier the strong thickness inhomogeneities of the SSSD limits the separation power of this method. Indeed, as we can see in figure 8.22, we can only see the separation between $Z = 1$ and $Z = 2$ particles, we cannot separate ^{3}He from α particle. That is why the determination of the thickness map was so important. Indeed by replacing $\Delta E = E_{sssd}$ by $\Delta E_{corr} = \frac{e_{norm}}{e_{sssd}} E_{sssd}$ the separation in mass becomes possible and we can finally separate ^{3}He from α particles as we can see in figure 8.23.

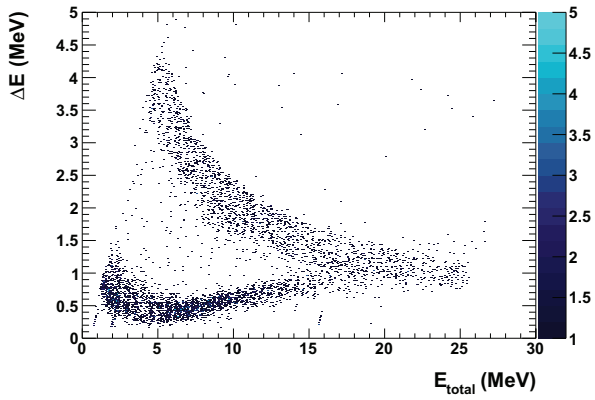

Figure 8.22: *$E-\Delta E$ spectrum before correction for detector 1*

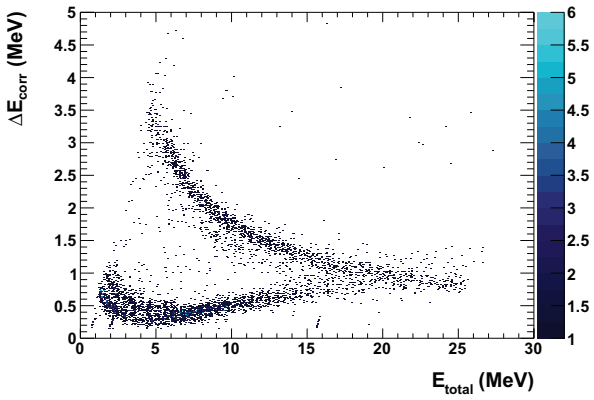

Figure 8.23: *$E-\Delta E$ spectrum after correction for detector 1*

8.6 Ionization chamber

In this experiment, the signal for the ionization chamber was digitized at a sampling rate of 40 MHz. The sample of each signal comprises 350 points. We can see a typical digitized signal in figure 8.24 when only one ion is detected during the digitization. Unfortunately, as we can see in figure 8.25, several ions can be detected during the range of the digitization, this is what we call pile-up. In most cases we have pile-up in our

signal. Then it is important to know which peak corresponds to our good event that has triggered. Actually when we look for all the events, the peak that corresponds to the good event arises always at the same position between the digitized point 180 and 200 as we can see in figure 8.26.
We want to get the amplitude of the peak we are interested in. Indeed the amplitude is mainly proportional to the atomic number Z of the nucleus. Thus we should be able to discriminate between different elements and mainly between Ga, Zn and Cu. To do so, the important thing is to well know the base line from which the peaks start to arise and also the position of the maximum. Finally the amplitude is just the difference between these two points.

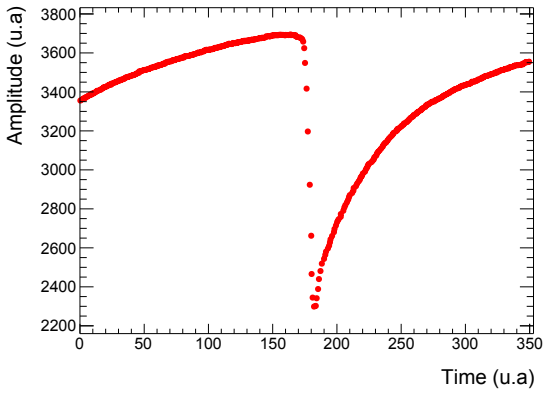

Figure 8.24: *Typical signal of the digitized ionisation chamber*

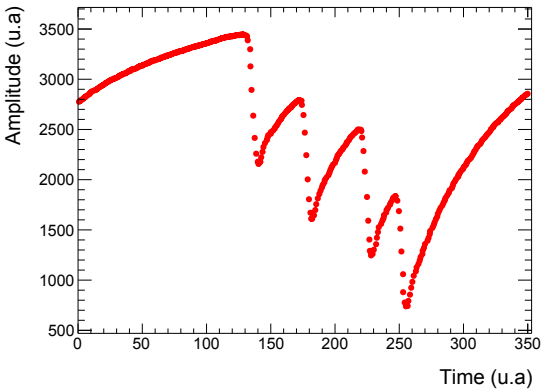

Figure 8.25: *Typical signal with pile-up indicating the passage of different ions during the time of digitization*

Concerning the resolution, if we look at figure 8.27, we see that we separate the different elements with difficulty concerning the amplitude in the ionization chamber. If we project element by element on the Y-axis to get the centroid of the distribution in the ionization chamber we can calibrate as a function of the atomic number Z:

$$\text{Amplitude} = \alpha Z + \beta \tag{8.20}$$

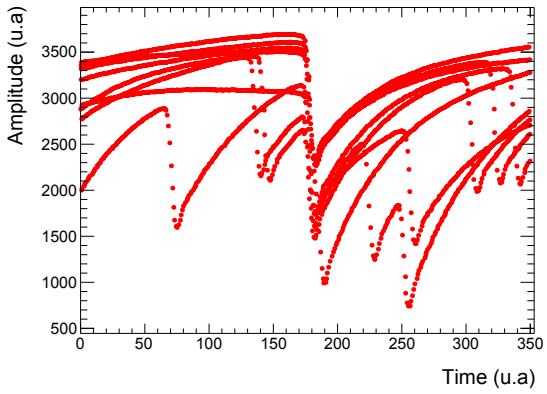

Figure 8.26: *Superposition of several signals. All the good peaks are situated between the point 180 and 200*

We can see the result of the fit in figure 8.28. We get the following parameters:

$$\begin{cases} \alpha = 73.0 \pm 3.5 \\ \beta = -887 \pm 109 \end{cases} \tag{8.21}$$

Knowing the errors on the parameters of the fit, we can estimate the amplitude in the ionization chamber for $Z = 29$. Then, by doing the following selection:

$$1030 < \text{Amplitude}(Z = 29) < 1400 \tag{8.22}$$

we should get the $Z = 29$ elements. Nevertheless the resolution is not good enough to get rid of all the contaminants. But this selection and the one in the time-of-flight to select the beam, enable us to get a clear excitation energy spectrum as we will see in the next section. In addition, we lose in efficiency when we do this selection. Then in order to clear the spectrum and well identify the populated states in ^{71}Cu we will use the chamber, however due to the lack of efficiency, no condition on the ionization chamber will be applied for the angular distribution.

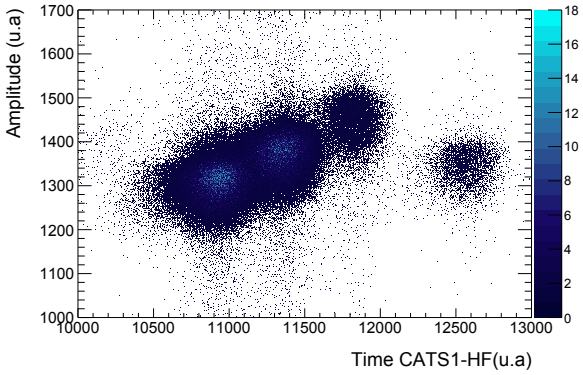

Figure 8.27: *Amplitude in the ionization chamber versus the TAC between CATS1 and the HF*

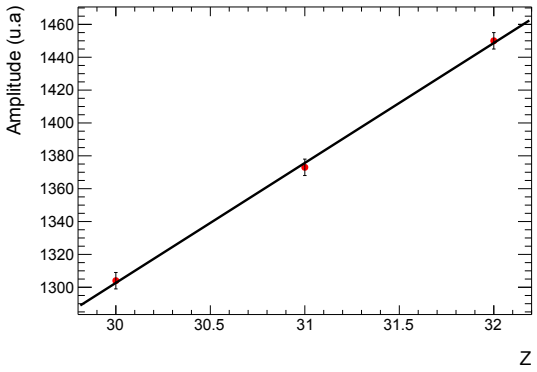

Figure 8.28: *Linear fit of the amplitude in the ionization chamber as a function of the atomic number Z*

8.7 Plastic

The plastic scintillator is normally used to measure the residual energy of the fragment of the reaction. However, as we can see in figure 8.29 most of the event are wrong and the plastic energy is not encoded. Only 11.4% of the events have a good plastic energy. So unfortunately, the plastic information was useless for the selection of the heavy fragment in this experiment.

8.8 Observables of interest

8.8.1 Excitation energy

We are here in inverse kinematics, but of course, the information we have access to is the same as in direct kinematics. Through the two-body kinematics we can reconstruct the excitation energy of the heavy fragment by measuring the kinetic energy and the angle of the light one. Concerning the excitation-energy spectrum it is similar as we have discussed in section 5.4. But one has to be careful when calculating the kinetic energy E_{lab} of the particle b. One has to properly calculate the energy loss in the dead layers of

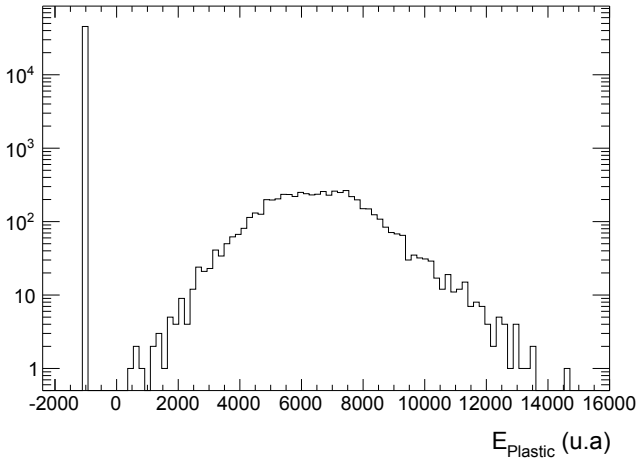

Figure 8.29: *Energy measured in the plastic. Most of the event are not encoded*

the detectors and in the target using energy loss tables. As it is shown in figure 8.30 the total kinetic energy is:

$$\begin{aligned} E_{lab} = & E_{DSSD}^{measured} + E_{DSSD}^{front}(E, \theta_n) \\ & + E_{SSSD}^{back}(E, \theta_n) + E_{SSSD}^{measured} + E_{SSSD}^{front}(E, \theta_n) \\ & + E_{target}(E, \theta_n). \end{aligned} \tag{8.23}$$

8.8.2 Angular distribution

Concerning the angular distribution the procedure is a little bit different since we have measured all the angles at the same time.
We want to calculate the angle in the center-of-mass frame. We know the beam energy $E_A = T_A + m_A$ and we measured the kinetic energy T_b of particule b ($E_b = T_b + m_b$). From this, we can calculate the angle θ_{CM} in the center of mass frame.

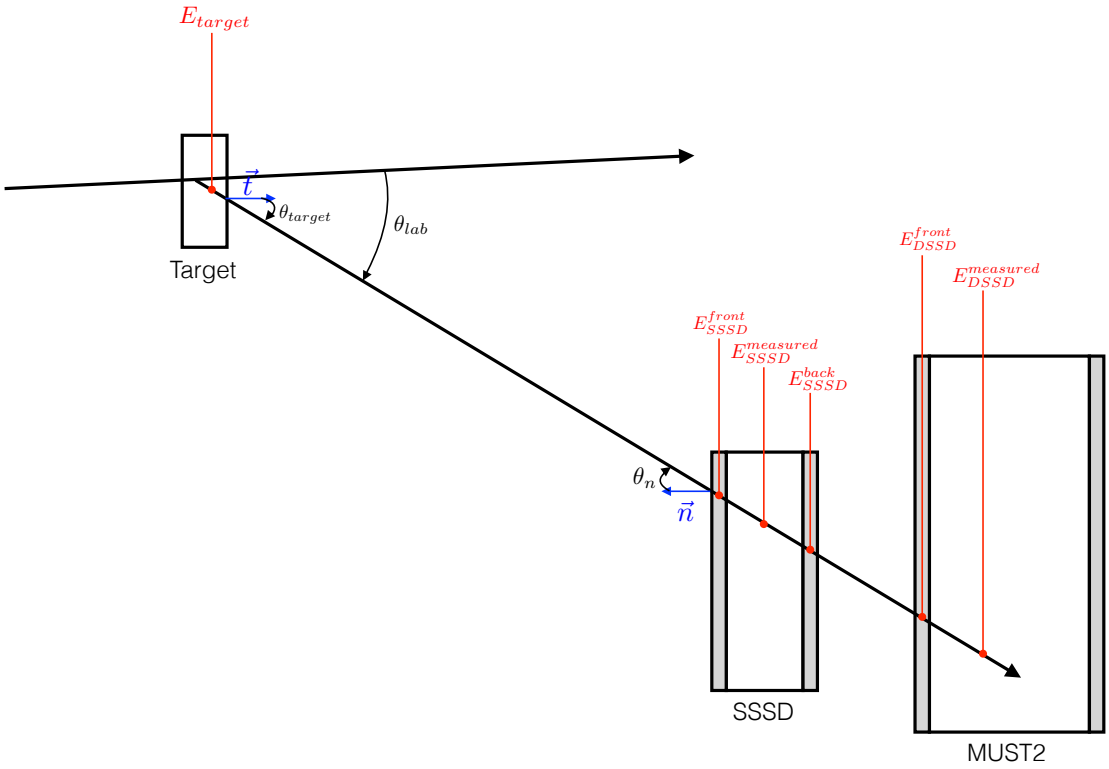

Figure 8.30: *Definition of parameter needed for the reconstruction of the excitation energy.* $\vec{t}$ *and* $\vec{n}$ *are respectively the normal to the target and the normal to the detector surface*

We remind that:

$$\begin{cases} E_b^* = \dfrac{s + m_b^2 - m_B^2}{2\sqrt{s}} \\ E_a^* = \dfrac{s + m_a^2 - m_A^2}{2\sqrt{s}} \end{cases} \tag{8.24}$$

where $s = (P_A + P_a)^2 = (P_B + P_b)^2$ is the first Mandelstam variable that is a Lorentz invariant. The energy in the center-of-mass frame E_i^* of the particle i is constant. And we have also $p_i^* = \sqrt{E_i^{*2} - m_i^2}$.

We construct the second Mandelstam variable $u = (P_3 - P_2)^2$

$$\begin{cases} u = (P_b - P_a)^2 = m_a^2 + m_b^2 - 2m_a E_b \\ u = (P_b^* - P_a^*)^2 = m_a^2 + m_b^2 - 2(E_a^* E_b^* - p_a^* p_b^* \cos\theta_{CM}) \end{cases} \tag{8.25}$$

Thus :

$$2p_a^* p_b^* \cos\theta_{CM} = u - (m_a^2 + m_b^2 - 2E_a^* E_b^*) \tag{8.26}$$

$$2p_a^* p_b^* \cos\theta_{CM} = u - (m_a^2 + m_b^2 - 2(E_a^* E_b^* + p_a^* p_b^*)) - 2p_a^* p_b^* \tag{8.27}$$

And thus:

$$\cos\theta_{CM} = \frac{u - u_0}{2p_a^* p_b^*} - 1, \tag{8.28}$$

with $u_0 = m_a^2 + m_b^2 - 2(E_a^* E_b^* + p_a^* p_b^*)$, or:

$$\theta_{CM} = \cos^{-1}\left(\frac{u - u_0}{2p_a^* p_b^*} - 1\right). \tag{8.29}$$

For each event, the angle in the center-of-mass frame θ_{CM} is calculated. Then we gate on a populated state in the excitation-energy spectrum E_{Bex} in order to obtain the angular distribution for this observed state in nucleus B. $N(\theta_{CM})$ is used to build the differential cross section that we want to compare with a reaction model in order to extract the transferred angular momentum thanks to the shape of the distribution. The experimental differential cross section is obtained as follows:

$$\frac{d\sigma}{d\Omega_{CM}} = \frac{N(\theta_{CM})}{\epsilon_{geo} N_{beam} N_{target} d\Omega_{CM}}. \tag{8.30}$$

- N_{target} is the deuteron number in the target as defined in equation 7.1.
- N_{beam} is the number of incident ion beam determined by the triggers CATS1 divided (or CATS2 divided). The difference given by the two CATS is less than 3%.
- $N(\theta_{CM})$ is the number of counts in the angular range $d\Omega_{CM}$, it contains the CATS efficiency.
- ϵ_{geo} is the MUST2 geometrical efficiency. $\epsilon_{geo} d\Omega_{CM}$ is evaluated thanks to a simulation using a flat differential cross section in the center-of-mass frame for the reaction of interest.

9 Results

Contents

THIS chapter presents the experimental results for the studied reactions: the elastic scattering ^{72}Zn(d,d)^{72}Zn and the two pick-up transfer reactions (d,^{3}He) and (d,t). We shall see the excitation-energy spectrum together with the experimental differential cross sections. In order to extract the information about the nuclear structure of our nuclei of interest we will use the same reaction model as the one explained in the first

part and the same parametrization for the optical potentials, which means that both nuclei are studied in the same coherent way. Thus comparison of the centroid of the strength distribution will be possible.

9.1 Elastic scattering

Two MUST2 detectors were placed at ninety degrees that enabled us to detect the deuterons coming from the elastic scattering. This reaction is an important benchmark for the validity of the optical potential and also to check the normalization procedure. Moreover we were able to quantify the amount of protons present in the target thanks to the elastic scattering between the beam and the protons. The total quantity of deuterons is determined as we saw in equation 7.1.

9.1.1 Target contamination

It is important for the normalization procedure to quantify the amounts of protons in the target. To determine this amount, we used elastic scattering. Indeed by gating on the protons in the time-of-flight spectrum we can see in figure 9.1 an excess of statistics corresponding to the kinematics of the elastic scattering between the beam and protons present in the target. In figure 9.2 we can see the associated excitation-energy spectrum. By looking at the angular distribution of the scattered protons and compare it to the calculation, as we can see in figure 9.3, we have determined the fraction of protons to be $f_p \approx 2\%$. For the calculation we have used the parametrization given by Menet *et al.* [71], this optical potential covers the range from ^{12}C to ^{208}Pb for 30-60-MeV protons. Even though this contamination is very low we take it into account for the analysis.

9.1.2 Excitation-energy spectrum for (d,d')

By selecting the beam as we saw in figure 8.1 and by selecting the deuterons in the time-of-flight versus the energy spectrum as visible in figure 9.4, we can reconstruct the

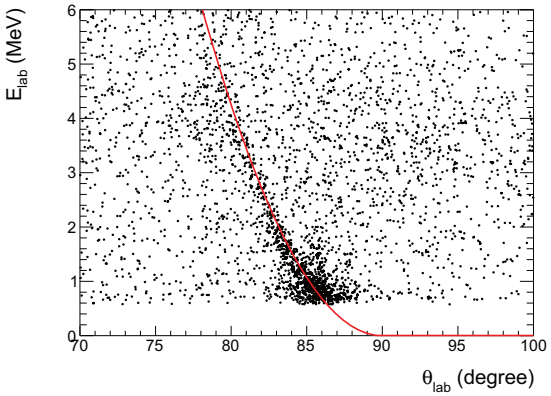

Figure 9.1: *Kinematic line for ^{72}Zn(p,p) reaction with in red the theoretical kinematic line*

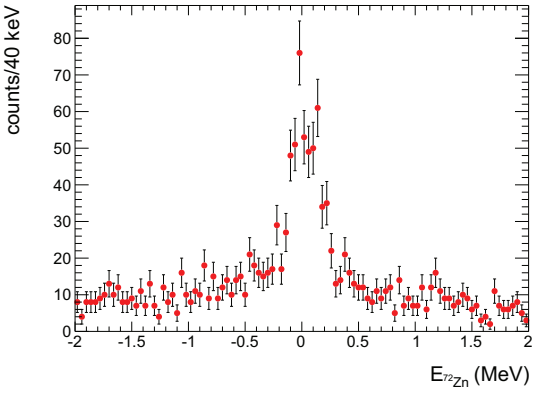

Figure 9.2: *Excitation energy spectrum of ^{72}Zn reconstructed with the ^{72}Zn(p,p) kinematics with a resolution σ = 165(9) keV*

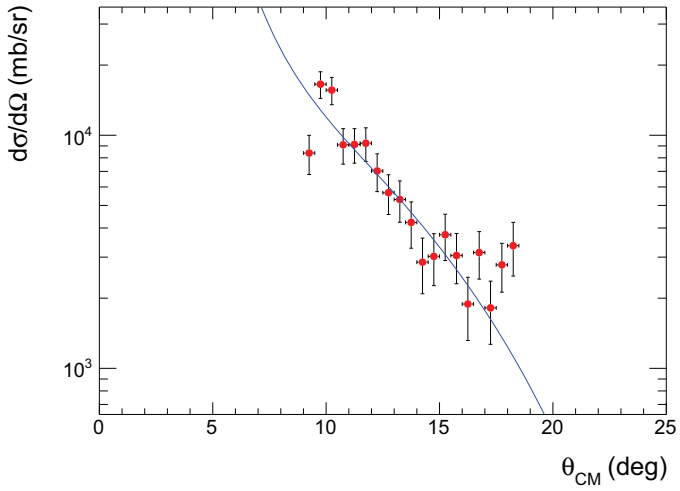

Figure 9.3: *Differential cross-section of the protons elastic scattering*

excitation-energy spectrum of the ^{72}Zn nucleus. Moreover, the kinematic line in figure 9.5 is clearly visible for this reaction. Indeed the excess of statistics is well reproduced by the theoretical kinematic line corresponding to the ^{72}Zn(d,d)^{72}Zn elastic scattering.

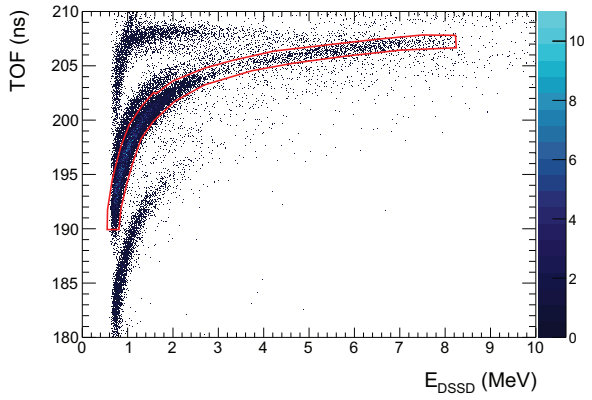

Figure 9.4: *Time-of-flight versus the energy of light particles in T5-6. The red cut corresponds to the selected deuterons*

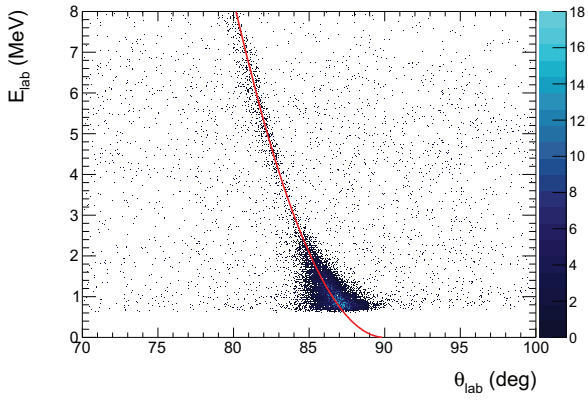

Figure 9.5: *Kinematic line for ^{72}Zn(d,d) reaction with in red the theoretical kinematic line*

Figure 9.6 shows the excitation-energy spectrum corresponding to the ^{72}Zn nucleus. The elastic peak was fitted using a Gaussian function. The position of the centroid and the experimental width are $\mu = -12.3 \pm 8.3$ keV and $\sigma = 203$ keV respectively, that is the expected resolution from the simulation. One can clearly realize the importance of the beam reconstruction using the CATS detectors in figure 9.7. Indeed, in this plot the excitation-energy spectrum is calculated assuming no beam reconstruction. That means that event by event we suppose that the beam hits the target at the position $(0, 0, 0)$. By doing this approximation, the angle in the laboratory frame is wrong and it deteriorates badly the energy resolution that is $\sigma = 389$ keV.

9.1.3 The angular distribution

The angular distribution is obtained by gating on the elastic peak using the following condition: $-0.8 \leq E_{^{72}Zn} \leq 0.8$ MeV on top of the selection of the beam and the gate on the deuterons. The efficiency of the detection setup is determined thanks to the simulation of the elastic scatering using a flat distribution in the center-of-mass frame. After normalization, the final cross section is obtained in figure 9.8. For the calculation we

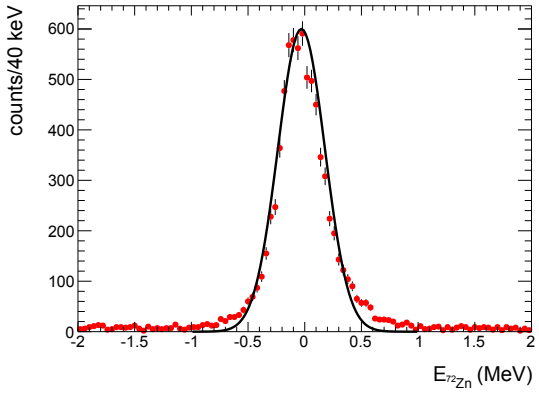

Figure 9.6: *Excitation-energy spectrum of* ^{72}Zn. $\sigma = 203(3)$ *keV*

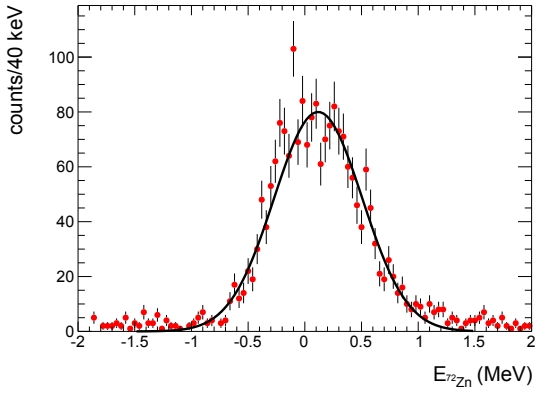

Figure 9.7: *Excitation-energy spectrum of* ^{72}Zn *without any beam reconstruction on the target.* $\sigma = 389(6)$ *keV*

used the Daenick relativistic optical potential [54]. We have a good agreement between the experimental cross section and the calculated one, giving us confidence about this potential for the entrance channel to calculate the transfer cross section. The values used for the optical potential are listed in table 9.2.

9.2 Transfer reactions

The (d,^{3}He) and (d,t) transfer reactions are studied using the four MUST2 telescopes placed at forward angles plus the four SSSSD detectors used for the identification of the light charged particles. As explained in the next section the spectra are obtained using the different following selections:

1. Gate on the incident beam ^{72}Zn,
2. Gate $\Delta E - \text{TOF}$ on $Z = 2$ or $Z = 1$ particles,
3. Gate $E - \text{TOF}$,
4. Gate $E - \Delta E$ on the ^{3}He or the triton,
5. Gate on the ionization chamber on the $Z = 29$ as specified in equation 8.22.

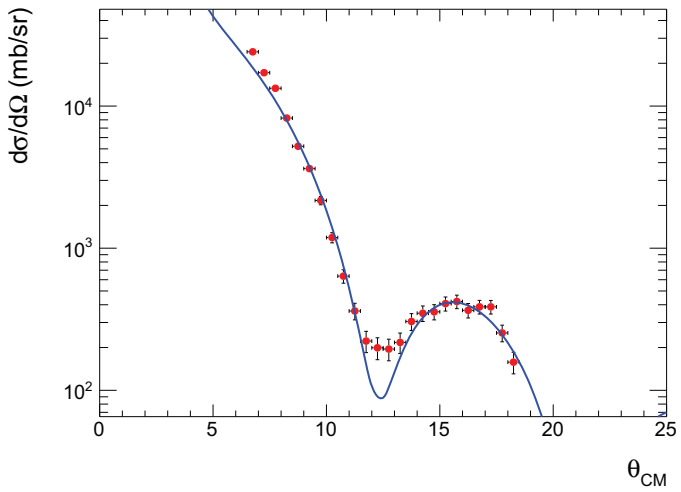

Figure 9.8: *Differential cross section of the elastic scattering after correction for the efficiency and normalization (red points), compared with a calculation using the relativistic Daehnick optical potential (blue line)*

9.2.1 The one-proton transfer reaction (d,^{3}He)

Excitation energy spectrum

After applying the gates 1-4 and except 5, we can see the kinematic plot for the ^{72}Zn(d,^{3}He)^{71}Cu reaction in figure 9.9 and the associated excitation-energy spectrum of the ^{71}Cu nucleus in figure 9.10. In order to clean the spectrum and to be sure we select only our reaction of interest we apply the gate 5. By doing this selection we have the excitation energy visible in figure 9.11. By applying this condition, we clearly lose in efficiency especially at high excitation energy. Then in order to define the peaks and determine their position in energy we keep the condition on the ionization chamber. But due to the lack of efficiency we remove this condition 5 to construct the angular distributions. This choice is legitimate because the carbon background is very low as we can see in blue in figure 9.11.

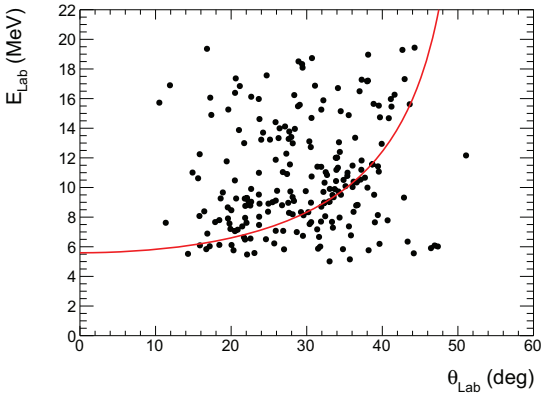

Figure 9.9: *Kinematic plot for the $^{72}Zn(d,^{3}He)^{71}Cu$ transfer reaction*

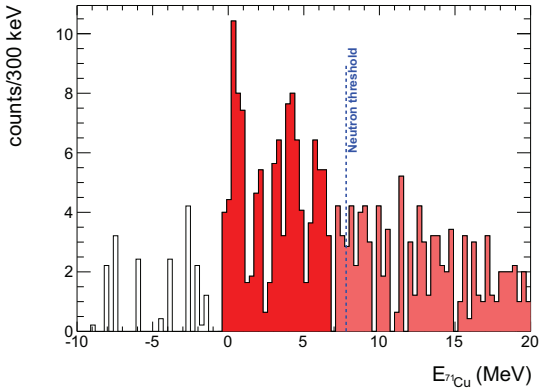

Figure 9.10: *Excitation-energy spectrum of ^{71}Cu without any condition on the ionization chamber*

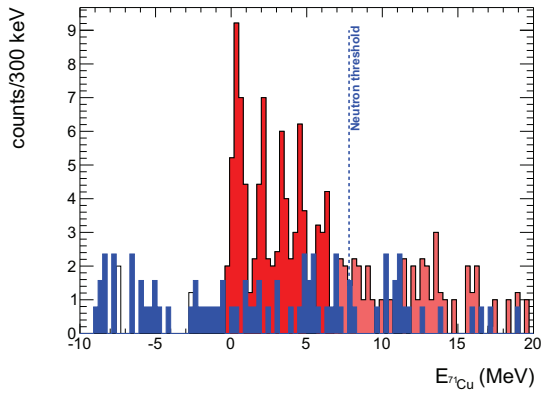

Figure 9.11: *Excitation-energy spectrum of ^{71}Cu with a condition 5 (in red). In blue is the corresponding normalized carbon spectrum*

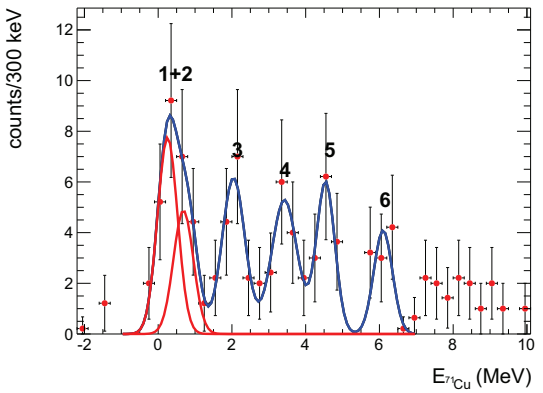

Figure 9.12: *Multiple Gaussian fit of the excitation-energy spectrum*

In ^{71}Cu, we know that there are the $3/2^-$ ground state and also a $5/2^-$ excited state at 534 keV. We will populate both states even though we do not expect to populate substantialy the $5/2^-$ state with this pick-up reaction. Moreover, we also know from the simulation that we do not have the energy resolution good enough to separate these two peaks. In addition we see in figure 9.12 that the first peak is broader than the others. For the fit

we assume two states in the first peak separated by 534 keV. The position of the peaks in blue are listed in table 9.1 as the resolution. Thus, we see that we have populated six different states in this reaction within our detection limit. The average resolution is about 306 keV and worst than for the elastic scattering because here we have the SSSSD that degrade the final resolution. In order to get the spectroscopic information for these different states we will look at the angular distributions.

States	Energy (MeV)	σ (keV)	$L(J^\pi)$	C^2S	χ^2/NDF
1	0.29(19)	390(51)	1 ($3/2^-$)	0.80(15)	2.23/3
2			3 ($5/2^-$)	1.40(63)	2.23/3
3	2.04(15)	324(68)	3 ($7/2^-$)	1.38(18)	0.613/4
4	3.42(20)	333(61)	3 ($7/2^-$)	1.49(34)	4.13/5
5	4.54(17)	280(36)	3 ($7/2^-$)	3.69(62)	2.94/3
6	6.10(18)	290(45)	0 ($1/2^+$)+2 ($3/2^+$)	0.4(1) and 3.0(5)	6.2/3

Table 9.1: *Position in energy of the different populated states in ^{71}Cu, the resolution σ, the associated angular momentum L, the proposed spin-parity J^π and the spectroscopic factor C^2S*

Angular distributions

The angular distributions for the different populated peaks are obtained by applying the same gates 1-4 plus a gate on the excitation energy-spectrum corresponding to the peak we want to look at its differential cross section. Figures from 9.14 to 9.19 correspond to the differential cross section for the populated peaks in ^{71}Cu. In table 9.1 are listed the different states and the determined transferred angular momenta with their associated spectroscopic factors. The latter is determined through a χ^2 minimization between the experimental points and the calculated finite-range cross section with DWUCK5. The results shown in the figures correspond to the distributions that minimize the χ^2. For the calculation, we have used the Perey and Peray optical potential for the out-going channel [55]. The value of all the parameters are listed in table 9.2. Finally, as in the ^{69}Cu case, we have used the Brida *et al.* potential [56] to describe the overlap between the deuteron and the ^{3}He.

	V	W	W_D	r_c	r_0	a_0	r_i	a_i	V_{so}	λ
d	72.8	6.30	8.17	1.3	1.17	0.81	1.29	0.88	2.5	
^{3}He	150.1	28.47	0	1.3	1.2	0.72	1.4	0.88	2.5	
p	adj			1.25	1.25	0.65				25

Table 9.2: *Global optical potential for* ^{71}Cu

First of all, for the first peak that is wider as mentioned earlier, if we look at the angular distribution we clearly see that we need an $L = 1$ plus $L = 3$ contribution to reproduce correctly the data. This confirms that we have populated the $3/2^-$ ground state as the $5/2^-$ excited state at 534 keV. Even though we do not have the energy resolution good enough to separate them we can identify clearly their different contributions through the angular distribution.
Moreover, we note that in the range $1.3 < E_{^{71}Cu} < 5.3$ MeV the three populated peaks are compatible with an $L = 3$ angular momentum. In order to increase the statistics to get the differential cross-section, we can see in figure 9.18 the angular distribution for the three peaks. If we assume that these three peaks at 2.04 MeV, 3.42 MeV and 4.54 MeV respectively have an angular momentum $L = 3$ and assuming that they correspond to the proton-hole state $f_{7/2}^{-1}$ (the assignment $5/2^-$ can be excluded because we do not expect to populate $5/2^-$ state in pick-up reaction and especially at high excitation energy) then the centroid of the measured strength is:

$$E(f_{7/2}^{-1}) = \frac{\sum C^2S(7/2^-)E(7/2^-)}{\sum C^2S(7/2^-)}. \tag{9.1}$$

In our case we get $E(f_{7/2}^{-1}) = 3.76$ MeV with $\sum C^2S(7/2^-) = 6.56 \pm 1.14 = 82\%$.
Now in figure 9.18 we see the angular distribution for these three states fitted with an $L = 3$ angular distribution simulating a single state a 3.76 MeV. The associated spectroscopic factor after the minimization is $C^2S = 6.9 \pm 0.8 = 86\%$ that is compatible with the previous result.
Finally, the angular distribution of the peak at 6.10 MeV (figure 9.19) is more compatible with a doublet between an $L = 0$ and $L = 2$ distribution even though the data are not well fitted with such a distribution ($\chi^2/NDF = 6.2/4$). This peak might correspond to the inner *sd* states of the nucleus.
As the extraction of the spectroscopic factor is model-dependent it is interesting to discuss the effect on its value by changing some of the ill-defined parameters in the DWBA

calculation. Of course we will not change all the parameters especially there is no need to change the parameters in the entrance channel as we saw earlier that the global potential reproduced very well the elastic scattering. The interesting parameters to vary are the radius r_0 and the diffuseness a_0 of the proton in the transfer channel that are two of the Woods-Saxon parameters of the potential between the proton and the ^{71}Cu nucleus. The depth of the potential is automatically adjusted during the calculation to reproduce the binding energy. The typical values of these two parameters are $r_0 = 1.25$ fm and $a_0 = 0.65$ fm but it is worth to change those values to see the effect on the extracted spectroscopic factor. We have changed the radius r_0 from 1.20 fm to 1.30 fm and the diffuseness a_0 from 0.60 fm to 0.70 fm and for each couple (r_0, a_0) we have extracted the measured $C^2S(f_{7/2}^{-1})$ by looking at the angular distribution of the three states at the same time. We can see the result of this work in figure 9.13. We can note that we get a variation of 38% between the central values ($r_0 = 1.25$ fm, $a_0 = 0.65$ fm) and the two extremities ($r_0 = 1.20$ fm, $a_0 = 0.60$ fm) and ($r_0 = 1.30$ fm, $a_0 = 0.70$ fm). So depending on the choice of the couple we could have measured 50% of the proton-hole strength or all of the strength. Although we are aware of this effect we stay with the values ($r_0 = 1.25$ fm, $a_0 = 0.65$ fm) for both isotopes. Indeed the effect of such a variation is the same for ^{69}Cu and ^{71}Cu and because we want to study them in a coherent way and also to be consistent with majority of literatures, the most important thing is to use the same global parameters in both analyses.

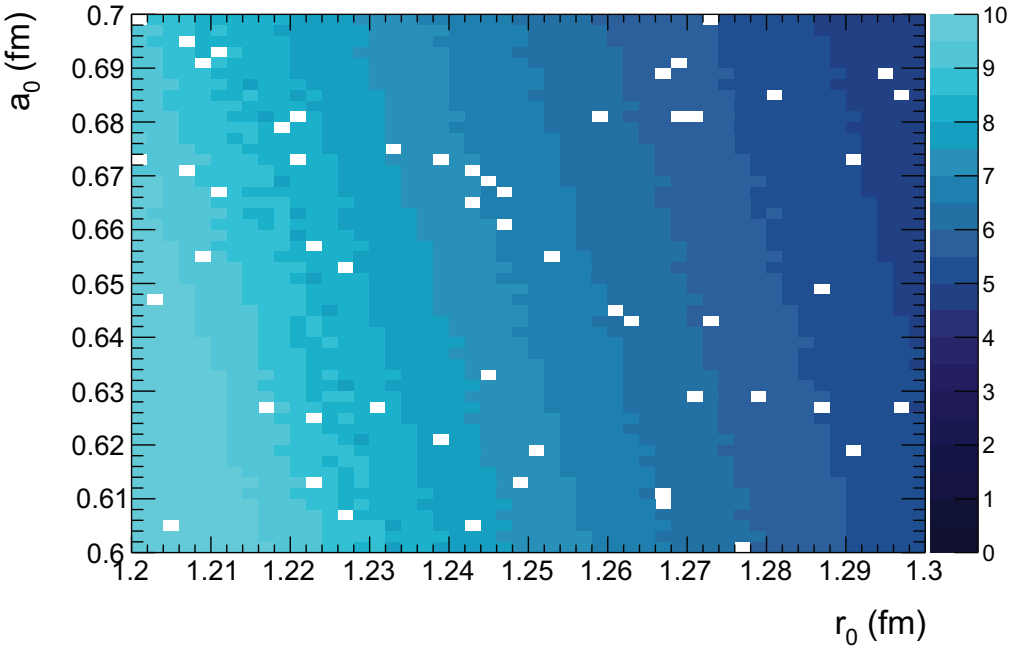

Figure 9.13: *Evolution of the spectroscopic factor C^2S in the z-axis as a function of the radius r_0 and the diffuseness a_0 of the proton potential in the transfer channel*

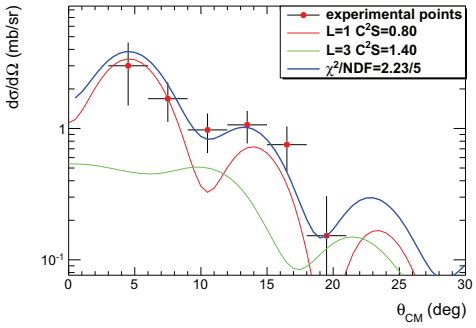

Figure 9.14: *Differential cross-section for $-0.5 < E_{^{71}Cu} < 1.3$ MeV (peak 1+2)*

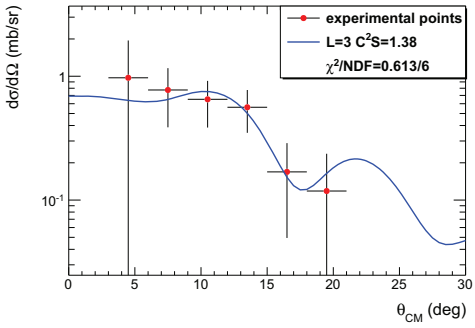

Figure 9.15: *Differential cross-section for $1.3 < E_{^{71}Cu} < 2.5$ MeV (peak 3)*

Effect on the C^2S using different potentials in the out-going channel

In order to see the effect on the spectroscopic factors we have used two different optical potential in the out-going channel. The first one, as we saw just before is the parametriza-

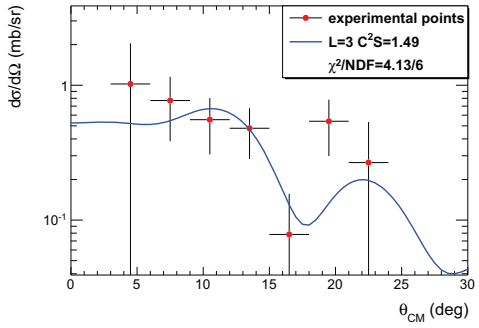

Figure 9.16: *Differential cross-section for* $2.5 < E_{^{71}Cu} < 3.7$ *MeV (peak 4)*

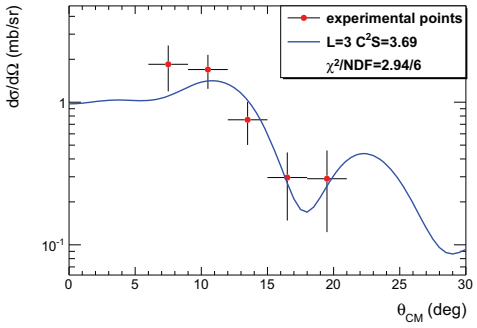

Figure 9.17: *Differential cross-section for* $3.7 < E_{^{71}Cu} < 5.3$ *MeV (peak 5)*

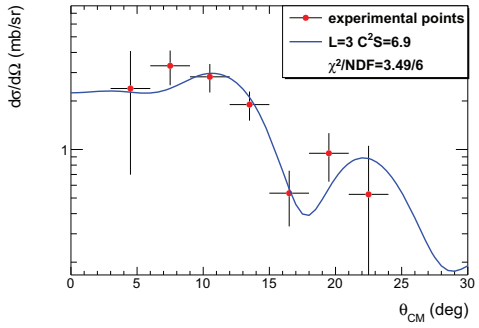

Figure 9.18: *Differential cross-section for* $1.3 < E_{^{71}Cu} < 5.3$ *MeV (peak 3+4+5)*

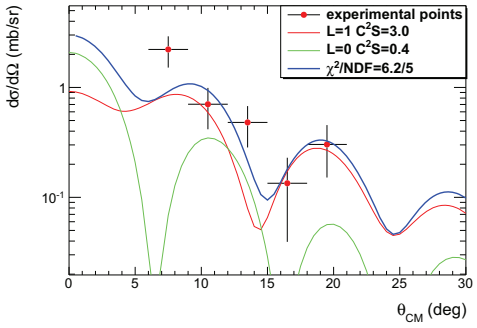

Figure 9.19: *Differential cross-section for* $5.1 < E_{^{71}Cu} < 6.8$ *MeV (peak 6)*

tion of Perey and Perey [55], and the second one is the global optical potential of Pang *et al.* [72]. We can see in figure 9.20 the result for both parametrization and in table 9.3 the result for the spectroscopic factor C^2S with the associated χ^2. One can see that the values for the spectroscopic factor differ by only 10% and are completely compatible within the errors. Finally, because the χ^2 is better in the case of Perey and Perey, this potential was chosen for the analysis of both isotopes.

Parametrization	C^2S	χ^2/NDF
Perey and Perey [55]	6.9(8)	6.8/5
Pang [72]	6.1(7)	4.3/5

Table 9.3: *Value of spectroscopic factor obtained using two different parametrizations*

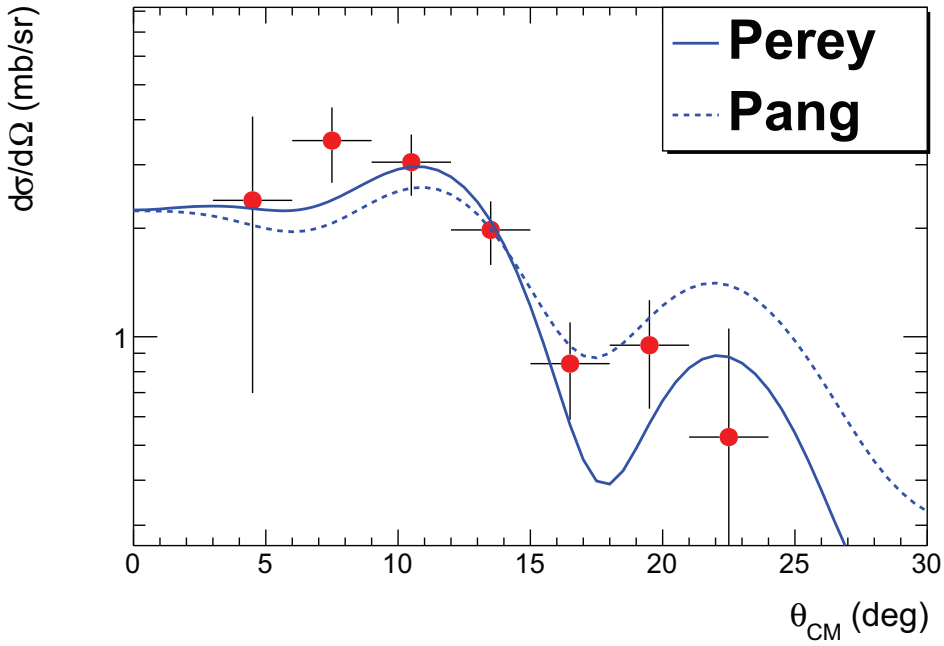

Figure 9.20: *Minimization of the $L = 3$ angular distribution using the Perey and Perey parametrization (blue line) and the Pang one (dashed line)*

9.2.2 The one-neutron transfer reaction (d,t)

Excitation-energy spectrum

In order to study the neutron-removal (d,t) reaction we have applied the same gates 1-4 as before but we have selected the tritons instead of the ^{3}He.
By doing so, we can see in figure 9.21 the kinematic line for the reaction where the red line corresponds to the transfer reaction when the ^{71}Zn nucleus is populated in its ground state. In figure 9.22 we have reconstructed the excitation-energy spectrum of ^{71}Zn and we see that we have populated two states. The energy of these two states are listed in table 9.4 as the energy resolution for each peak. The energy resolution of peak 1 suggests that two or several levels are present in this peak.

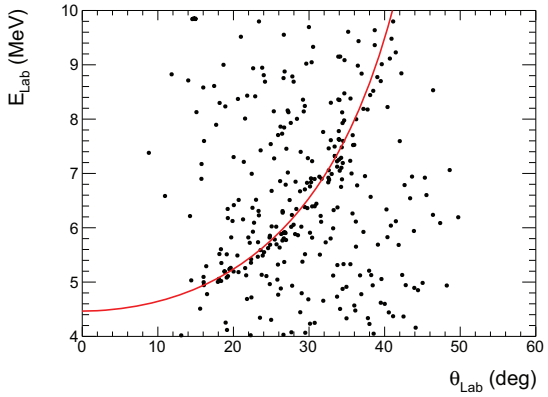

Figure 9.21: *Kinematic plot for the $^{72}Zn(d,t)^{71}Zn$ transfer reaction*

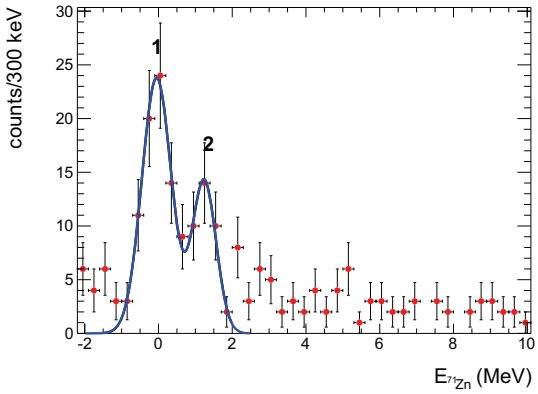

Figure 9.22: *Excitation-energy spectrum of ^{71}Zn*

States	Energy(MeV)	σ (keV)	$L(J^\pi)$	C^2S	χ^2/NDF
1	−0.03(07)	444(69)	1 $(1/2^-)$	0.84(15)	2.53/4
			2 $(5/2^+)$	0.70(13)	
2	1.27(09)	299(57)	2 $(5/2^+)$	0.51(10)	1.94/4

Table 9.4: *Position in energy of the different populated states in ^{71}Zn with the associated angular momentum L, proposed spin-parity (J^π) and spectroscopic factor C^2S*

Angular distributions

Once more, the angular distributions are given by applying the same gates 1-4 as before and by doing a selection on the excitation-energy spectrum. The results for the two populated peaks are plotted in figures 9.23 and 9.24. In these two figures, the experimental angular distribution is fitted to determine the angular momentum and the spectroscopic factor. The parameters of the global optical potential used for the finite-range calculation using the DWUCK5 code are listed in table 9.5. We show here the calculated distributions for a minimized χ^2 and the final results are given in table 9.4.
The low-lying states in ^{71}Zn have been well established in the work of D. Von Ehrenstein and J. P. Schiffer [73] from the ^{70}Zn(d,p)^{71}Zn reaction. From this work, it is known that the ground state is a $1/2^-$ state, a $9/2^+$ state lies at 157 keV and a $5/2^+$ state lies at 285 keV. If we assume in our work that only the $1/2^-$ state is populated in the first peak then the result of the χ^2 minimization for a $p_{1/2}$ distribution gives a spectroscopic

factor $C^2S(p_{1/2}) = 2.77 \pm 0.36$. This value is too large to be consistent with a $p_{1/2}$ state. Moreover D. Von Ehrenstein and J. P. Schiffer [73] measured for the ground state $C^2S(p_{1/2}) = 0.95$. In order to satisfy the sum rule we should have a spectroscopic factor around 1 but not higher. With this argument we clearly have another populated state in this peak, which we do not resolve in energy. To determine the different populated states thanks to the shape of the angular distribution we have summed two or three different distributions to fit the data. The results are listed in table 9.6. We see in this table that we obtain the best result for a doublet of states $L = 1$ plus $L = 2$. It seems that we do not populate any $g_{9/2}$ particle state in the ^{71}Zn nucleus. Concerning the state at 1.27 MeV, the angular distribution clearly shows an $L = 2$ state with $C^2S = 0.51$. From D. Von Ehrenstein *et al.*, a $L = 2$ state at 1.26 MeV was observed with a measured spectroscopic factor of $C^2S = 0.06$, which is in fair agreement with our measurement since we did the complementary reaction.

	V	W	W_D	r_c	r_0	a_0	r_i	a_i	V_{so}
d	72.8	6.30	8.17	1.3	1.17	0.81	1.29	0.88	2.5
t	153.07	37.96	0	1.3	1.2	0.72	1.4	0.84	2.5

Table 9.5: *Global optical potential for ^{71}Zn*

L	χ^2/NDF	C^2S
1	3.05/4	$C^2S(p_{1/2}) = 2.77$
1+2	2.53/3	$C^2S(p_{1/2}) = 0.84$
		$C^2S(d_{5/2}) = 0.70$
1+4	4.22/3	$C^2S(p_{1/2}) = 1.21$
		$C^2S(g_{9/2}) = 0.90$
1+2+4	3.18/2	$C^2S(p_{1/2}) = 0.50$
		$C^2S(g_{9/2}) = 0.43$
		$C^2S(d_{5/2}) = 0.54$

Table 9.6: *Minimization with different angular distributions for the first populated peak in ^{71}Zn*

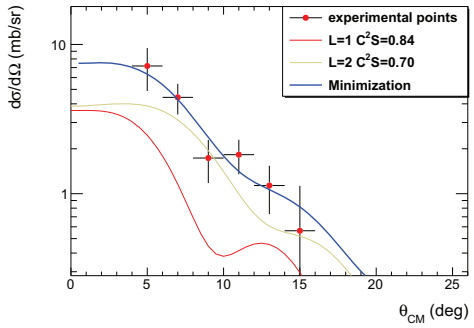

Figure 9.23: *Differential cross-section for* $-1.0 < E_{^{71}Zn} < 0.7$ *MeV (peak 1 from Fig. 9.22)*

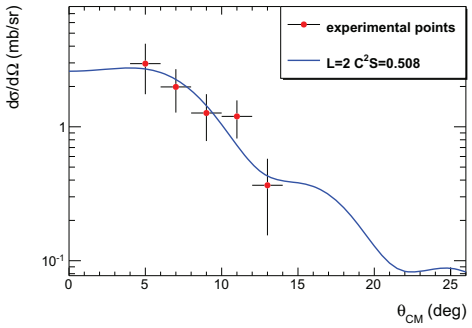

Figure 9.24: *Differential cross-section for* $0.7 < E_{^{71}Zn} < 1.7$ *MeV (peak 2 from Fig. 9.22)*

Part IV

Interpretation and discussion

10

Results and discussion

Contents

THIS chapter will present the theoretical calculations compared with the experimental results. We will explain the details of the calculations performed and we will discuss the results about the ^{69}Cu and ^{71}Cu nuclei.

10.1 Details of present shell-model calculations

10.1.1 Valence space and interaction

The shell-model calculation was done by the Strasbourg group and in particular by Kamila Sieja using the ANTOINE code [74, 75]. In our case, the valence space used, named hereafter $fpgd$, contains $1f_{7/2}$, $2p_{3/2}$, $1f_{5/2}$ and $2p_{1/2}$ orbits for protons and $2p_{3/2}$, $1f_{5/2}$, $2p_{1/2}$, $1g_{9/2}$ and $2d_{5/2}$ orbits for neutrons. This corresponds to a ^{48}Ca core. This valence space is huge and allows proton excitations from the $1f_{7/2}$ orbital. The calculations are very time consuming. For example in the case of ^{71}Cu which has 9 protons and 12 neutrons in the valence space, the total dimension of the configuration space is given by:

$$D = \binom{20}{9}\binom{28}{12} \approx 5.11\ 10^{12}, \tag{10.1}$$

which is beyond current computing possibilities. Therefore, the calculations have been truncated to $8p-8h$ excitation across $Z = 28$ and $N = 40$ gaps. Lanczos strength function method with 60 iterations has been used to obtain spectroscopic factor distribution.
The interaction used for the calculation is the LNPS interaction from previous work [76] with minor revisions that includes modifications of the pairing interaction and of the relative position of the single-particle energies to reproduce well the evolution of the $Z = 28$ shell gap between $N = 40$ and $N = 50$ as we can see in figure 10.1. One can see the good agreement between experimental ΔS_p and the calculated gap between $N = 40 - 44$. For $N > 44$, the experimental data are estimated because the measurement are not yet available. From the calculation, one can see that there is a maximum of correlations at $N = 46$.

10.1.2 Results for ^{69}Cu

We have populated eight states in ^{69}Cu. Our results are in agreement for the five first states with previous work [32, 34]. The main difference is the $L = 3$ state at 1.23 MeV. In the previous work, the obtained spectroscopic factor was high leading to the conclusion that two states populated in this peak were separated by less than 15 keV. However, from

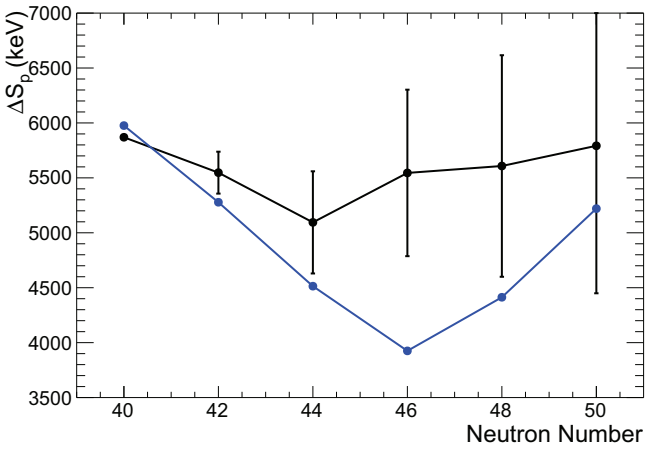

Figure 10.1: *Comparison between calculated gap in blue and experimental ΔS_p in black as a function of neutron number. It is an estimated ΔS_p for $N = 46 - 50$ since the mass are not measured yet*

our work there is no evidence of such a doublet. Indeed, the obtained resolution for this state was not higher than for the other populated states. The obtained spectroscopic factor ($C^2S = 0.7$) is twice smaller than the one measured by Zeidman *et al.*. Finally, there was no evidence of another state at 1.23 from β-decay [29, 30] where the resolution of the gamma detectors was good enough to distinguish two peaks.
In addition new spectroscopic data have been obtained for the states at 3.35, 3.70 and 3.94 MeV. The states at 3.70 and 3.94 MeV correspond to $L = 2$ and $L = 0$ respectively and most probably come from a part of the inner $1d_{3/2}$ and $2s_{1/2}$ orbitals. However it is not possible to confirm it in shell-model calculation because these states are not included in the valence space used here. Finally, the state at 3.35 MeV is an $L = 3$ state and corresponds to 30% of the $\pi f_{7/2}$ proton-hole strength. As it was explained earlier we still miss 33% of the strength, most probably because the beam energy was not high enough to populate states at higher excitation energy. In this case it is hard to well define experimentally the centroid for the proton-hole strength. From what we have measured, we have $E(\pi f_{7/2}) = 2.45$ MeV. The missing strength corresponds to $C^2S = 2.6$. By assuming that this value is concentrated in only one state, we can say that this state has necessary an energy superior at 6.9 MeV thanks to the exponential constrain 6.16 we have established earlier. By taking a state at 6.9 MeV with $C^2S = 2.6$, the centroid is situated

at $E(\pi f_{7/2}) = 3.9$ MeV. Of course the missing strength could also be fragmented, then in order to estimate the centroid using our experimental constrain, we were able to perform a Monte Carlo as follows:

- we generate a randomly uniform energy E_{sim} between 0 and 10 MeV,
- for this energy we generate a randomly uniform spectroscopic factor C^2S_{sim} between 0 and $C^2S_{lim} = \alpha + \beta \exp \gamma E$ that corresponds to equation 6.1.

For each iteration, we do so until we reach the missing strength that corresponds to $C^2S_{missed} = 2.6$. Once we have reached this condition we can extract the estimated centroid that is represented in figure 10.2 as follows:

$$E(\pi f_{7/2}) = \frac{1}{8}\Big(\sum_{i=1}^{3} C^2S_{exp}E_{exp} + \sum C^2S_{sim}E_{sim}\Big), \tag{10.2}$$

with the condition that $C^2S_{sim} < C^2S_{lim}$ and $\sum C^2S_{sim} = 2.6$. The mean value of the distribution is $E(\pi f_{7/2}) = 3.81 \pm 0.05$ MeV and the full width at half maximum of this distribution is $\sigma_{FWHM} = 0.92$ MeV.

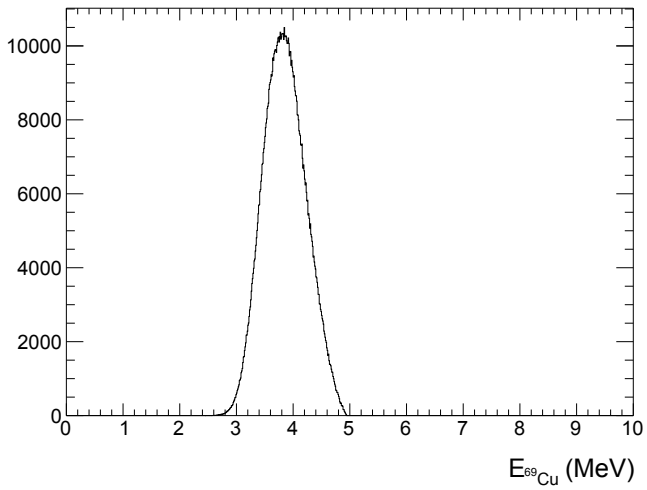

Figure 10.2: *Estimated $f_{7/2}$ centroid in ^{69}Cu*

In figure 10.3 we can see the populated states with their spectroscopic factors (bottom)

and they are compared with shell-model calculations. One can see that we are in good agreement with the $3/2^-$ ground state which corresponds to one proton in the $\pi p_{3/2}$ orbital and the $5/2^-$ state which corresponds to one proton in the $\pi f_{5/2}$ orbital. The calculation reproduce well the energy and the associated spectroscopic factors. Concerning the $7/2^-$ strength, the calculation reproduce the levels satisfactory as we can see in figure 10.4. However the calculations fail to reproduce the spectroscopic factor for the first $7/2^-$ state at 1.71 MeV. In table 10.1 are listed the proton occupancies in the valence space for the $3/2^-$ ground state and the first $5/2^-$ and $7/2^-$ excited states. As we can see in table 10.2, it was possible to determine the percentage of the wave function for the first states in ^{69}Cu. We see indeed that the wave function of the first two $7/2^-$ state arises mainly from the proton-core coupling.

Energy (MeV)	J^π	$\pi f_{7/2}$	$\pi p_{3/2}$	$\pi f_{5/2}$	$\pi p_{1/2}$	C^2S_{th}
0	$3/2^-$	7.77	1.07	0.14	0.03	0.935
1.25	$5/2^-$	7.30	0.68	0.95	0.07	0.343
1.86	$7/2^-$	7.27	1.32	0.32	0.09	0.021
2.18	$7/2^-$	7.10	0.73	1.10	0.07	0.358

Table 10.1: *Dominant components of the wave functions for the lowest states in* ^{69}*Cu*

Energy (MeV)	J^π	Composition
0	$3/2^-$	93% $\|0^+_\nu \otimes \pi p^1_{3/2}\rangle$
1.25	$5/2^-$	37% $\|0^+_\nu \otimes \pi f^1_{5/2}\rangle$
		20% $\|2^+_\nu \otimes \pi p^1_{3/2}\rangle$
		16% $\|2^+_\nu \otimes \pi f^1_{5/2}\rangle$
1.86	$7/2^-$	40% $\|2^+_\nu \otimes \pi p^1_{3/2}\rangle$
		22% $\|4^+_\nu \otimes \pi p^1_{3/2}\rangle$
		12% $\|J^+_\nu \otimes \pi f^{-1}_{7/2}\rangle$
2.18	$7/2^-$	52% $\|2^+_\nu \otimes \pi f^1_{5/2}\rangle$
		14% $\|4^+_\nu \otimes \pi f^1_{5/2}\rangle$
		16% $\|J^+_\nu \otimes \pi f^{-1}_{7/2}\rangle$

Table 10.2: *Composition of the wave function for the first states in* ^{69}*Cu*

Instead of examining the result peak by peak it could be also interesting to look at the cumulated strength by range of 2 MeV as we can see in figure 10.5. On the one hand we clearly see that we experimentally miss the strength above 4.5 MeV and on the other hand the calculation does not reproduce the experimental strength below 2 MeV. One should note, that due to the complexity of present shell-model calculations, the strength function distributions were obtained at $8p-8h$ truncation, using Lanczos strength function method with 60 iterations. We have however checked that the wave function of the starting pivot used in this calculation, i.e. the ground state of ^{70}Zn, change conspicuously between $8p-8h$ and $10p-10h$. In particular, the proton occupancy of the $f_{7/2}$ orbit drops from 7.50 particles at $8p-8h$ to only 7.34 particles at $10p-10h$. One can thus expect that more $f_{7/2}$ strength would be located at lower energy if the calculations of strength function distributions would be feasible in a larger configuration space.

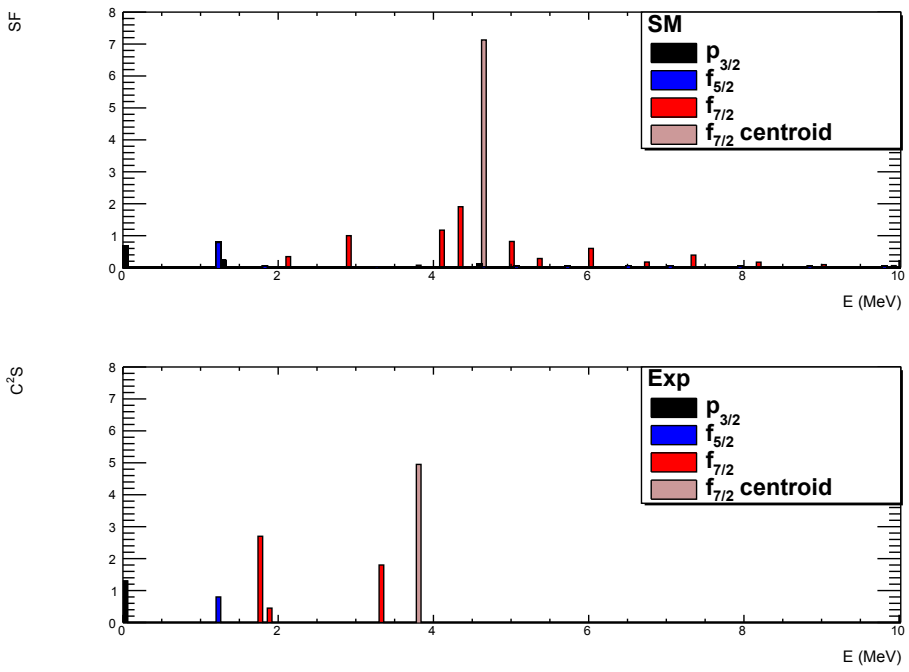

Figure 10.3: *Comparison between the experimental results (bottom) and the theoretical calculation (top) for ^{69}Cu where the position in energy of the states are plotted with the associated spectroscopic factor*

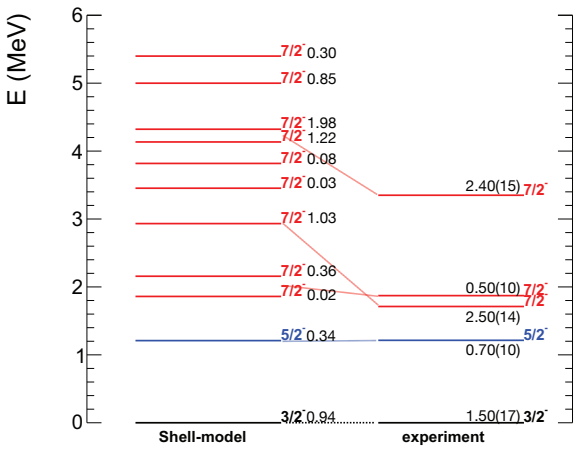

Figure 10.4: *Comparison between the experimental results (right) and the theoretical calculation (left) for* ^{69}Cu

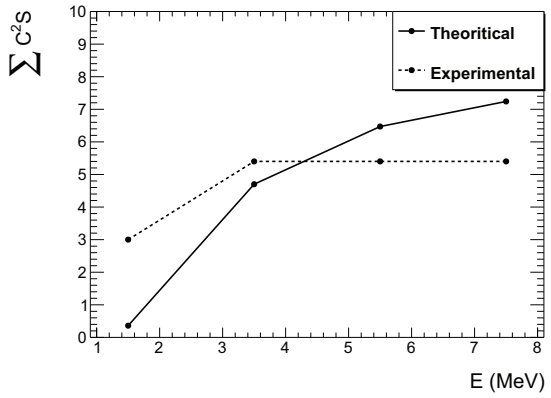

Figure 10.5: *Comparison of the cumulated spectroscopic factor in step of 2 MeV between theoretical calculation in red and experimental measurement in blue*

10.1.3 Results for ^{71}Cu

We have populated several states in ^{71}Cu as it is listed in table 9.1. We have measured 86% of the $\pi f_{7/2}^{-1}$ strength leading to an experimental centroid at 3.76 MeV. An important part of the strength (45%) was measured at 4.54 MeV. The other main result is that no states have been populated around 1 MeV. The first conclusion we can stress is that the state at 981 keV in ^{71}Cu does not correspond to a proton-hole state.
In figure 10.8 we compare theoretical calculations with the $7/2^-$ states measured in our experiment and the two others at 981 keV and 1190 keV. First of all, in the calculation the two first $7/2^-$ states lies at 1.09 MeV and 1.41 MeV with a spectroscopic factor $C^2S_{th} = 0.431$ and $C^2S_{th} = 0.007$ respectively. This is a quite small spectroscopic factor and we were not sensitive to such low spectroscopic factor in this experiment. No other $7/2^-$ states appears around 1 MeV with a high spectroscopic factor leading to the conclusion that no hole-state lies at 981 keV. The $7/2^-$ yrast state at 981 keV must correspond to another coupling. We can see in table 10.3 the proton occupation in the valence space for the $3/2^-$ ground state and the first $5/2^-$ and $7/2^-$ excited states. The ground state corresponds to a single proton in the $p_{3/2}$ orbital as the $5/2^-$ state corresponds to a single proton in the $f_{5/2}$ orbital, while for the two $7/2^-$ states neither of both correspond to a proton-hole in the $f_{7/2}$ orbital leading to very small spectroscopic factor for these states. In addition, in table 10.4 one can see the percentage of the wave function for the first states in ^{71}Cu. In the same manner as ^{69}Cu the first two $7/2^-$ state situated at 1.09 and 1.41 MeV respectively arise mainly from the proton-core coupling and do not correspond to a proton-hole state.
Experimentally the two first $7/2^-$ states belong to two different γ bands. The first one shows an $E2$ sequence built on the $3/2^-$ ground state, the $7/2^-$ state at 1190 keV makes part of this band. The $7/2^-$ state at 981 keV makes part of the second band that forms an $\Delta L = 1$ sequence [77] as we can see figure 10.6. If we assume an $M1$ sequence for this band that could explain why the 981 keV level was not seen in Coulomb excitation [31].
Finally, as we can see in figure 10.7 the $7/2^-$ populated states in our experiment are globally well reproduced by the calculations and the theoretical centroid of the $\pi f_{7/2}$ orbital lies at $E_{th}(f_{7/2}) = 3.52$ MeV, which is in good agreement with the experimental one. In a similar way as in the case of ^{69}Cu, we can look at the cumulated strength by range of 2 MeV as we can see in figure 10.9. The shape between experiment and theory are very similar even though the absolute value in the experimental case is systematically lower.

Energy (MeV)	J^π	$\pi f_{7/2}$	$\pi p_{3/2}$	$\pi f_{5/2}$	$\pi p_{1/2}$	C^2S
0	$3/2^-$	7.57	1.50	0.31	0.08	0.487
0.31	$5/2^-$	7.40	0.54	0.94	0.12	0.989
1.09	$7/2^-$	7.44	1.12	0.38	0.06	0.431
1.41	$7/2^-$	7.44	1.02	0.43	0.11	0.007
1.14	$5/2^-$	7.21	0.7 4	0.95	0.09	0.004

Table 10.3: *Dominant components of the wave functions for the lowest states in* ^{71}Cu

Energy (MeV)	J^π	Composition
0	$3/2^-$	60% $\|0^+_\nu \otimes \pi p^1_{3/2}\rangle$
0.31	$5/2^-$	36% $\|0^+_\nu \otimes \pi f^1_{5/2}\rangle$
		22% $\|4^+_\nu \otimes \pi f^1_{5/2}\rangle$
1.09	$7/2^-$	47% $\|2^+_\nu \otimes \pi p^1_{3/2}\rangle$
		11% $\|4^+_\nu \otimes \pi p^1_{3/2}\rangle$
		10% $\|J^+_\nu \otimes \pi f^{-1}_{7/2}\rangle$
1.41	$7/2^-$	42% $\|2^+_\nu \otimes \pi f^1_{5/2}\rangle$
		12% $\|4^+_\nu \otimes \pi f^1_{5/2}\rangle$
		13% $\|J^+_\nu \otimes \pi f^{-1}_{7/2}\rangle$

Table 10.4: *Composition of the wave function for the first states in* ^{71}Cu

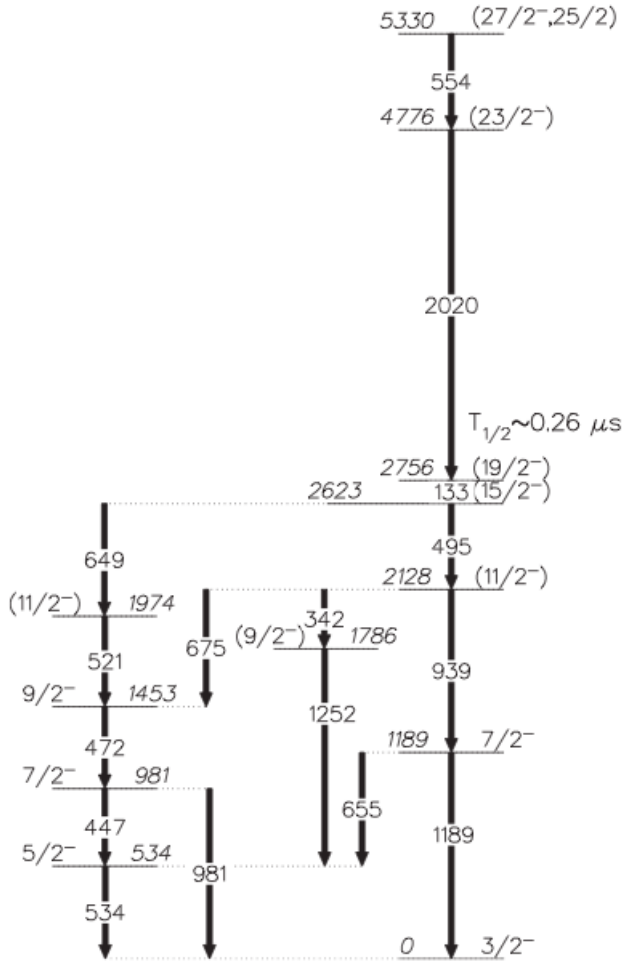

Figure 10.6: *Level scheme for* ^{71}*Cu showing the two bands* $E2$ *and* $M1$ *[78]*

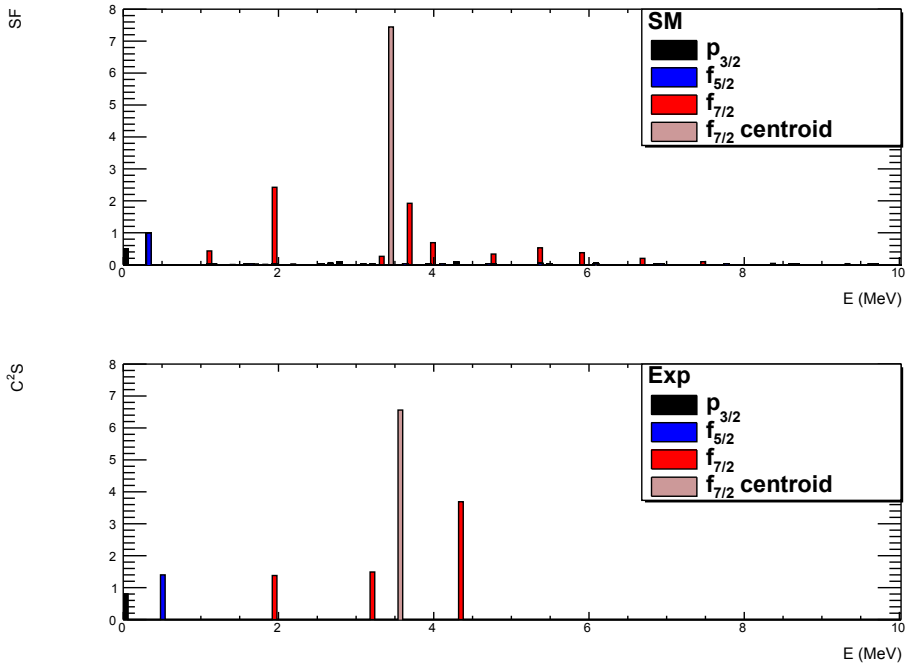

Figure 10.7: *Comparison between the experimental results (bottom) and the theoretical calculation (top) for* ^{71}*Cu where the position in energy of the states are plotted with the associate spectroscopic factor*

10.2 Monopole migration in Copper isotopes

10.2.1 Evolution of effective-single-particle energies

In figure 10.10 we can see the evolution of the proton ESPE (defined in section 1.2.4) from the interaction used in this work. As we see, the interaction predicts the inversion between $\pi p_{3/2}$ and $\pi f_{5/2}$ orbitals at the end of the neutron filling. One can see that the energy difference between $\pi f_{7/2}$ and $\pi p_{3/2}$ is stable between $N = 40$ and $N = 50$. The monopole term of the interaction seems to act in a similar manner between those two orbitals with the addition of neutrons in the $\nu g_{9/2}$ orbitals. However there is a diminution of the spin-orbit gap between $\pi f_{7/2}$ and $\pi f_{5/2}$. We see that for $N = 40$ and $N = 42$ the $Z = 28$ gap that corresponds to the energy separation between $\pi p_{3/2}$ and $\pi f_{7/2}$ orbitals

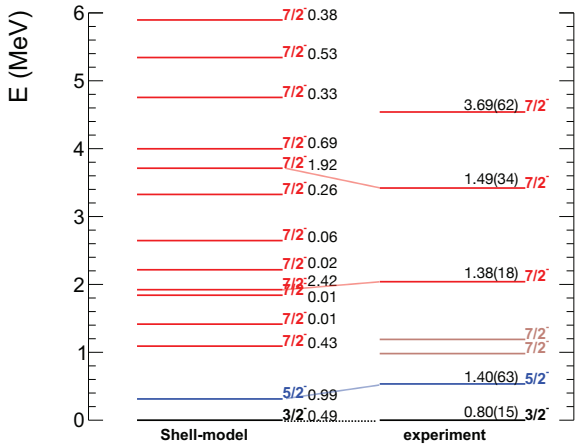

Figure 10.8: *Comparison between the experimental results (right) and the theoretical calculation (left) for* ^{71}Cu

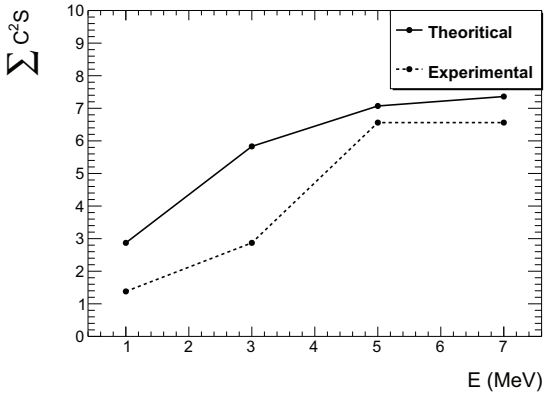

Figure 10.9: *Comparison of the cumulated spectroscopic factor by range of 2 MeV between theoretical calculation in red and experimental measurement in blue*

does not change (about 5.8 MeV) while the spin-orbit partner $\pi f_{5/2}$ is strongly affected for $N > 40$: 8.6 MeV at $N = 40$ and 5.4 MeV at $N = 50$ that corresponds to the $Z = 28$ gap.

Even though the tensor force has a strong effect on the evolution of the $\pi f_{5/2}$ ESPE, it appears that the $\pi f_{7/2}$ ESPE is less affected with the neutron filling. Indeed we know from equation 2.7 that the interaction is stronger between $\nu g_{9/2} - \pi f_{5/2}$ than $\nu g_{9/2} - \pi f_{7/2}$. Finally, because the inversion between $\pi p_{3/2}$ and $\pi f_{5/2}$ happens at the end of the neutron filling, the $Z = 28$ shell gap is not affected at $N = 50$ and ^{78}Ni should exhibit a magic character.

10.2.2 Discussion

We have measured the proton-hole states in neutron rich ^{69,71}Cu isotopes by means of (d,^{3}He) transfer reactions in two different experiments in order to extract the centroid of the $\pi f_{7/2}$ proton-hole strength in a coherent way.

In order to extend the existing data for ^{69}Cu and to study both ^{69}Cu and ^{71}Cu in a coherent way we performed a new experiment in direct kinematics using the split-pole spectrometer at Orsay. In this experiment, another part of the strength was measured.

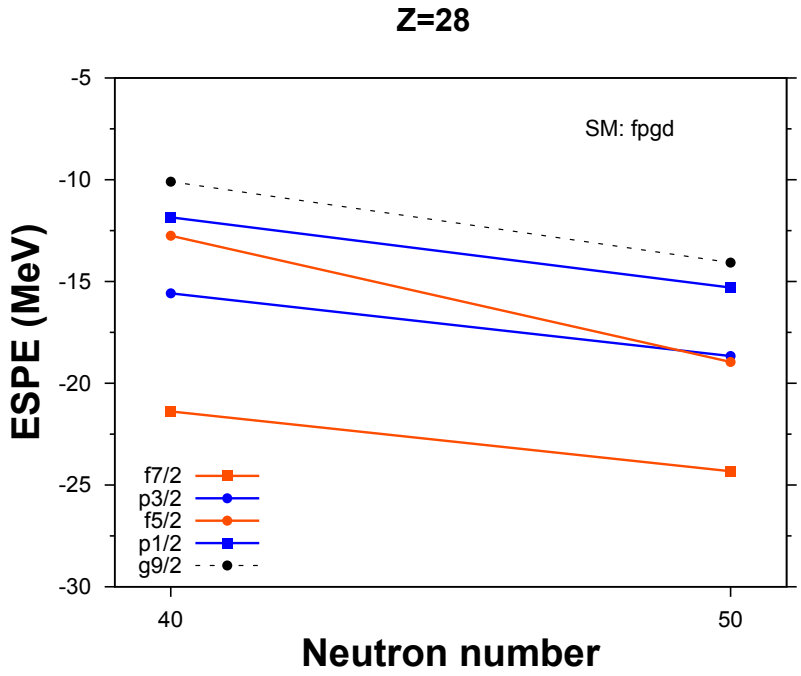

Figure 10.10: *Evolution of the effective-single-particle energies (ESPE) as a function of the neutron number*

Nevertheless 33% of the strength is still missing but we were able to constrain the missing strength and estimate the centroid of the proton $f_{7/2}$ strength distribution.
In addition for the first time spectroscopic factors were measured in ^{71}Cu through transfer reaction in inverse kinematics. In this experiment, 86% of the $\pi f_{7/2}$ strength was measured. Contrary to expectation [38] no strength lies around 1 MeV.
Because those two nuclei were studied using the same global optical potential in a coherent way, the comparison of the evolution of $\pi f_{7/2}$ orbital between $N = 40$ and $N = 42$ Copper isotopes is possible. We estimated that the $f_{7/2}$ experimental centroid in ^{69}Cu at 3.81 MeV and in ^{71}Cu at 3.76 MeV from the measured strength. Moreover the first measured $7/2^-$ state in ^{71}Cu lies at 2.04 MeV. We can conclude that the effect of neutron $\nu g_{9/2}$ on $\pi f_{7/2}$ orbital is the same as on the $\pi p_{3/2}$ orbital, as the $f_{7/2}$ centroid remains the same between $N = 40$ and $N = 42$. Or at least, within our experimental resolution the effect is not visible contrary to its spin-orbit partner $\pi f_{5/2}$ that exhibit a sudden drop in energy of 680 keV with respect to the $3/2^-$ ground state already at $N = 42$.
In figures 10.11 and 10.12 we compare the evolution of the ESPE for two different interac-

tions. The first one is the interaction from Ref. [44] where the valence space contains the f and p orbitals for the protons and the $f_{5/2}$, $p_{3/2}$, $p_{1/2}$ and $g_{9/2}$ orbitals for the neutrons. The second one corresponds to the interaction used in this work where the $d_{5/2}$ orbital is added in the valence space for the neutrons. In addition the experimental centroids are plotted in this figure. To do so, we have considered that the ground state corresponds to the $\pi p_{3/2}$ ESPE and we have added or subtracted the experimental centroid for the $\pi f_{5/2}$ and $\pi f_{7/2}$ orbitals. The arrows mean the range for the $\pi f_{7/2}$ centroid due to missing strength. Of course the experimental centroid does not match with the ESPE because of the correlations and the difference between the ESPE and the centroid gives the amount of correlations in the nucleus. The main differences between these two interactions are the inversion between $\pi p_{3/2}$ and $\pi f_{5/2}$ that occurs at a different neutron number. This indicates that the amount of correlations in $fpgd$ interaction are more important than in fpg. It is clearly visible when we look at the differences between the ESPE's and the experimental centroid. In the first interaction [44], the spin-orbit splitting evolves from 8.7 MeV to 4.1 MeV while in the latter case with the $fpgd$ interaction it evolves from 8.6 to 5.4 MeV. At $N = 40$, the spin-orbit splitting is almost identical in both interactions, while at $N = 50$, the difference is smaller in the first interaction. This is so, because of the tensor force between $\nu g_{9/2} - \pi f_{5/2}$, which is stronger in the fpg case. In order to correctly determine the strength of the tensor force, it would be important to measure it in the ^{79}Cu nucleus. In both cases, the prediction of the proton gap is between 4.1 MeV to 5.4 MeV at $N = 50$, which indicates that there is no considerable quenching of the proton gap toward the ^{78}Ni nucleus.

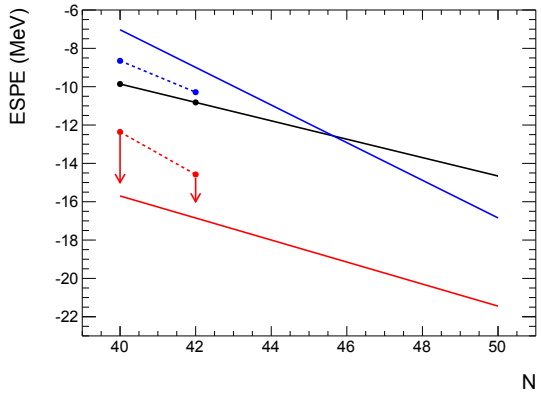

Figure 10.11: *Evolution of the ESPE for the interaction used in reference [44] with the experimental centroid value for* $N = 40$ *and* $N = 42$

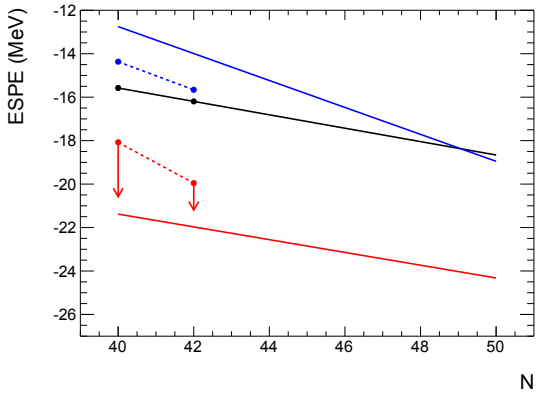

Figure 10.12: *Evolution of the ESPE for the* $fpgd$ *interaction with the experimental centroid value for* $N = 40$ *and* $N = 42$

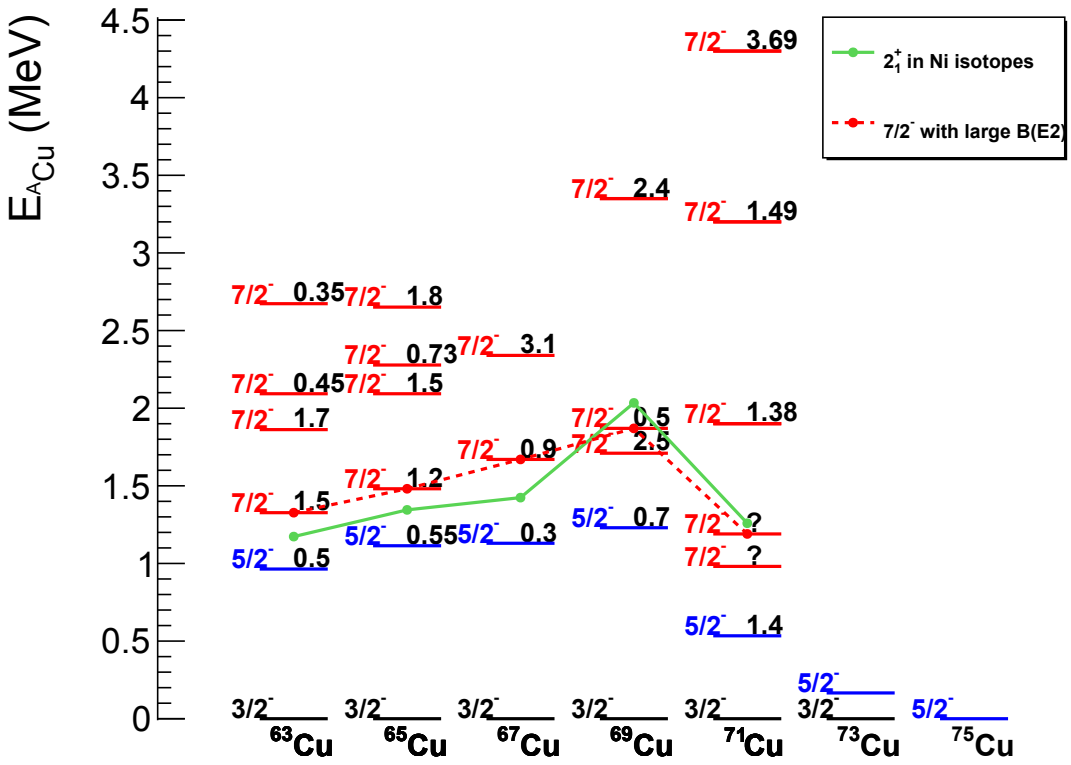

Figure 10.13: *Systematic of the levels in Copper isotopes with their spectroscopic factor, the 2_1^+ state in Nickel isotopes are also reported.*

One never notices what has been done, one can only see what remains to be done

Marie Curie (1867-1934)

Conclusion and perspectives

In this manuscript we have studied the proton-hole states in two neutron-rich Copper isotopes: ^{69}Cu and ^{71}Cu by means of the (d,^{3}He) transfer reaction. We were interested in $Z = 28$ proton-gap evolution with the filling of the neutron orbital $\nu g_{9/2}$. The experiment in direct kinematics to study the ^{69}Cu nucleus was performed to extend the existing data and to make sure that both isotopes are studied in a coherent way using the same parametrization for the optical potential. In this experiment, another part of the strength was measured but 33% of the strength is still missing giving a lower limit on the $\pi f_{7/2}$ centroid at $E(f_{7/2}) > 2.45$ MeV. In addition, for the first time we have measured the proton $f_{7/2}$ strength distribution in ^{71}Cu through the same (d,^{3}He) pick-up reaction but in inverse kinematics. In this case 86% of the strength was measured giving an experimental centroid at $E(f_{7/2}) = 3.76$ MeV. From this work, there is no indication of shell-quenching between the proton $\pi p_{3/2}$ and $\pi f_{7/2}$ orbitals at $N = 42$.

It should be also interesting to perform the complementary reaction ^{A}Ni(α,t)$^{A+1}$Cu in order to get all the sum rule. Both (α,t) and (d,^{3}He) data are only available for ^{65}Cu [79, 32]. It could be then interesting to perform the ^{68}Ni(α,t)^{69}Cu transfer reaction in inverse kinematics using active target like ACTAR [80] for instance to get the complementary strength and verify the sum rule.

It should be also interesting to perform (d,^{3}He) pick-up reaction for more neutron-rich nuclei since the study of exotic nuclei through direct reaction is a very efficient way to probe the proton gap, especially with the reaction ^{80}Zn(d,^{3}He)^{79}Cu that probe the proton gap at $N = 50$. However such an exotic beam of ^{80}Zn to perform transfer reaction is not yet available. However, very recently the SEASTAR campaign at RIKEN has taken measurements in this very neutron-rich region and the energy of the 2^+ state in ^{78}Ni should be known soon. In addition with this campaign the proton gap at $N = 50$ should be known as well through the ^{80}Zn(p,2p) proton knockout reaction. This information will tell us about the robustness of the proton and neutron gaps in ^{78}Ni. Already, very recently, Xu

et al. [81] have shown experimental indication of a doubly magic ^{78}Ni through β-decay half-lives of cobalt and nickel around $N = 50$, but the SEASTAR results should give more direct indication about its magicity.
In the future ^{80}Zn beam should be available at HIE-ISOLDE [82], but the beam energy has to be high enough to perform (d,^{3}He) pick-up reaction because of the very negative Q-value and in order to have a good matching to populate $L = 3$ states. The other main problem of such reaction is the very low energy of the ^{3}He particles emitted from the reaction. Because of that thin target has to be used if we do not want to degrade too much the resolution. In an alternative way, we could use the future GASPARD 4π silicon detector for charged particle coupled with gamma detectors such as AGATA [83] or PARIS and use a thicker target knowing that the excitation energy spectrum would be degraded. Another solution is to use future active target such as ACTAR, in this case we could have an important effective target thickness without degrading too much the resolution.
The position of proton-hole states in the copper isotopes is related to the structure of the nickel isotopes. The structure of ^{68}Ni is of great interest also nowadays. In recent calculation, Tsunoda *at al.* [84] showed that the three 0^+ states in ^{68}Ni correspond to a spherical shape for the ground state, an oblate shape for the state at 1604 keV and an prolate shape for the one at 2511 keV. It could be interesting to know the evolution of these 0^+ states for more exotic nickel isotopes and in particular for the ^{70}Ni, the structure of which is related to ^{71}Cu. The investigation of 0^+ exited state could be done through (p,p') inelastic reaction for example using MUST2 detectors to detect the emitted protons. Another interesting channel of reaction could be the ^{68}Ni(t,p)^{70}Ni reaction using the tritium source of ISOLDE for example. For the latter reaction, a beam of very high intensity ($\approx 10^6$ pps) is required.
Direct reaction will be an important tool for more of exotic beams, but it is also important to get all the data as we can and cross the information from other study such as β-decay or Coulomb excitation for example to constrain the nuclear force at stake in this mass region.

A

Target composition

ISOFLEX USA

P. O. Box 29475
San Francisco CA 94129 USA
Tel: 415-440-4433
Fax: 415-563-4433
Email: iusa@isoflex.com
EIN: 208066748

CERTIFICATE of ANALYSIS

CUSTOMER:

Centre National de la Recherche Scientifique
Institut de Physique Nucleaire Orsay
Attn: D. Jacquet
15, rue Georges ClemenceauMagasi
n Bat 100M, 91406 Orsay Cedex
FRANCE
Tel: +33-169157124

CERTIFICATE NO.: 4832

CUSTOMER ORDER NO.: L 74335/DR/BS

The description, isotopic distribution and chemical admixtures relating to the above referenced order number are certified to be as follow:

Description

ISOTOPE	Zn-70
ENRICHMENT	95.41%
ELEMENT WEIGHT	100 mg
FORM	Metal

Isotopic Distribution

ISOTOPE	Zn-64	Zn-66	Zn-67	Zn-68	Zn-70
CONTENT (%)	0.03	0.04	0.02	4.50	95.41

Chemical Admixtures

ELEMENT	Al	As	Ca	Cd	Co	Cu	Fe	Na	K	Mg
CONTENT (ppm)	1	1	1	540	1	1	75	1	1	1

ELEMENT	Mn	Pb	Si	Sn
CONTENT (ppm)	1	1	5	1

ISOFLEX USA

January 14, 2013
Date

Teck Hing Teo
Operations Manager

B

E552 electronics

We list here the different entries in the GMT and the electronic layout is presented. We use the following notation:

- AR: Fast amplifier.
- GMT: Ganil Master Trigger.
- FCC8 or DFC: Constant Fraction Discriminator.
- DSCT: Coincidences module.
- DS: Output generator (distributeurs de sorties)
- ECL/NIM: Module that convert ECL signal into NIM signal.
- FAG: Fast Analysis Gate. Temporary windows generate by the GMT. The signals from the detectors have to arrive in this gate in order to be correlated with the event.

- FIFO: Fan-In Fan-Out, the Fan-Out fonction generates severals output from an analog or logical signal.
- QDC: Charge to Digital Converter.
- U2M: Scaler.
- %: divider that transmits the signal every N events.

Channel	Entry	Trigger
1	MM1	✓
2	MM2	✓
3	MM3	✓
4	MM4	✓
5	MM5	✓
6	MM6	✓
7	MM7	✓
8	MM8	✓
9	CATS1div	✓
10	CATS2div	✓
11	CHIOdiv	x
12	PLASTdiv	✓
13	PLASTIC	x
14	SSSDdiv	✓
15	GMT 15	x
16	LISE	x

Table B.1: List of GMT's entries

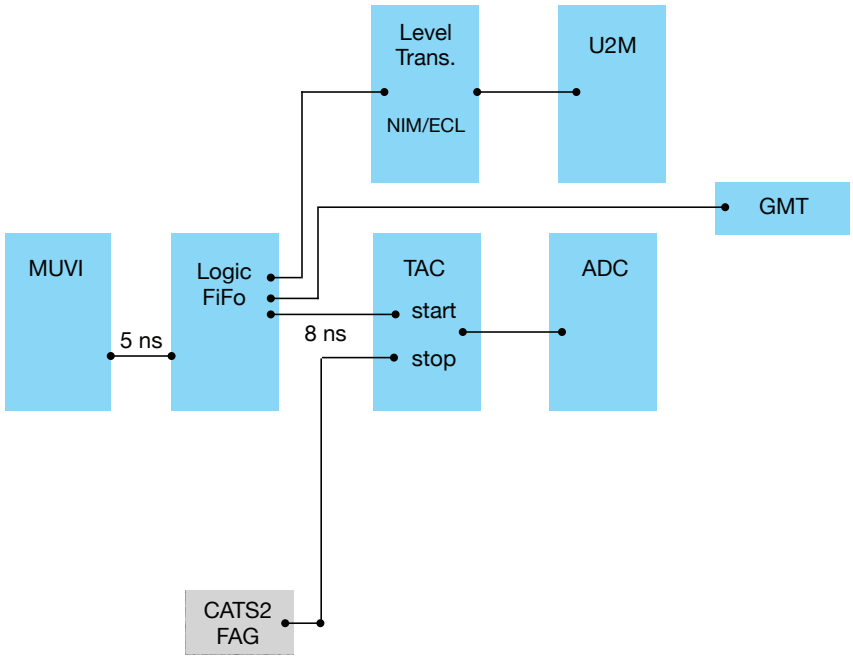

Figure B.1: Electronic chain of MUST2

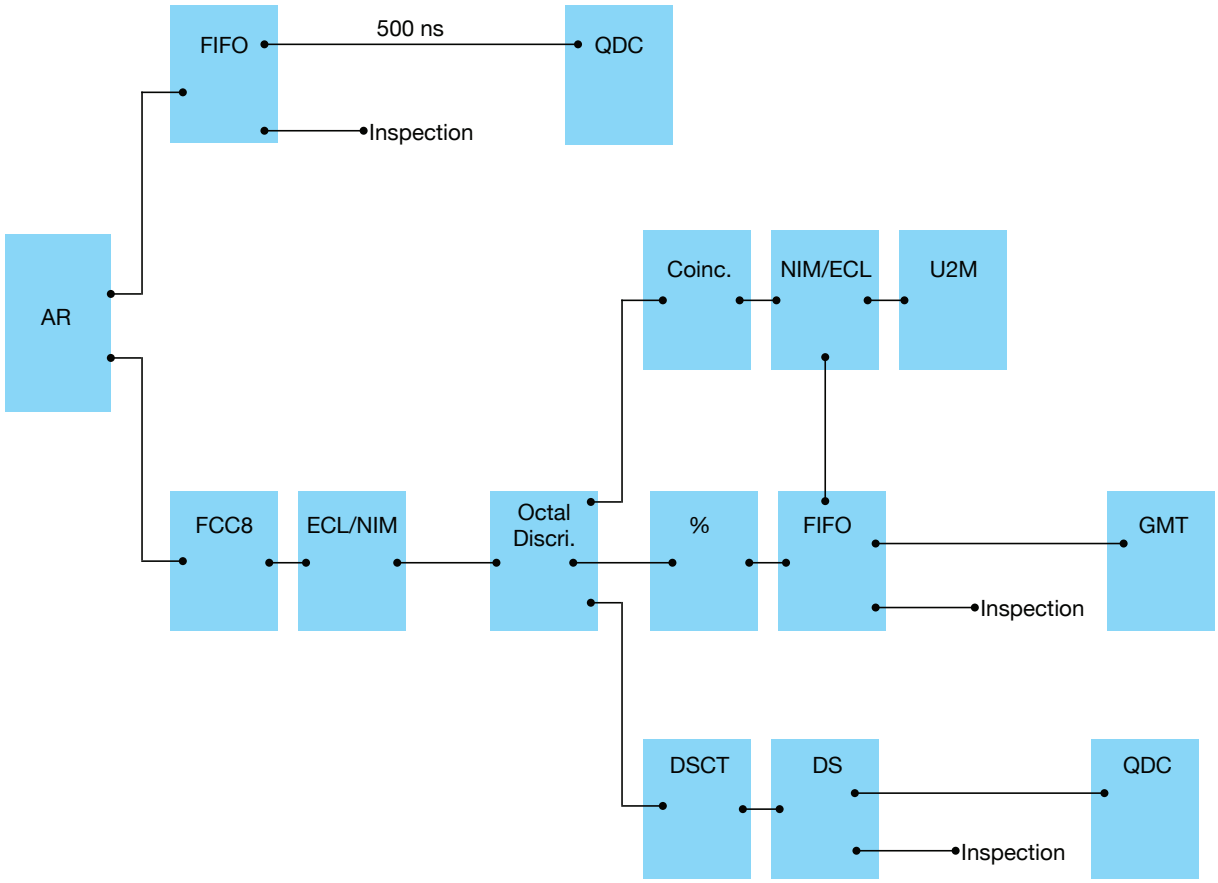

Figure B.2: Electronic chain of CATS

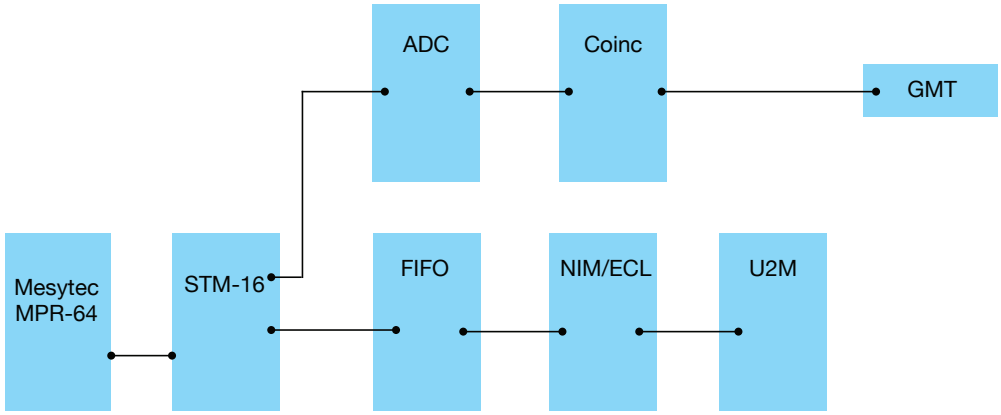

Figure B.3: Electronic chain of SSSSD detectors

Bibliography

[1] E. Rutherford. *The scattering of α and β particles by matter and the structure of the atom. Philosophical Magazine*, **21**(125):669–688, 1911.

[2] J. Chadwick. *Possible Existence of a Neutron. Nature*, **159**(312), 1932.

[3] J. Erler *et al. The limits of nuclear landscapes. Nature*, **486**:509–512, 2012.

[4] F. Wienholtz *et al. Masses of exotic calcium isotopes pin down nuclear forces. Nature*, **498**:346–349, 2013.

[5] T. Otsuka *et al. Magic Numbers in Exotic Nuclei and Spin-Isospin Properties of the NN Interaction. Physical Review Letters*, **87**:8, 2001.

[6] I. Tanihata *et al. Measurement of interaction cross sections using isotope beams of Be and B and isospin dependance of the nuclear radii. Physics Letters B*, **206**:4, 1988.

[7] G. Gamow. *Mass Defect Curve and Nuclear Constitution. Proc. Roy. Soc. A*, **126**:632–644, 1930.

[8] JC. Lattes *et al. Observations on the tracks of slow mesons in photographic emulsions. Nature*, **160**(4066):453–456, 1947.

[9] Maria Goeppert Mayer. *On Closed Shells in Nuclei. Physical Review*, **74**(3):235–239, 1948.

[10] Maria Goeppert Mayer. *On Closed Shells in Nuclei II. Physical Review*, **75**:1969–1970, 1949.

[11] Otto Haxel, J. Hans D. Jensen, and Hans E. Suess. *On the Magic Numbers in Nuclear Structure. Physical Review*, **75**:1766–1766, 1949.

[12] S. Raman, C.W Nester JR., and R. Tikkaken. *Transition probability from the ground to the first-excited 2^+ state of even-even nuclides. Atomic Data And Nuclear Data Tables*, **78**:1–128, 2001.

[13] S. K. Bogner *et al. Model-independent low momentum nucleon interaction from phase shift equivalence. Physics Reports*, **386**:1, 2003.

[14] M. Dufour and A. P. Zuker. *Realistic collective nuclear Hamiltonian. Physical Review C*, **54**(4):1641, 1996.

[15] Y. Utsuno *et al. Varying shell gap and deformation in $N \approx 20$ unstable nuclei studied by the Monte Carlo shell model. Physics Review C*, **60**:054315, 1999.

[16] S. K. Bogner, H. Hergert, J. D. Holt, A. Schwenk, S. Binder, A. Calci, J. Langhammer, and R. Roth. *Nonperturbative shell-model interactions from the in-medium similarity renormalization group*, 2014.

[17] T. Otsuka *et al. Evolution of Nuclear Shells due to the Tensor Force. Physical Review Letters*, **95**:232502, 2005.

[18] D. Suzuki *et al. Breakdown of the $Z = 8$ Shell Closure in Unbound ^{12}O and its Mirror Symmetry. Physical Review Letters*, **103**:152503, 2009.

[19] N. Alahari *et al. Direct Evidence for the Breakdown of the $N = 8$ Shell Closure in ^{12}Be. Physical Review Letters*, **85**:266, 2000.

[20] T. Otsuka *et al. Mean field with Tensor Force and Shell Structure of Exotic Nuclei. Physical Review Letters*, **97**:162501, 2006.

[21] B. Bastin *et al. Collapse of the $N = 28$ Shell Closure in ^{42}Si. Physical Review Letters*, **99**:022503, 2007.

[22] S. Raman *et al. At. Data Nucl. Data Tables*, **78**:1, 2001.

[23] M Sawacki *et al. Low energy levels in ^{72}Ni. Physics Review C*, **68**:044304, 2003.

[24] O. Perru *et al. Enhanced Core Polarization in ^{70}Ni and ^{74}Zn. Physical Review Letters*, **96**:232501, 2006.

[25] N. Aoi *et al. Enhanced collectivity in ^{74}Ni. Physics Letters B*, **692**:302, 2010.

[26] M.Wang G.Audi A.H.Wapstra F.G.Kondev M.MacCormick X.Xu and B. Pfeiffer. *The Ame2012 atomic mass evaluation (II). Chinese Physics C*, **36**:1603–2014, 2012.

[27] O. Sorlin and M.-G. Porquet. *Nuclear magic numbers: new features far from stability. Physica Scripta*, **T152**:014003, 2013.

[28] K. Heyde *et al. A Shell-model description of 0^+ intruder states in even-even nuclei. Nuclear Physics A*, **466**:189–226, 1987.

[29] S. Franchoo *et al. Beta Decay of $^{68-74}Ni$ and Level Structure of Neutron-Rich Cu Isotopes. Physical Review Letters*, **81**:15, 1998.

[30] S. Franchoo *et al. Monopole migration in $^{69,71,73}Cu$ observed from β-decay of laser-ionized $^{68-74}Ni$. Physical Review C*, **64**:054308, 2001.

[31] I. Stefanescu *et al. Interplay between Single-Particle and Collective Effects in the Odd-A Cu Isotopes beyond $N = 40$. Physical Review Letters*, **100**:112502, 2008.

[32] B. Zeidman and J. A. Nolen. *Mass and low-lying energy levels of ^{69}Cu. Physical Review C*, **18**(5):2122, 1978.

[33] K.T. Flanagan *et al. Nuclear Spins and Magnetic Moments of $^{71,73,75}Cu$: Inversion of $\pi 2p_{3/2}$ and $\pi 1f_{5/2}$ Levels in ^{75}Cu. Physical Review Letters*, **103**:142501, 2009.

[34] F. Ajzenberg-Selove *et al. States of ^{69}Cu. Physical Review C*, **24**:4, 1981.

[35] T. Ishii *et al. Core-Excited States in the Doubly Magic ^{68}Ni and its Neighbor ^{69}Cu. Physical Review Letters*, **84**:1, 2000.

[36] T. Ishii *et al. The $(\nu g_{9/2}\pi p_{3/2})_{19/2^-}$ Isomer in ^{71}Cu and the prediction of its E2 Decay from the Shell Model. Physical Review Letters*, **81**:19, 1998.

[37] R. Grzywacz *et al. New Island of μs Isomers in Neutron-Rich nuclei around the $Z = 28$ and $N = 40$ Shell Closures. Physical Review Letters*, **81**(4), 1998.

[38] A.M. Oros-Peusquens and P.F. Mantica. *Particle-core coupling around ^{68}Ni: a study of subshell closure at $N = 40$. Nuclear Physics A*, **669**:81–100, 2000.

[39] M. Doncel *et al. Lifetime measurements in neutron-rich Cu isotopes. Acta Physica Polonica B*, **44**(3), 2013.

[40] G. Rotbard *et al.* $^{70,72,74,76}Ge(d,^3He)^{69,71,73,75}Ga$ *reactions ot 26 MeV . Physics Review C*, **18**:1, 1978.

[41] D. Verney *et al. Low-energy states of* $^{81}_{31}Ga_{50}$*: Proton structure of the nuclei close to* ^{78}Ni*. Physics Review C*, **76**:054312, 2007.

[42] NNDC. http://www.nndc.bnl.gov.

[43] N.A. Smirnova *et al. Shell-model description of monopole shift in neutron-rich Cu. Physical Review C*, **69**:044306, 2004.

[44] K. Sieja and F. Nowacki. *Shell quenching in* ^{78}Ni*: A hint from the structure of the neutron-rich copper isotopes. Physical Review C*, **81**:061303(R), 2010.

[45] N.A. Smirnova *et al. Shell evolution and nuclear forces. Physics Letters B*, **686**:109–113, 2010.

[46] N.A. Smirnova *et al. Nuclear shell evolution and in-medium NN interaction. Physical Review C*, **86**:034314, 2012.

[47] R.J. Furnstahl and H.-W. Hammer. *Are occupation numbers observable ? Physics Letters B*, **531**:203–208, 2002.

[48] T. Duguet and G. Hagen. *Ab-initio take on effective single-particle energies in double closed shell nuclei. Physics Review C*, **85**:034330, 2012.

[49] Norman K Glendenning. *Direct nuclear reaction.* World Scientific, 2004.

[50] E. Bauge. *Sonder la structure nucléaire avec des nucléons.* Ecole Joliot-Curie, 2007.

[51] A. Messiah. *Mécanique quantique, Tome 2.* Dunod, 1995.

[52] J.E. Spencer and H.A. Enge. *Split-Pole magnetic spectrograph for precision nuclear spectroscopy. Nuclear Instruments and Methods*, **49**:181–193, 1967.

[53] R.G. Markham and R.G.H. Robertson. *High resolution position-sensitive proportional counter. Nuclear Instruments and Methods*, **129**:131–140, 1975.

[54] W.W. Daehnick *et al. Global optical model potential for elastic deuteron scattering from 12 to 90 MeV. Physical Review C*, **21**(6):2253, 1980.

[55] C. M. Perey and F. G. Perey. *Compilation of phenomenological optical-model parameters. At. Data Nucl. Data Tables*, **17**(1), 1976.

[56] I. Brida Steven C. Pieper and R. B. Wiringa. *Quantum Monte Carlo calculations of spectroscopic overlaps in $A \leq 7$ nuclei. Physical Review C*, **84**:024319, 2011.

[57] NPTOOL. https://forge.in2p3.fr/projects/nptool.

[58] A. Matta. *Study of the very neutron-rich ^{10}He by one-proton transfer reaction ^{11}Li(d,^{3}He).* PhD thesis, Université Paris-Sud XI, Institut de Physique Nucléaire, CNRS/IN2P3/Université Paris-Sud X1, 91406 Orsay Cedex, 2012.

[59] GEANT4. http://geant4.cern.ch.

[60] ROOT. http://root.cern.ch.drupal.

[61] Y. Blumenfeld *et al. Facilities and methods for radioactive ion beam production. Physica Scripta*, **T152**:014023, 2013.

[62] R. Anne *et al. The achromatic spectrometer LISE at GANIL. Nuclear Instruments and Methodes in Physics Research A*, **257**, 1987.

[63] W. Mittig. *Spectromètres magnétiques et électriques comme détecteurs de haute résolution et comme filtres sélectif.* Ecole Joliot-Curie, 1994.

[64] R. Anne *et al. LISE3 : a magnetic spectrometer; Wien filter combination for secondary beam production. Nuclear Instruments and Methodes B*, **70**:276, 1992.

[65] S. Ottini-Hustache *et al. CATS, a low pressure multiwire proportionnal chamber for secondary beam tracking at GANIL. Nuclear Instruments and Methodes in Physics Research A*, **431**:476–484, 1999.

[66] E. Pollacco *et al. MUST2: A new generation array for direct reaction studies. The European Physical Journal*, **25**(10.1140/epjad/i2005-06-162-5):287–288, 2005.

[67] D. Suzuki *et al. Missing mass spectroscopy on oxygen isotopes beyond the proton-drip line: mirror symmetry of nuclear shell evolution. The European Physical Journal. A*, **48**:130, 2012.

[68] S. Giron. *Etude de la réaction d'intérêt astrophysique $^{60}Fe(n,\gamma)^{61}Fe$ par réaction de transfert (d,pγ).* PhD thesis, Université Paris-Sud XI, Institut de Physique Nucléaire, CNRS/IN2P3/Université Paris-Sud XI, 91406 Orsay Cedex, 2011.

[69] F. Flavigny. *Détermination de facteurs spectroscopiques absolus par réaction de knockout et de transfert.* PhD thesis, Université Paris-Sud XI, CEA, 2011.

[70] G. Burgunder. *Etude de l'interaction nucléaire spin-orbite par réactions de transferts $^{36}S(d,p)^{37}S$ et $^{34}Si(d,p)^{35}Si$.* PhD thesis, Université de Caen, GANIL, 2011.

[71] J. J. H. Menet *et al. Total-Reaction-Cross-Section Measurements for 30-60-MeV Protons. Physical Review C*, **4**:1114, 1971.

[72] D. Y. Pang *et al. Global optical model potential for $A = 3$ projectiles. Physical Review C*, **79**:024615, 2009.

[73] D. Von Ehrenstein and J.P. Schiffers. *Study of (d,p) reactions on $^{64,66,68,70}Zn$. Physical Review*, **164**(4):1374, 1967.

[74] E. Caurier and F. Nowacki. *Present status of shell model techniques. Acta Physica Polonica B*, **30**:3, 1999.

[75] A. Poves and F. Nowacki. *The nuclear shell model. Lectures Notes in Physics*, **581**:70–101, 2001.

[76] S.M. Lenzi *et al. Island of inversion around ^{64}Cr. Physical Review C*, **82**:054301, 2010.

[77] G. de Angelis. *Exploring the evolution of the shell structure by means of deep inelastic reactions: recent results from LNL. Physica Scripta*, **T150**:014010, 2012.

[78] I. Stefanescu *et al. Levels above the $19/2^-$ isomer in ^{71}Cu: Persistance of the $N = 40$ neutron shell gap. Physical Review C*, **79**:034319, 2009.

[79] P. Roussel *et al. Etude des réactions de transfert (α,t), (α,^{3}He) dans la couche fp. Nuclear Physics A*, **155**:306–336, 1970.

[80] J. Pancin *et al. Electrostatic mask for active targets. JINST*, **7**:01006, 2012.

[81] Z. Y. Xu *et al. β-Decay Half-Lives of $^{76,77}Co$, $^{79,80}Ni$ and ^{81}Cu: Experimental Indication of a Doubly Magic ^{78}Ni. Physical Review Letters*, **113**:032505, 2014.

[82] A. Herlert *et al. The HIE-ISOLDE Project. Journal of Physics: Conference Series*, **312**:052010, 2011.

[83] D. Bazzacco *et al. The Advanced Gamma Ray Tracking Array AGATA. Nuclear Physics A*, **746**:248–254, 2004.

[84] Y. Tsunoda *et al. Novel shape evolution in exotic Ni isotopes and configuration-dependent shell strucuture. Physical Review C*, **89**:031301(R), 2014.